



# ScuDo

Scuola di Dottorato ~ Doctoral School

WHAT YOU ARE, TAKES YOU FAR

Doctoral Dissertation

Doctoral Program in Electronic Engineering (29<sup>th</sup> cycle)

# Memristor Platforms for Pattern Recognition

## Memristor Theory, Systems and Applications

By

**Jacopo Secco**

\*\*\*\*\*

**Supervisor(s):**

Prof. Fernando Corinto, Supervisor

**Doctoral Examination Committee:**

Prof. Julius Georgiou, Referee, University of Cyprus

Prof. Mauro Forti, Referee, Università degli Studi di Siena

Prof. Salvatore Iannotta, IMEM-CNR

Prof. Georgis Sirakoulis, Democritus University of Thrace

Politecnico di Torino

2017

## **Declaration**

I hereby declare that, the contents and organization of this dissertation constitute my own original work and does not compromise in any way the rights of third parties, including those relating to the security of personal data.

Jacopo Secco  
2017

\* This dissertation is presented in partial fulfillment of the requirements for **Ph.D. degree** in the Graduate School of Politecnico di Torino (ScuDo).

*A mia Mamma ed a mio Papá...ed a tutti quelli che hanno creduto come loro...*

## **Acknowledgements**

At the end of this journey, many are to thank for their precious work and help.

At first I would like to acknowledge my Ph.D. supervisor Professor Fernando Corinto for his mentorship and his continuous technical, professional and personal support throughout the whole project.

I would like to acknowledge also Professor Marco Gilli, Professor Emilio Paolucci, DET and the whole Institution for the support and the large number of growth possibilities given to my Ph.D. and research projects.

I would also like to thank Professor Ronald Tetzlaff, Professor Danilo Demarchi, Professor Alon Ascoli, Professor Laryssa Baraban, Professor Kyeong-Sik Min, Professor Sandro Carrara, Professor Marius Orłowski, Doctor Matteo Fasano, Doctor Jens Muller, Doctor Julian Shutt, Doctor Juliane Simchen, and Doctor Abu Sebastian for their cooperation on the research projects brought on together.

I would like to thank my team at Omnidermal: Marco Farina, Alberto Uberti, Piergiorgio Perotto, Paride Letizia, Vito Musci and Ubaldo Uberti for the work done and for their commitment to the goals that have been reached and the ones that still have to come. Same I would like to thank Doctor Elia Ricci for his clinical and scientific help.

At last I would like to thank all my (now extended) family, especially my parents and my girlfriend Chiara for their unconditional love and affection.

Thank you all.

## Abstract

In the last decade a large scientific community has focused on the study of the memristor. The memristor is thought to be by many the best alternative to CMOS technology, which is gradually showing its flaws. Transistor technology has developed fast both under a research and an industrial point of view, reducing the size of its elements to the nano-scale. It has been possible to generate more and more complex machinery and to communicate with that same machinery thanks to the development of programming languages based on combinations of boolean operands. Alas as shown by Moore's law, the steep curve of implementation and of development of CMOS is gradually reaching a plateau. It is clear the need of studying new elements that can combine the efficiency of transistors and at the same time increase the complexity of the operations.

Memristors can be described as non-linear resistors capable of maintaining memory of the resistance state that they reached. From their first theoretical treatment by Professor Leon O. Chua in 1971, different research groups have devoted their expertise in studying the both the fabrication and the implementation of this new promising technology. In the following thesis a complete study on memristors and memristive elements is presented. The road map that characterizes this study departs from a deep understanding of the physics that govern memristors, focusing on the HP model by Dr. Stanley Williams. Other devices such as *phase change memories* (PCMs) and memristive biosensors made with Si nano-wires have been studied, developing emulators and equivalent circuitry, in order to describe their complex dynamics. This part sets the first milestone of a pathway that passes through more complex implementations such as *neuromorphic systems* and *neural networks* based on memristors proving their computing efficiency. Finally it will be presented a memristor-based technology, covered by patent, demonstrating its efficacy for clinical applications. The presented system has been designed for detecting and assessing automatically chronic wounds, a syndrome that affects roughly 2% of

the world population, through a Cellular Automaton which analyzes and processes digital images of ulcers. Thanks to its precision in measuring the lesions the proposed solution promises not only to increase healing rates, but also to prevent the worsening of the wounds that usually lead to amputation and death.

# Contents

<b>1</b>	<b>Introduction</b>	<b>1</b>
1.1	Description of the Work . . . . .	9
1.1.1	Contributions to the Work . . . . .	9
1.1.2	Author's Contribution to Papers . . . . .	10
<b>2</b>	<b>Memristor Theory: Device Modeling and Simulations</b>	<b>12</b>
2.1	Original Description . . . . .	13
2.2	Flux-Charge Analysis Method and Memristor Classification . . . . .	19
2.2.1	$\mathcal{L}\mathcal{M}$ Circuit Class Introduction and Analysis . . . . .	22
2.2.2	Insight on Kirchoff's Incremental Laws . . . . .	24
2.2.3	Memristor Classification Based on $\varphi$ and $q$ . . . . .	25
2.3	Conductive Filament Formation and Rupturing in the HP Device . . . . .	29
2.3.1	General Overview of Memristor Models and HP Model Introduction . . . . .	29
2.3.2	Chua's Constitutive Memristor Relations for William's De- vice: Set Model . . . . .	33
2.3.3	Chua's Constitutive Memristor Relations for William's De- vice: Reset Model . . . . .	38
2.3.4	Rupturing Model Simulation Results . . . . .	44
2.3.5	Discussion and Conclusions . . . . .	50
2.4	$\varphi - q$ Modeling of Phase Change Memories . . . . .	53

2.4.1	Introduction to PCMs and Physical Description . . . . .	54
2.4.2	Memristor Model for PCM devices . . . . .	57
2.4.3	Derived Conclusions on PCMs as Memristors . . . . .	62
2.5	Memristive-RC Switching Dynamics of <i>Si</i> Nano-Wire Biosensors . .	63
2.5.1	Electronic Approach Model . . . . .	66
2.5.2	SiNW Memristor Classification . . . . .	69
2.6	Memristor Emulator Circuit Based on Static Nonlinear Two-Ports and Dynamic Bipole . . . . .	71
2.6.1	Circuit Design and Analysis . . . . .	72
2.6.2	Spice Modeling and Simulation Results . . . . .	76
<b>3</b>	<b>Memristors-Based Systems for Machine Learning</b>	<b>79</b>
3.1	General Introduction to Perceptrons and SBPI . . . . .	80
3.1.1	Stochastic Belief Propagation Inspired Algorithm . . . . .	82
3.2	Memristor-Based SBPI Perceptron Design and Implementation . . .	85
3.2.1	Generalized Boundary Condition Memristor Model . . . . .	86
3.2.2	Memristor-Based Perceptron Circuit Design . . . . .	87
3.3	Functional and Learning Efficiency Essays on the Memristive Per- ceptron . . . . .	91
3.3.1	"Read" and "Write" Impulse Characterization . . . . .	93
3.3.2	Binary Synapse Threshold Characterization . . . . .	94
3.3.3	Perceptron Learning Efficiency Essays . . . . .	95
3.3.4	Statistical Analysis on the Learning Efficiency of the Memristor- Based SBPI Perceptron . . . . .	98
<b>4</b>	<b>Memristive Systems for Clinical Assessment of Chronic Wounds</b>	<b>104</b>
4.1	Clinical Overview . . . . .	105
4.2	Cellular Automaton and Discrete Time Cellular Neural Networks . .	106

---

4.2.1	Cellular Automata and Stochastic Belief Propagation In- spired Perceptron Equivalence . . . . .	109
4.2.2	Element Detection in an RGB Image Trough Memristive SBPI-CA . . . . .	112
4.3	System Based on SBPI-CA for Chronic Wound Detection, Follow- Up and Assessment . . . . .	115
4.3.1	System Design . . . . .	117
4.3.2	Pre-Clinical Trials and Results . . . . .	123
<b>5</b>	<b>Conclusion</b>	<b>129</b>
	<b>References</b>	<b>131</b>
	<b>List of Figures</b>	<b>142</b>
	<b>List of Tables</b>	<b>151</b>

# Chapter 1

## Introduction

The memristor as a circuit element was first theoretically treated by professor Leon O. Chua in 1971, where he defined it as *the fourth and missing circuit element* [1]. Memristors were defined this way since they represent the missing link between the integral of the current named *charge* ( $q$ ), and the integral of the voltage named *flux* ( $\phi$ ) as shown in Figure 1.1, which also introduces its circuit symbol. Although Professor Chua introduced and deeply described the basis of this new element he also stated that, at that time, the discovery of the physical device was yet to be done. In 2008, at the Hp Laboratories, Dr. Stanley Williams was able to produce a first prototype of memristor [2] opening a new path for scientific development and discovery around the element, from device modeling and building, to implementation and application in complex systems.

One example of scientific community that was created from these discoveries is the *EU COST Action IC1401*, which has the scope to provide means of easy communication to researchers that are geographically dispersed around the world in order to reach ambitious and multidisciplinary goals. Recently the COST Action IC1401 has presented an interesting work of review, summarizing the most recent and significant advances in memristor theory and applications [3].

The applications for which memristors are intended are various, mostly focused on non-volatile memory, neuromorphic engineering and mixed-signal processing due to their properties. However, mostly in the field of non-volatile memories given that research has been predominantly driven towards that kind of industry, the majority of memristive devices explored exhibit non-volatile resistance states that can be

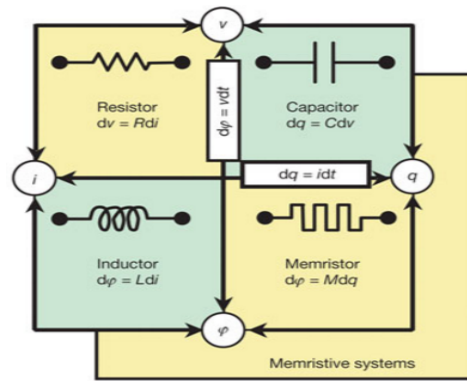


Fig. 1.1 Comparison of the memristor with the other three fundamental two-terminal circuit elements, respectively related to their descriptive variables. Through this figure it is possible to note the appropriateness of the *missing element* definition given by Professor Leon Chua in 1971. In the bottom right corner it is shown the circuit symbol of the memristor. This figure has been taken from the work of Strukov *et al.* [2].

increased or decreased electrically in an analog or digital manner. In particular, proposed memristive devices in the literature are based on physical concepts such as phase-change in chalcogenides, ferroelectricity, ferromagnetism, anion- or cation-based nano-ionic transport [4]. Much of them exhibit a two-step resistance type behaviour such as PCMs, ferroelectric memory (FeRAM), magnetic memory (MRAM) and resisting switching memory (ReRAM). All these have intrinsic properties that bound them to the concept of memristor. As so in literature it is possible to find works related to their equivalence and their classification as memristive devices [5]. Moreover their applications are similar to the ones proposed for memristors concerning neuromorphic engineering [6–8] and mixed-signal processing [9–11]. Finally a large number of nano-devices that exploit purely electronic effects has shown memristive behaviour such as ferroelectric and spin-torque memristors, where the resistance changes are obtained through electron mediated phenomena at the interfaces [12, 13].

In order to exploit memristors in more complex systems, such as devices that can exploit a wide range of applications it is crucial to obtain reliable circuit models that can be used in circuit design. In memristor theory, the basic fingerprint that was associated to memristors is the "pinched hysteresis loop" which will be deeply described later in this work. The pinched loop shows the nonlinear dynamics of memristors in the  $v - i$  domain when excited with a zero-mean periodic signal [14]. This consideration extended the definition of memristors to a wide range of

---

elements and devices. One noteworthy example, that will be exhaustively treated in the following chapters, are memristive biosensors described in [15]. These devices, composed essentially by a silicon nano-wire clamped between two *SiNi* electrodes, exploit the classical pinched loop  $v - i$  to sense the presence (or the absence) of a given antigen of a sampled solution or its pH variations.

The particular memristive  $v - i$  curve has been the starting point to study a standardized modeling method for memristors. Proceeding with the discovery and the development of new memristive elements it was clear that not all of them had the same behaviour in the  $v - i$  domain (i.e. the pinched loop presented different dynamics). Various mathematical models were investigated with the scope of providing developers with reliable tools to simulate memristive behaviour in circuit design and their applications. Biolek *et al.* developed a mathematical model which is descriptive of memristor dynamics based on the pinched hysteresis loop [16]. The same group recently described the charge-controlled memristance ( $R_M(q)$ ) map of all orders within the working intervals of  $q$  [17] and developing a novel fingerprint of generic ideal memristors [18], yielding to a new knowledge on frequency dependance of memristive devices' behaviour. As it will be described subsequently in this work, the pinched hysteresis loop derived from the response of memristive devices strongly depends on the frequency of the input signal changing the shape of the curve.

Exquisitely based on circuit design, the Pickett model serves as a SPICE modeling tool to simulate memristor non-linear dynamics [19]. This model has been improved based on the emerging technologies regarding this particular field and most of all the need to cope with greater simulation tasks required by the larger complexity of the studied applications. Noteworthy examples are given by the behavioural S-model and the modified Pickett model [20]. Finally Ascoli *et al.* developed the Generalized Boundary Condition Memristor (GBCM) model [21]. Though the GBCM it is possible to model a broad range of memristor and memristive devices by setting the suitable parameters. The equivalent circuit of this model is reported in Figure 1.2. Considering the figure the on and off boundary state cells act as commutated switches that let or close the current flow at the terminals *A* and *B*. The capacitance *C* is the responsible of the memory of the device keeping the state cells in their state depending on the volatility of the modeled memristor. The actual memristance is given by the series of  $R_{off}$  and  $R(v_x)$  which is an appropriately modeled non-linear resistor. Through the correct calibration of the switches, also the different frequency responses can be modulated to resemble more the desired

device to model. A practical example of extended use of the GBCM, other than a more precise insight of the model will be delivered in the next chapters of this work.

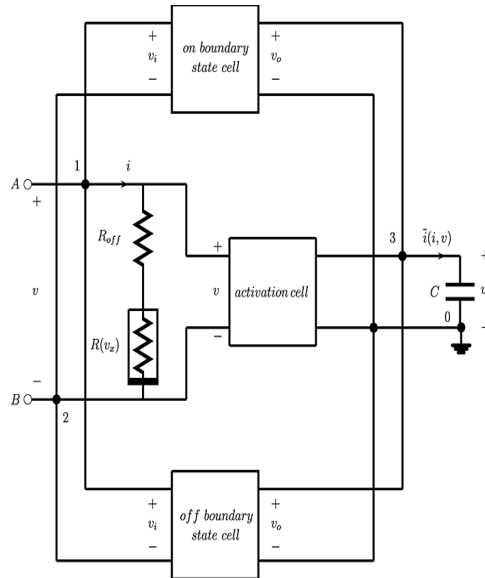


Fig. 1.2 Equivalent circuit of the Generalized Boundary Condition Memristor (GBCM) developed by Ascoli *et al.* The circuit presented is taken directly from [21]. From the manipulation of the on and off state cells it is possible to modulate the effective resistance given by the series of  $R_{off}$  and  $R(v_x)$ , which is a non-linear resistor that depends on the voltage drop on the capacitor  $C$ .  $C$ , on the other hand expresses the volatility of the desired modeled device.

The broad range of memristors that were created and developed in the past years led to a variety of physical interactions between the elements used to build the devices. Considering the  $TaO$  devices, of which in [2] is reported the first example, the  $Ag/SiO_2/Pt$  devices treated by Valov *et al.* [22], the memristors based on  $NiTi$  smart alloys [23, 24], and the other elements that show memristive behaviour (such as PCMs, ReRAMS, MRAMS and FeRAMS), it is possible to notice from literature that all present different  $v - i$  curves resulting in pinched loops of different shape. Moreover the frequency response, as afore mentioned, of these elements is different and the reactions to the input signals changes accordingly. When a memristor is excited with a zero-mean periodic signal, higher is the frequency more the element will act as a linear resistor. The frequency dependance of the response of these devices is to be considered the direct consequence of the physical phenomena that occur amongst the devices' elements.

Through a deeper analysis of all the models reported in literature it is possible to note that a series of physical variables may interfere or have a great resonance on the behaviour of the different elements. Broader is the range of phenomena and electrochemical interactions that can give rise to memristive effects, broader must be the descriptive properties of the model that might summarize them all. It is possible to state that the  $v - i$  response of a memristor is to be considered input dependant and so it cannot be considered as a descriptive model for a memristive device. For this reason Corinto and Forti introduced a novel analysis method based on the electrical variables of flux and charge ( $q$  and  $\varphi$  respectively) instead on the canonic voltage and current ( $v$  and  $i$ ) [25].

Flux-charge analysis ( $\varphi - q$  models) have the scope to have two main advantages with respect to non-linear circuit theory:

1. more simple analysis of non-linear dynamics and bifurcations by means of smaller ordinary differential equations (ODEs);
2. a clear understanding of the effects of initial conditions.

In [25], it is demonstrated the effectiveness of exploiting the *integral of Kirchoff's current and voltage law* (KqL and K $\varphi$ L respectively) in a large class of memristor circuits. The need for this analytical method rises from the incremented development of hybrid circuits that contain memristors and CMOS. The design of programming of such devices resulted difficult for several reasons related mostly to the non-linear behaviour of memristors acting as volatile memories and the low programming resolution of memristors acting as non-volatile memories.

Most importantly the  $\varphi - q$  analysis led to a greater classification of memristors and memristive devices. As afore mentioned the broad variety of devices and elements that show memristive effects leads to a great difficulty in standardizing the devices. Knowing how the various physical variables and the physical phenomena taking place in the elements interact with the overall dynamics is of key importance in the attempt of implementing memristors in larger and more complex systems. Recently it has been proposed to classify memristors in three major groups depending on the governing equations of the different devices [26]. Considering an internal vector  $\mathbf{x}$  composed of  $n$  state variables such that  $\mathbf{x} = (x_1, x_2, \dots, x_n)^T \in \mathbb{R}^n$  it is possible to state that the dynamics of these variables, in general electrical and non electrical, can be described as:  $\dot{\mathbf{x}} = g(u, \dot{u}, \mathbf{x})$ . Considering  $u$  as an input, in memristor

theory as it will be explained in details in the following chapters,  $\dot{\mathbf{x}}$  can represent the flux  $\varphi$  or the charge  $q$ . From this consideration in [26] it has been proposed to classify memristors in the following three categories (over here reported as charge controlled, but is always intended law of duality for flux controlled devices):

1. *ideal memristors*  $\Rightarrow v = f(q)i$ ;
2. *generic memristors*  $\Rightarrow v = f(q, \mathbf{x})i$ ;
3. *extended memristors*  $\Rightarrow v = f(q, i, \mathbf{x})i$ .

A detailed description of the  $\varphi - q$  analysis method and memristor classification will be delivered in the following chapters as well as their use in modeling different memristive devices such as: the HP *Pt/TaO/Pt* device [2], PCMs [27] and the aforementioned memristive bio-sensors based on silicon nano-wires [15]. In the first case it will be provided a mathematical demonstration based on experimental results on how flux plays an important role in the formation and in the rupturing of the conductive filament.

Regarding PCMs, Sebastian *et al.* provided an important study on the physical and chemical phenomena regarding their behaviour [28]. As a matter of fact these devices have the capability of keeping and maintaining a given memory state by increasing and decreasing the size of a chalcogenide bulb exploiting its phase transition from crystalline to amorphous. Based on the experimental data of from the IBM Lab in Zurich (CH) it was possible to derive a mathematical model based on  $\varphi$  and  $q$  that is able to describe the particular behaviour of these elements. Similarly it has been done with silicon nano-wire bio-sensors, with the addition of a reliable circuit model for sensing reading and implementation.

The scope for this kind of analysis is to achieve a possible generalized memristor model able to implement memristive devices in more complex systems. Chua and Yang in 1987 and 1988, proposed a novel class of information processing systems called *Cellular Neural Networks* (CNNs) [29]. Their work took inspiration from Hopfield's Networks (regarding *Neural Networks*) [30] and regarding *Cellular Automata*, CAs) [31]. CNNs take the best features from both worlds. As neural networks, CNNs are a large scale system for real time signal processing, thanks to their continuous time features. As CAs they consist of a *cellular* nature, since they represent a mass aggregate of regularly spaced operands denominated cells.

---

CNNs, CAs and neural networks are part of a wider class of platforms that take inspiration from the computing capabilities and "strategies" of human brain: *biologically-inspired systems*. Biologically inspired systems and algorithms are widely studied in the fields of computation and signal processing thanks to their advantages regarding canonic computing. The most important feature of biologically-inspired computing is *machine learning*, since it renders the possibility of treating and classifying massive numbers of data avoiding coding exploiting the interactions and the evolution of the internal state of the cells composing the network, simulating bio-inspired *synapses*.

One explicative example of bio-inspired algorithms for pattern classification [32] is the *perceptron*, a system composed of a given number of single arrays of elements, working in parallel, that evolve at each iteration and at each input presentation, rendering a combination of desired operands [33]. The perceptron and perceptron-like networks were developed in the years and increased their learning and classification efficiency. The *stochastic belief propagation inspired algorithm* (SBPI) represents a good example of this kind of algorithm. The SBPI consists on a single array of cells that may have a range of possible internal states  $K \in [2, \infty)$ , setting threshold to the output current of each element obtaining binary synapses, avoiding therefore disturbing noise effects [34]. In the following chapters of this work a detailed description of the SBPI will be provided, parallel to the study of a dedicated memristor circuitry proving its classification efficacy.

The introduction of memristors in dedicated circuitry and systems implementing this kind of algorithms, especially the SBPI, well renders the needed dynamics of the cells and the synapses that occur for their design and functioning. The combination of memristor theory with bio-inspired computing for machine learning set the path for *neuromorphic engineering* leading to [3]:

1. the utilization of brain-like, spike-based information encoding, computing and communication;
2. taking advantage of such spike-based information encoding to perform neuroscience-inspired spike based learning rules such as Spike-Timing-Dependent-Plasticity [35] and all their variants;
3. assemble arbitrary scale hierarchical systems by intercommunicating spike-driven computing modules (or local neuron populations) such as multi-layer

Deep Neural Networks structures [36] either in their purely feed-forward version or allowing weak or strong feedback interaction.

Several systems have been also developed through circuits non-memristive devices, especially CMOS technology, such as the SpiNNaker system [37]. The trend in any case is leading towards the development of hybrid CMOS/memristive and purely memristive devices [38, 39]. As a general overview from a physical hardware implementation point of view, boards and chips that exploit memristor technology are built with schemes similar to one reported in Figure 1.3.

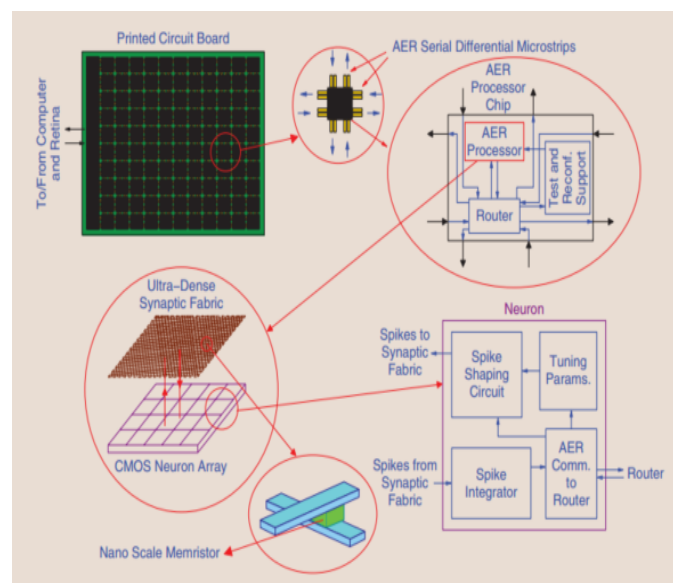


Fig. 1.3 Example of physical deployment of memristors in a PCB architecture. PCB boards contain many functional elements. The implementation of memristor crossbar arrays permits an agile computing and selection of the desired element. In figure is reported a typical example taken from the work of Serrano-Gotarredona *et al.* [40].

Memristive systems that implement bio-inspired algorithms may find various applications, as afore mentioned, for their high efficiency in processing big amounts of data. One field in which these devices can find a high use is bio-medicine and biomedical engineering. Itoh and Chua described an important equivalence between CAs and discrete time cellular neural networks (DTCNNs), which are assimilable to classic CNNs with the exceptions that the evolutive iterations of the cells in the network are processed at fixed discrete time points [41]. In their work they proved the possibility to use memristor-based circuitry in this kind of systems. The common

use of CAs resides in image processing, which in biomedical engineering is of central importance for the recognition of sane and pathological tissues.

Taking inspiration from the work of Itoh and Chua it was possible to determine a further equivalence between memristor CAs and memristive perceptrons exploiting SBPI. Taking the characteristics of both systems it is possible to perform image processing tasks. A device capable of taking pictures and processing them through the scheme here presented was developed for the analysis and assessment of chronic cutaneous lesions such as ulcers, wounds and escaræ. Proceeding with the chapters of this work the device will be presented proving the SBPI-CA equivalence and the high efficiency of classification given by the system through pre-clinical trials.

## 1.1 Description of the Work

This work presents a deep insight on memristors and memristive systems, based on a solid scientific background. From the here presented introduction it is possible to note that each step of the work leads to the next with the goal of developing a fruitful and realistic application of these systems proving that memristors can provide off the shelf solutions for up-to-date problems regarding core fields such as biomedical engineering.

### 1.1.1 Contributions to the Work

From an organization point of view the this work will begin with Chapter 2 where it is introduced the memristor theory starting from the one presented by Professor Leon Chua in 1971 and following, a deep insight on  $\varphi - q$  analysis of memristors and memristive devices other than the aforementioned memristor classification. Subsequently in the chapter is reported the use of  $\varphi - q$  models to better comprehend the rupturing and formation dynamics of the conductive filament of the HP memristor model (with an insight of the element's physical behaviour), and to obtain equivalent circuit models for PCMs and silicon nano-wires for memristive bio-sensing.

Chapter 3 provides a complete explanation of CNNs and bio-inspired algorithms for machine learning. Moreover a complete description on the SBPI algorithm is provided with a comparison with other existing procedures. In this chapter is

introduced the design of a dedicated memristor-based system implementing the SBPI. To prove that the use of memristors for its implementation the system was coded in SPICE for circuit simulations. Several efficiency essays were performed to tune the elements of the system and to prove its learning capability and efficacy. As it will be deeply described in the chapter the GBCM model was used to emulate memristors in the perceptron.

Concluding in Chapter 4 is reported an introduction to CAs and DTCNNs and their equivalence in order to demonstrate the obtaining of the equivalence of CAs and SBPI. The design of an innovative device is provided based on the merge of the two reported analysis schemes for automatic recognition, classification and assessment of cutaneous ulcers. Parallel, is reported the need for such systems based on medical literature and the proof of the actual classification and detection capability based on pre-clinical trials on more than 200 patients.

### 1.1.2 Author's Contribution to Papers

1. Jacopo Secco, Fernando Corinto, and Marius Orlowski. Physics of the rupturing mechanism for hp memristor in flux mode. In Proceedings of the International Conference on Numerical Analysis and Applied Mathematics 2014 (ICNAAM-2014), volume 1648, page 280004. AIP Publishing, 2015.
2. Marius Orlowski, Jacopo Secco, and Fernando Corinto. Chua's constitutive memristor relations for physical phenomena at metal-oxide interfaces. *Emerging and Selected Topics in Circuits and Systems*, IEEE Journal on, 5(2):143-152, 2015.
3. Jacopo Secco, Mario Biey, Fernando Corinto, Alon Ascoli, and Ronald Tetzlaff. Complex behavior in memristor circuits based on static nonlinear two-ports and dynamic bipole. In *Circuit Theory and Design (ECCTD)*, 2015 European Conference on, pages 1-4. IEEE, 2015.
4. Jacopo Secco and Fernando Corinto. Memristor-based cellular nonlinear networks with belief propagation inspired algorithm. In *2015 IEEE International Symposium on Circuits and Systems (ISCAS)*, pages 1522-1525. IEEE, 2015.
5. Jacopo Secco, Alessandro Vinassa, Valentina Pontrandolfo, Carlo Baldassi, and Fernando Corinto. Binary synapse circuitry for high efficiency learning al-

- gorithm using generalized boundary condition memristor models. In *Advances in Neural Networks: Computational and Theoretical Issues*, pages 369–374. Springer, 2015.
6. Jacopo Secco, Marco Farina, Danilo Demarchi, and Fernando Corinto. Memristor cellular automata through belief propagation inspired algorithm. In *2015 International SoC Design Conference (ISOCC)*, pages 211–212. IEEE, 2015.
  7. Jacopo Secco, Marco Farina, Danilo Demarchi, Fernando Corinto, and Marco Gilli. Memristor cellular automata for image pattern recognition and clinical applications. In *2016 IEEE International Symposium on Circuits and Systems (ISCAS)*, pages 1378–1381. IEEE, 2016.
  8. Jacopo Secco and Fernando Corinto. Memristor-based binary synapses for deep neural networks. *CNNA 2016*, 2016.
  9. Jacopo Secco, Marco Farina, and Selenu Orlando. **Patent:** Device and method of acquisition of medical images for ulcer analysis, IT102015000087450 2015.

## Chapter 2

# Memristor Theory: Device Modeling and Simulations

Memristors have become a widely studied technology since their theorization given in [1]. In the years a variety of models and devices have been developed with different characteristics given by their different intrinsic properties and the different fabrication ways and materials. Moreover a vast series of devices have been proved to show memristive effects such as ReRAMS, FeRAMS, MRAMS and most of all PCMs. In order to achieve the required know-how on memristors for their use and implementation in wider and more complex system it is necessary to develop a generalized simplified analysis model for their insertion in common circuit theory. One of the models that provides this capability is the  $\varphi - q$  analysis method [25] thanks to which it has been possible to arrive with a clear memristive device classification [26].

In the following sections of this chapter it will be presented the state of the art involving memristors, starting from Section 2.1 which introduces the original description given by Professor Chua in his 1971 paper. Following, a clear and complete description of the  $\varphi - q$  analysis method is provided with its relation regarding memristor classification. Concluding it will be presented the use of the  $\varphi - q$  analysis for the modeling of the behaviour of the HP memristor [2, 42] regarding the formation and rupturing of the conductive filament with a detailed insight of the device. Moreover the same kind of analysis has been performed for modeling and obtaining off-the-shelf equivalent circuit models of PCMs [28] and of

memristive bio-sensors based on silicon nano-wires (SiNW) [15], other than their classification regarding memristor theory.

## 2.1 Original Description

Resistors, Capacitors and Inductors are well known as the three fundamental two-terminal circuit elements. The equations that describe their behaviour represent the relationship between the four fundamental circuit variables: the *current* ( $i$ ), the *voltage* ( $v$ ), the *charge* ( $q$ ) and the *flux* ( $\varphi$ ). More precisely, resistors define the relationship between  $v$  and  $i$ , capacitors the one between  $q$  and  $v$  and inductors the one between  $\varphi$  and  $q$ . Moreover other two relationships out of the six possible reside in the definition of charge and flux [43] as:

$$q(t) = \int_{-\infty}^t i(\tau) d\tau, \quad (2.1)$$

$$\varphi(t) = \int_{-\infty}^t v(\tau) d\tau. \quad (2.2)$$

The memristor is the two terminal circuit element which describes the relationship between charge and flux and can be characterized by a  $\varphi - q$  curve. The name *memristor* derives from the contraction of *memroy* and *resistor* since as it will be shown later, the memristor can be described as a two-terminal non-linear resistor with memory. By definition these elements can be described by a relation  $g(\varphi, q) = 0$  and can be divided in two groups: charged controlled and flux controlled. In the first case the voltage across the memristor can be given by

$$v(t) = M(q(t))i(t), \quad (2.3)$$

where

$$M(q) = \frac{d\varphi(q)}{dq}. \quad (2.4)$$

On the other hand the current flowing through a charge controlled memristor can be computed as

$$i(t) = W(\varphi(t))v(t), \quad (2.5)$$

where

$$W(\varphi) = \frac{dq(\varphi)}{d\varphi}. \quad (2.6)$$

Comparing Equations (2.3) and (2.5) to Ohm's law it is possible to notice that  $M(\cdot)$  has the unit of resistance and  $W(\cdot)$  has the unit of conductance. As so henceforth they will be associated respectively to the names of *memristance* and *menductance*. Observing the previous equations it is possible to note that the memristance (menductance) depends at any time on the flux and charge which are respectively the time integrals of the voltage applied to, and the current flowing through the element. Though the memristor acts as an ordinary resistance at any time instant  $t_0$ , its resistance value depends on the complete *history* of the voltage and of the current, justifying the name memristor (as memory-resistor).

Five theorems and two definitions were postulated by Professor Chua in order to define the memristor and to prove the existence of the element. Here, for the maintenance the correct mathematical dialectics, will be reported the theorems and the definitions regarding memristors as written in [1].

*Theorem 1: Passivity Criterion.* A memristor characterized by a differentiable charge controlled  $\varphi - q$  curve is passive if, and only if, its incremental memristance  $M(q)$  is nonnegative; i.e.,  $M(q) > 0$ .

*Proof:* The instantaneous power dissipated by a memristor is given by

$$p(t) = v(t)i(t) = M(q(t))[i(t)]^2. \quad (2.7)$$

Hence, if the incremental memristance  $M(q) > 0$ , then  $p(t) > 0$  and the memristor is obviously passive. To prove the converse, suppose that there exists a point  $q_0$  such that  $M(q_0) < 0$ . Then the differentiability of the  $\varphi - q$  curve implies that there exists an  $\varepsilon > 0$  such that  $M(q_0 + \Delta q) < 0$ ,  $|\Delta q| < \varepsilon$ . Now let us drive the memristor with a current  $i(t)$  which is zero for  $t < \hat{t}$  and such that  $q(t) = q_0 + \Delta q(t)$  for  $t \geq t_0 > \hat{t}$  where  $|\Delta q(t)| < \varepsilon$ ; then  $\int_{-\infty}^t p(\tau)d\tau < 0$  for sufficiently large  $t$ , and hence the memristor is active. ■

*Theorem 2: Closure Theorem.* A one-port containing a memristor is equivalent to a memristor.

*Proof:* Letting  $i_j$ ,  $v_j$ ,  $q_j$ , and  $\varphi_j$  denote the current, voltage, charge, and flux-linkage of the  $j$ -th memristor, where  $j = 1, 2, \dots, b$ , and letting  $i$  and  $v$  denote the port current and port voltage of the one-port, then we can write  $(n - 1)$  independent KCL (Kirchhoff current law) equations (assuming the network is connected); namely,

$$\alpha_{j0}i + \sum_{k=1}^b \alpha_{jk}i_k = 0 \quad j = 1, 2, \dots, n - 1 \quad (2.8)$$

where  $\alpha_{jk}$  is either 1,  $-1$ , or 0,  $b$  is the total number of memristors, and  $n$  is the total number of nodes. Similarly, we can write a system of  $(b - n + 2)$  independent KVL (Kirchhoff voltage law) equations:

$$\beta_{j0}v + \sum_{k=1}^b \beta_{jk}v_k = 0 \quad j = 1, 2, \dots, b - n + 2 \quad (2.9)$$

where  $\beta_{jk}$  is either 1,  $-1$ , or 0. If we integrate each equation in (2.8) and (2.9) with respect to time and then substitute  $\varphi_k = \varphi_k(q_k)$  for  $\varphi_k$  in the resulting expressions, we obtain

$$\sum_{k=1}^b \alpha_{jk}q_k = Q_j - \alpha_{j0}q \quad j = 1, 2, \dots, n - 1 \quad (2.10)$$

$$\beta_{j0}\varphi + \sum_{k=1}^b \beta_{jk}\varphi_k(q_k) = \Phi_j \quad j = 1, 2, \dots, b - n + 2 \quad (2.11)$$

where  $Q_j$  and  $\Phi_j$  are arbitrary constants of integration. Equations (2.10) and (2.11) together constitute a system of  $(b + 1)$  independent nonlinear functional equations in  $(b + 1)$  unknowns. Hence, solving for  $\varphi$ , we obtain a relation  $f(q, \varphi) = 0$ . ■

*Theorem 3: Existence and Uniqueness Theorem.* Any network containing only memristors with positive incremental memristances has one, and only one, solution.

*Proof:* Since the governing equations of a network containing only memristors are identical in form to the governing equations of a network containing only nonlinear resistors, the proof follows *mutatis mutandis* the well-known proof given in [44, 45]. ■

*Definition 1:* it is defined the action (coaction) associated with a chargecontrolled (flux-controlled) memristor to be the integral

$$A(q) \equiv \int_0^q \varphi(q) dq \quad \left( \hat{A}(\varphi) \equiv \int_0^\varphi q(\varphi) d\varphi \right). \quad (2.12)$$

Consider now a pure memristor network  $N$  containing  $n$  nodes and  $b$  branches. Let  $T$  be a *tree* of  $N$  and  $L$  its associated *cotree*. Let us label the branches consecutively starting with the tree elements and define  $\boldsymbol{\varphi} = (\varphi_1, \varphi_2, \dots, \varphi_b)^t$ ,  $\mathbf{q} = (q_1, q_2, \dots, q_b)^t$ ,  $\boldsymbol{\varphi}_T = (\varphi_1, \varphi_2, \dots, \varphi_{n-1})^t$ , and  $\mathbf{q}_L = (q_n, q_{n+1}, \dots, q_b)^t$ . It is well known that either  $\boldsymbol{\varphi}_T$  or  $\mathbf{q}_L$  constitutes a complete set of variables in the sense that  $\boldsymbol{\varphi} = \mathbf{D}^t \boldsymbol{\varphi}_T$  and  $\mathbf{q} = \mathbf{B}^t \mathbf{q}_L$ , where  $\mathbf{D}$  and  $\mathbf{B}$  are the fundamental cut-set matrix and the fundamental loop matrix, respectively [46].

*Definition 2:* it is defines the total action  $\Lambda(\mathbf{q}_L)$  [total coaction  $\hat{\Lambda}(\boldsymbol{\varphi}_T)$ ] associated with a network  $N$  containing charge-controlled (flux-controlled) memristors to be the scalar function

$$\Lambda(\mathbf{q}_L) = A \circ (\mathbf{B}^t \mathbf{q}_L) \quad \hat{\Lambda}(\boldsymbol{\varphi}_T) = \hat{A} \circ \mathbf{D}^t \boldsymbol{\varphi}_T \quad (2.13)$$

where

$$A = A(\mathbf{q}) = \sum_{j=1}^b A_j(q_j) = \text{sum}_{j=1}^b \int_0^{q_j} \varphi_j(q_j) dq_j \quad (2.14)$$

$$\hat{A} = \hat{A}(\boldsymbol{\varphi}) = \sum_{j=1}^b \hat{A}_j(\varphi_j) = \text{sum}_{j=1}^b \int_0^{\varphi_j} q_j(\varphi_j) d\varphi_j \quad (2.15)$$

and where  $\circ$  denotes the "composition" operator.

*Theorem 4: Principle of Stationary Action (Coaction):* A vector  $\mathbf{q}_L = \mathbf{Q}_L(\boldsymbol{\varphi}_T = \boldsymbol{\Phi}_t)$  is a solution of a network  $N$  containing only charge-controlled (flux-controlled) memristors if, and only if, it is a *stationary point* of the total action  $\Lambda(\mathbf{q}_L)$  [total coaction  $\hat{\Lambda}(\boldsymbol{\varphi}_T)$ ] associated with  $N$ ; i.e., the gradient of  $\Lambda(\mathbf{q}_L)$  ( $\hat{\Lambda}(\boldsymbol{\varphi}_T)$ ) evaluated in  $\mathbf{Q}_L(\boldsymbol{\Phi}_T)$  is zero:

$$\partial \Lambda(\mathbf{q}_L) / \partial \mathbf{q}_L \big|_{\mathbf{q}_L = \mathbf{Q}_L} = 0 \quad \partial \hat{\Lambda}(\boldsymbol{\varphi}_T) / \partial \boldsymbol{\varphi}_T \big|_{\boldsymbol{\varphi}_t = \boldsymbol{\Phi}_T} = 0. \quad (2.16)$$

*Proof:* It suffices to prove the charge-controlled case since the flux-controlled case will then follow by duality. Taking the gradient of  $\Lambda(\mathbf{q}_L)$  and applying the chain rule for differentiating composite functions, we obtain

$$\begin{aligned}\partial\Lambda(\mathbf{q}_L)/\partial\mathbf{q}_L &= \partial A \circ (\mathbf{B}^t \mathbf{q}_L) / \partial \mathbf{q}_L = \\ &= \mathbf{B} \partial A(\mathbf{q}) / \partial \mathbf{q} |_{\mathbf{q}=\mathbf{B}^t \mathbf{q}_L} = \mathbf{B} \boldsymbol{\varphi} \circ (\mathbf{B}^t \mathbf{q}_L).\end{aligned}\quad (2.17)$$

But the expression  $\mathbf{B} \boldsymbol{\varphi} \circ (\mathbf{B}^t \mathbf{q}_L) = 0$  since this is simply the set of KVL equations written in terms of  $L$ . Consequently, any vector  $\mathbf{Q}_L$  is a solution of  $N$  if, and only if, it is a stationary point of  $\Lambda(\mathbf{q}_L)$ . ■

*Theorem 5: Order of Complexity:* Let  $N$  be a network containing resistors, inductors, capacitors, memristors, independent voltage sources, and independent current sources. Then the order of complexity  $m$  of  $N$  is given by

$$m = (b_L + b_C + b_M) - (n - M + n_{CE} + n_{LM}) - (\hat{n}_M + \hat{n}_{LJ} + \hat{n}_{CM}) \quad (2.18)$$

where  $b_L$  is the total number of inductors;  $b_C$  is the total number of capacitors;  $b_M$  is the total number of memristors;  $n_M$  is the number of independent loops containing only memristors;  $n_{CE}$  is the number of independent loops containing only capacitors and voltage sources;  $n_{LM}$  is the number of independent loops containing only inductors and memristors;  $\hat{n}_M$  is the number of independent cut sets containing only memristors;  $\hat{n}_{LJ}$  is the number of independent cut sets containing only inductors and current sources;  $\hat{n}_{CM}$  is the number of independent cut sets containing only capacitors and memristors.

*Proof:* It is well known that the order of complexity of an RLC network is given by  $m = (b_L + b_C) - n_{CE} - \hat{n}_{LJ}$ . It follows, therefore that for an RLC-memristor network with  $n_m = n_{LM} = \hat{n}_M = \hat{n}_{CM} = 0$ , each memristor introduces a new state variable and we have  $m = (b_L + b_C + b_M) - n_{CE} - \hat{n}_{LJ}$ . Observe that a *constraint* among the state variables occurs whenever an independent loop consisting of elements corresponding to those specified in the definition of  $n_M$  and  $n_{LM}$  is present in the network. It is assumed that the algebraic sum of charges around any loop (flux linkages in any cut set) is zero. Similarly, a constraint among the state variables occurs whenever an independent cut set consisting of elements corresponding to those specified in the definition of  $\hat{n}_M$  and  $\hat{n}_{CM}$  is present in the network. Since

each constraint removes one degree of freedom each time this situation occurs, the maximum order of complexity ( $b_L + b_C + b_M$ ) must be reduced by one. ■

Thanks to the above reported theorems and definitions, it was possible to state the possibility of existence of memristors. Chua was able to demonstrate their coherence with conventional circuit theory and most of all their adhesion to canonic physics. For the sake of completeness it is an obligation to report that the first memristor, intended as singular physical device, was developed more than thirty years later [2] than the postulation of these theorems by L.O. Chua. He was able to go over this absence using mutators [47]. Through mutators it was possible for him to realize a memristor with any prescribed  $\varphi - q$  ( $f(\varphi, q) = 0$ ) curve connecting an appropriate non-linear resistor, capacitor or inductor by transforming the respective  $v_R - i_R$  ( $f(v_R, i_R) = 0$ ),  $\varphi_L - i_L$  ( $f(\varphi_L, i_L) = 0$ ) and  $v_C - q_C$  ( $f(v_C, q_C) = 0$ ) curves. The complete list of the mutators used by Professor Chua are represented in Figure 2.1.

As it will be demonstrated in the next sections of this work,  $v - i$  curves are not to be considered fully descriptive for memristors and memristive devices. Considering equations (2.3) and (2.5) the memductance and the memristance depend on the incremental charge and flux which are respectively the time integrals of the current flowing through the device and of the voltage applied. Due to this fact memristors are to be considered as non-linear resistors (in the  $\varphi - q$  domain), that behave responding not to the single voltage applied or to the single current value at any instant  $t_0$  (case in which the device acts like a passive linear resistor, as afore mentioned), but to all their previous values related to time. Though this is clear, memristors show a common peculiar dynamic described by a common family of  $v - i$  curves named "pinched hysteresis loop" [14]. Commonly the loop is pinched in the origin when considering ideal memristor, but in some cases such as in recently built memristive devices based on  $Ag/SiO_2/Pt$  may show non-zero pinched phenomenon, therefore showing nano-battery effect [22]. Figure 2.2 shows an example of a typical memristor hysteresis pinched in the origin. It can be seen from the figure that the curve changes according to the frequency of the input waveform. This particular phenomenon is very common in a series of memristors and memristive devices due to physical effects of the materials of which they are built [23, 24, 48–51], which typically leads them to behave more and more similarly to a generic resistor rather than to a memristor.

	TYPE	SYMBOL AND CHARACTERIZATION	TRANSMISSION MATRIX $\begin{bmatrix} V_1 \\ I_1 \end{bmatrix} = T(p) \begin{bmatrix} V_2 \\ -I_2 \end{bmatrix}$	BASIC REALIZATIONS USING CONTROLLED SOURCES	
M - R MUTATOR	1	$\begin{aligned} (q, \varphi) &\leftrightarrow (i_R, v_R) \\ v_1 &= \frac{d\varphi_2}{dt} \\ i_1 &= -\frac{dq_2}{dt} \end{aligned}$	$T_{MR_1}(p) = \begin{bmatrix} p & 0 \\ 0 & p \end{bmatrix}$		
	2	$\begin{aligned} (q, \varphi) &\leftrightarrow (v_R, i_R) \\ v_1 &= -\frac{dq_2}{dt} \\ i_1 &= \frac{d\varphi_2}{dt} \end{aligned}$	$T_{MR_2}(p) = \begin{bmatrix} 0 & p \\ p & 0 \end{bmatrix}$		
M - L MUTATOR	1	$\begin{aligned} (q, \varphi) &\leftrightarrow (i_L, \varphi_L) \\ v_1 &= v_2 \\ i_1 &= -\frac{d i_2}{dt} \end{aligned}$	$T_{ML_1}(p) = \begin{bmatrix} 1 & 0 \\ 0 & p \end{bmatrix}$ (Identical to $T_{CR_1}(p)$ of a Type 1 C-R MUTATOR)		
	2	$\begin{aligned} (q, \varphi) &\leftrightarrow (\varphi_L, i_L) \\ v_1 &= -\frac{d i_2}{dt} \\ i_1 &= v_2 \end{aligned}$	$T_{ML_2}(p) = \begin{bmatrix} 0 & p \\ 1 & 0 \end{bmatrix}$ (Identical to $T_{LR_2}(p)$ of a Type 2 L-R MUTATOR)		
M - C MUTATOR	1	$\begin{aligned} (q, \varphi) &\leftrightarrow (q_C, v_C) \\ v_1 &= \frac{d v_2}{dt} \\ i_1 &= -i_2 \end{aligned}$	$T_{MC_1}(p) = \begin{bmatrix} p & 0 \\ 0 & 1 \end{bmatrix}$ (Identical to $T_{LR_1}(p)$ of a Type 1 L-R MUTATOR)		
	2	$\begin{aligned} (q, \varphi) &\leftrightarrow (v_C, q_C) \\ v_1 &= -i_2 \\ i_1 &= \frac{d v_2}{dt} \end{aligned}$	$T_{MC_2}(p) = \begin{bmatrix} 0 & 1 \\ p & 0 \end{bmatrix}$ (Identical to $T_{CR_2}(p)$ of a Type 2 C-R MUTATOR)		

Fig. 2.1 Figurative list of the mutators used by Chua to give the first proof of the existence of memristors in 1971. The reported figure is taken directly from [1].

## 2.2 Flux-Charge Analysis Method and Memristor Classification

Memristors and memristive devices show a particular fingerprint named pinched hysteresis loop (Figure 2.2). This particular curve is used to assess if a particular device can be classified as a memristor or if it shows particular memristive behaviour

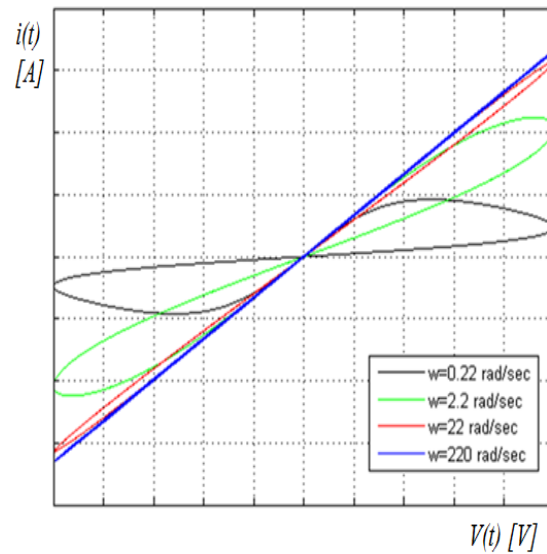


Fig. 2.2 Example of a typical memristor pinched loop  $v - i$ . It is possible to note from the given example that the loop decreases, as so the memristor acted more and more as a generic resistor rather than a memristor. This phenomenon is given by the physical properties of the materials of which some memristive devices are built with.

[14]. The pinched loop describes the typical non-linear behaviour if a memristor in the  $v - i$  domain. As can be noted from the figure, though the hysteresis is affected by a series of factors that can modify the form of the curve itself. The example here reported shows that the loop changes its shape increasing the frequency if the input signal waveform. This is a typical phenomenon presented by memristive devices and it is given by a series of physical effects due to the technological realization of the elements. One example (that will be presented in details in the following section of this chapter) is the HP memristor [2]. The conductive filament is created by the migration of oxygen vacancies in the  $TiO_2$  bulk that acts as a *solid electrolyte*. The migration of the vacancies suffers from a *tau* effect given by the material. Increasing the frequency of the waveform, it is not provided the sufficient time for the filament to reach the other electrode and therefore the memristor acts more and more as a linear passive resistor.

Moreover the pinched loop is also affected by the amplitude of the input signal. Higher or lower voltages (currents) in flux (charge) controlled devices generate different responses leading to a change of the shape of the  $v - i$  curve. At the end the constitutive materials of the various elements have a great effect on the resulting

curve. A broad range of fabrication techniques and materials lead to an equal broad range of behavioural curves [17, 18].

The trend in recent years led to the use of memristors and memristor-based circuits are widely exploited, for example to render novel classes of amplifiers, filters, oscillators, logic gates and artificial synapses in neuromorphic engineering [52–54]. This developing trend in memristive systems led to the necessity to find ease-of-use analytical methods that permit a more rapid circuit implementation of these elements. From what is mentioned above, it is clear that an analysis of these systems in the  $v - i$  domain results incomplete for the proper understanding of the on-linear dynamics that characterize memristive devices.

Fernando Corinto and Mauro Forti introduced the use of Kirchoff's Flux and Charge Laws ( $K\phi L$  and  $KqL$ ) for the analysis of memristor-based circuits instead of the common Kirchoff's Voltage and Current Laws (KVL and KCL) [25]. As mentioned in Chapter 1 the analysis of the dynamics in the  $\phi - q$  domain leads to the following advantages with respect to the  $v - i$  models:

1. more simple analysis of non-linear dynamics and bifurcations by means of smaller ordinary differentia equations (ODEs);
2. a clear understanding of the effects of initial conditions.

The work presented in [25] serves as a support of the introduction of the complete classification of memristors and memristive devices provided in [26], which will be explained in details forward in the chapter and introduced in Chapter 1. The classification given by Corinto, Civalleri and Chua is based in terms of pairs of electronic variables  $(v(t), i(t))$  and  $(\phi(t), q(t))$  and is the latest noteworthy example of a unified description of memristors, or in other words, without any regard of the technological provenance of the various elements. In addition it is proven in the same work (and will be subsequently shown) that the same memristor can return a variety of responses, conducting to a family of  $v - i$  curves depending on the different input waveforms given to the device.

The scope of the work by Corinto and Forti is to provide a standardized tool for circuit design of memristor-based systems. Memristors, as afore mentioned, have found a wide use as programmable memories due to their properties, and it is clear that systems that implement them are designed to provide a fine resolution

of the programming. Even in the case in which memristors that are used as volatile memories (exception of programming means) it results of high importance the deep comprehension of their non-linear dynamics. In the first case memristors are subject to pulse programming. Low voltages are used during their operations and high voltages are induced for setting the desired memristance. To do so hybrid CMOS/memristor circuits have been developed though their compatibility is still under investigation. On the other hand their nonlinear dynamic behaviour is highly exploited in oscillatory and chaotic circuits [55–57]. Classic analysis of these circuits leads to large systems of Differential Algebraic Equations (DAEs), whose solution requires powerful and efficient computation tools.

To best explain  $\varphi - q$  analysis, in the following paragraph will be introduced the class of non-linear circuits noted as  $\mathcal{LM}$  and a circuit analysis example on one specimen of this class taken from [25].

### 2.2.1 $\mathcal{LM}$ Circuit Class Introduction and Analysis

Circuits in the  $\mathcal{LM}$  class are constituted by ideal capacitors, inductors, resistors, current and voltage sources and memristors that can be either flux or charge controlled [25]. The application of these circuits starts at a fixed time point  $-\infty < t_0$ . The goal of the analysis here reported is to understand the behaviour of these circuits for  $t \geq t_0$ . one of the simplest example of circuit of this class is the one reported in Figure 2.3. When the the switches  $S_1$  and  $S_3$  are open and  $S_2$  is closed the proposed circuit results in a simple memristor-capacitor (M-C) circuit. in figure the blocks  $\mathcal{L}_a$  and  $\mathcal{L}_b$  represent any linear network composed by resistors, inductors, capacitors, voltage and current sources.

For the correct analysis of the proposed circuit it is necessary to set proper initial conditions for the state variables  $\varphi_M(t)$  and  $v_C(t)$  that will be noted as  $\varphi_M(t_0) = \varphi_{M_0}$  and  $v_C(t_0) = v_{C_0}$  respectively. It has been already explained the conditions by which the circuit is equivalent to a standard M-C circuit. On the other hand when  $S_1$  and  $S_3$  are closed and  $S_2$  is open it describes the evolution of the state variables  $\varphi_M(t)$  and  $v_C(t)$  for  $t < t_0$ . By means of the opening and closing of the switches in the two described fashions, it is clear that the initial conditions are set independently between the obtained circuits  $\mathcal{L}_a - M$  and  $\mathcal{L}_b - C$ . For the proposed example we consider the elements M and C not energized at  $t = -\infty$ .

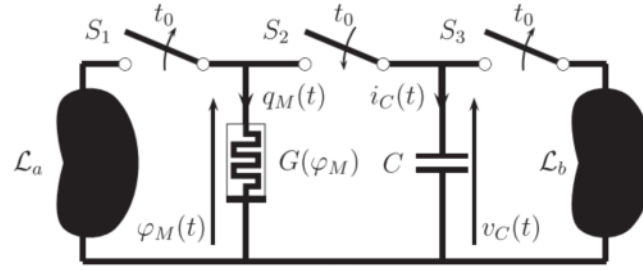


Fig. 2.3 Example of an  $\mathcal{LM}$  circuit.  $S_1$ ,  $S_2$  and  $S_3$  are switches that connect (or disconnect) the memristor  $M$  and the capacitor  $C$  with the linear networks  $\mathcal{L}_a$  and  $\mathcal{L}_b$ . By closing  $S_2$  and opening the rest of the switches, the reported circuit becomes an M-C circuit. The figure is taken from [25].

From the considerations made it is possible to derive that  $\varphi_M(t)$  and  $v_C(t)$  obey the Initial Value Problem (IVP) for a second order ODE:

$$C \frac{dv_C(t)}{dt} = -G(\varphi_M(t))v_C(t); \quad (2.19)$$

$$\frac{d\varphi_M(t)}{dt} = v_C(t); \quad (2.20)$$

resulting in (taking into account the initial conditions described before and the considerations regarding them):

$$-G(\varphi_M(t))v_C(t) = -\frac{df(\varphi_M)}{d\varphi_M} \frac{d\varphi_M(t)}{dt} = -\frac{d\varphi_M(t)}{dt}. \quad (2.21)$$

As a result of integrating (2.19) over  $(t_0, t)$ , where  $t \geq t_0$  it is obtained

$$C(v_C(t) - v_{C_0}) = -(f(\varphi_M(t)) - f(\varphi_{M_0})) = -(q_M(t) - q_M(t_0)) \quad (2.22)$$

which is a twofold.

The non-linearity of the  $\mathcal{LM}$  circuit can be derived from equations (2.19) and (2.22) from which it can be written an IVP for a first order ODE:

$$\frac{d\varphi_M(t)}{dt} = -\frac{f(\varphi_M(t)) + f(\varphi_{M_0})}{C} + v_{C_0} \quad (2.23)$$

where the state variable  $\varphi_M(t)$  and the initial conditions of the system appear as constant inputs. From this result it is clear that an IVP for a second order ODE in the  $v - i$  domain can be easily transformed do an IVP for a first order ODE in the

$\varphi - q$  domain. In addition the key electrical variable in equation (2.23) is  $\varphi_M(t)$  concluding that the sole variables that are necessary for the analysis of this class of circuits are  $(\varphi_M, q_M)$ .

Moreover equation (2.22) is the result of the integration of equation (2.19), in other words integrating the behavioural relation computed through the KCL analysis of the circuit obtaining the KqL. The KqL states that the algebraic sum of the *incremental charge* in a closed circuit is zero. For the property of duality the same considerations can be done amongst the KVL and K $\varphi$ L. From this analysis it is clear that the main pillars of the  $\varphi - q$  analysis are:

1. the use of K $\varphi$ L and KqL in terms of incremental flux and charge  $\varphi_k(t; t_0) = \varphi_k(t) - \varphi_k(t_0)$  and  $q_k(t; t_0) = q_k(t) - q_k(t_0)$  for any  $t \geq t_0$ , where the flux  $\varphi_k$  and the charge  $q_k$  are obtained from the integration voltage and the current ( $v_k$  and  $i_k$  respectively) in  $(t_0, t)$  flowing through a generic  $\mathcal{LM}$  circuit;
2. the use of constitutive relations expressed according to the same electrical variables.

The difference between the incremental flux (charge) and the flux (charge) defined in (2.2) ( (2.1)) are the integration extremes of integration. They result in being equivalent if and only if  $t_0 \rightarrow -\infty$  [25] and the circuit topology results in being invariant for any  $t \in (-\infty, \infty)$ .

### 2.2.2 Insight on Kirchoff's Incremental Laws

Considering a circuit that can be included in the  $\mathcal{LM}$  class with a number of two-terminal elements equal to  $l$  and  $n$  nodes, it is possible to write  $n - 1$  fundamental cutset equation and  $l - n + 1$  fundamental loop equations as

$$\mathbf{A}\mathbf{i}(t) = 0 \quad \text{where} \quad \mathbf{A} \in \mathbb{R}^{(n-1) \times l}; \quad (2.24)$$

$$\mathbf{B}\mathbf{v}(t) = 0 \quad \text{where} \quad \mathbf{B} \in \mathbb{R}^{(l-n+1) \times l}. \quad (2.25)$$

Where  $\mathbf{A}$  and  $\mathbf{B}$  are the reduced incidence and the reduced loop matrices respectively. By integrating (2.24) and (2.25) between  $t_0$  and  $t \geq t_0$  it is obtained

$$\mathbf{A}\mathbf{q}(t) = \mathbf{A}\mathbf{q}t_0; \quad (2.26)$$

$$\mathbf{B}\boldsymbol{\varphi}(t) = \mathbf{B}\boldsymbol{\varphi}t_0. \quad (2.27)$$

Equations (2.26) and (2.27) in order to be computed require all the initial conditions  $\mathbf{q}(t_0)$  and  $\boldsymbol{\varphi}(t_0)$ . Amongst them are required the initial conditions  $q_{C_k}(t_0) = C_k v_{C_k}(t_0)$  and  $\varphi_{L_k}(t_0) = L_k i_{L_k}(t_0)$ . These variables are easy to be measured via voltmeter or ammeter in a. On the other hand the initial conditions  $q_{L_k}(t_0) = \int_{-\infty}^{t_0} i_{L_k}(t) dt$  and  $\varphi_{C_k}(t_0) = \int_{-\infty}^{t_0} v_{C_k}(t) dt$  cannot be measured by the same means. The only way to have knowledge of  $q_{L_k}$  and of  $\varphi_{C_k}$  is by having knowledge about the system's history beginning from  $t = -\infty$ .

For this reason the K $\varphi$ L and KqL can be made independent from the initial conditions utilizing the incremental charges and fluxes regarding the circuit. KqL can be reduced to a simpler form as:

$$\mathbf{A}\mathbf{q}(t; t_0) = 0, \quad (2.28)$$

and in the same way K $\varphi$ L:

$$\mathbf{B}\boldsymbol{\varphi}(t; t_0) = 0. \quad (2.29)$$

It is known that these equations ((2.28) and (2.29)) give in overall  $l$  independent topological constraints on  $\mathbf{q}(t; t_0)$  and  $\boldsymbol{\varphi}(t; t_0)$  in the  $\varphi - q$  domain. The condition that has to be met when using Kirchoff's incremental laws is that it is necessary to have the incremental charge and flux description of all the elements in the circuit. A complete overview of Kirchoff's incremental flux and charge laws is provided in [25].

### 2.2.3 Memristor Classification Based on $\varphi$ and $q$

As explained in paragraph 2.2.1, memristors and memristor-based circuits are better described by models that reside in the  $\varphi - q$  domain rather than with  $v - i$  based models. In the same paragraph were explained the actual advantages of such models. Related to the same theory Corinto, Civalleri and Chua described an accurate classi-

fication of memristors and memristive devices that is regardless of the technological procedures that brought to the development of the variety of devices introduced in the above chapters of this work [26].

As afore explained the classical fingerprint used to recognize memristors and devices that show memristive behaviour is the pinched hysteresis loop (Figure 2.2). These particular kinds of  $v - i$  curves though present several difficulties if used to classify devices since their shape is strongly dependant on the on the amplitude and the frequency of the input signal given to the device (both for charge and flux controlled memristors). Moreover this fingerprint does not impose further conditions to the actual behaviour of the analyzed devices; as a matter of fact Chua reported in [14]: «*Pinched loops are the hallmarks of all memristors, ideal or otherwise*». All in all the pinched hysteresis loop can be considered as a useful tool for identifying weather a given element can or cannot be considered a memristor, but due to its variability based on the technological configuration (i.e. the physical phenomena that give rise to the memristive behaviour) of the element and the input signal's amplitude/frequency dependance it is required an alternative method of classification.

The equation  $\dot{\mathbf{x}} = g(u, \dot{u}, \mathbf{x})$  introduced in Chapter 1, introduces the ODE governing the *internal vector*  $\mathbf{x}$  which contains the state variables, and the non-state variables that depend form them, of a generic memristor element [26]. As afore mentioned  $u$  is the input to the element, that for memristors is represented by  $\varphi$  for flux controlled or  $q$  for charge controlled devices. Exploiting the considerations made in [1, 14, 58] it is possible to state the following two *definitions* regarding the *static and the dynamic characteristics* of a current controlled extended memristor.

*Definition 3:* considering a current controlled extended memritor, which is a two-terminal element defined thourgh current and voltage momentum (i.e.  $q$  and  $\varphi$  respectively) by the following equations:

$$\mathbf{F}(\varphi, q, i, \mathbf{x}) = 0; \quad (2.30)$$

$$\dot{\mathbf{x}} = \mathbf{g}(q, i, \mathbf{x}); \quad (2.31)$$

$$\dot{q} = i; \quad (2.32)$$

where  $\mathbf{F}(\cdot, \cdot, \cdot, \cdot) = 0$  is the *static characteristic equation*, with the constraint  $i = 0 \rightarrow v = 0, \forall \mathbf{x}$ , it is possible to define the *static characteristic*  $\tilde{\mathcal{F}}$  which is the collection

of points that satisfies equation (2.30) as:

$$\tilde{\mathcal{F}} = \{(\varphi, q, i, \mathbf{x}) \in \mathbb{R}^{(n+3)} : \mathbf{F}(\varphi, q, i, \mathbf{x}) = 0\}. \quad (2.33)$$

It is possible, moreover from equation (2.30), to redefine the static characteristic equation in terms of  $\varphi$  as:

$$\varphi = \mathbf{f}(q, i, \mathbf{x}), \quad (2.34)$$

with the same ODEs as the ones reported in equations (2.31) and (2.32) so that the static characteristic turns out to be:

$$\mathcal{F} = \{(\varphi, q, i, \mathbf{x}) \in \mathbb{R}^{(n+3)} : \varphi = \mathbf{f}(q, i, \mathbf{x})\}. \quad (2.35)$$

*Definition 4:* an extended memristor can be described in terms voltage  $v$  and current  $i$  by equations (2.31), (2.32), and the following:

$$v = \mathbf{R}(q, i, \mathbf{x})i, \quad (2.36)$$

if and only if  $\forall \mathbf{x}$  (taking into account equation (2.34))

$$\frac{\partial \mathbf{f}}{\partial i} i + \sum_{k=1}^n \frac{\partial \mathbf{f}}{\partial x_k} \dot{x}_k = L(q, i, \mathbf{x})\dot{i} + \mathbf{J}(q, i, \mathbf{x})\dot{\mathbf{x}} = 0, \quad (2.37)$$

where

$$\mathbf{R}(q, i, \mathbf{x}) = \frac{\partial \mathbf{f}(q, i, \mathbf{x})}{\partial q}; \quad (2.38)$$

$$L(q, i, \mathbf{x}) = \frac{\partial \mathbf{f}(q, i, \mathbf{x})}{\partial i}; \quad (2.39)$$

$$\mathbf{J}(q, i, \mathbf{x}) = \left( \frac{\partial \mathbf{f}(q, i, \mathbf{x})}{\partial x_1}, \dots, \frac{\partial \mathbf{f}(q, i, \mathbf{x})}{\partial x_n} \right); \quad (2.40)$$

$$\mathbf{J}_f(q, i, \mathbf{x}) = (\mathbf{R}(q, i, \mathbf{x}), L(q, i, \mathbf{x}), \mathbf{J}(q, i, \mathbf{x})). \quad (2.41)$$

In (2.41)  $\mathbf{J}_f$  is the Jacobian of the static characteristic equation ((2.34)), and  $\mathbf{J}$  is the part of  $\mathbf{J}_f$  with only the partial derivatives of the elements of the internal vector  $\mathbf{x}$ . The term  $\mathbf{J}\dot{\mathbf{x}}$  can be also seen as an external voltage source in series with the extended memristor which shows a pinched hysteresis loop in the origin. On the other hand  $\mathbf{R}$  is the memristance and  $L$  is to be considered as a parasitic inductive term in

series with the extended memristance which also presents a pinched hysteresis loop at the origin.

From equations (2.37), (2.38), (2.39), (2.40), and (2.41), it is possible to define the *dynamic characteristic*  $\mathcal{C}$  i.e.,

$$\mathcal{C} = \{(v(t), i(t)) \in \mathbb{R}^2 : v = \mathbf{R}(q, i, \mathbf{x})i, \dot{\mathbf{x}} = \mathbf{g}(q, i, \mathbf{x}), \dot{q} = i\}. \quad (2.42)$$

Regarding *Definitions 1 and 2*, introducing the concepts of internal state vector and parasitic effect, it is possible to define three classes of memristors [26]:

1. a *extended memristor* is a memristor that presents parasitic and has an internal state vector;
2. a *generic memristor* is a memristor with no parasitic effect;
3. an *ideal memristor* is a memristor with no parasitic effect and no state vector.

Tables 2.1, 2.2 and 2.3 summarize the above reported classes in terms of voltage and current compared with charge and flux.

Table 2.1 Extended Memristor

$(\varphi, q)$	$(v, i)$
$\varphi = \mathbf{f}(q, i, \mathbf{x})$	$v = \mathbf{R}(q, i, \mathbf{x})i$
$\dot{\mathbf{x}} = \mathbf{g}(q, i, \mathbf{x})$	$\dot{\mathbf{x}} = \mathbf{g}(q, i, \mathbf{x})$
$\dot{q} = i$	$\dot{q} = i$
$L(q, i, \mathbf{x})\dot{i} + \mathbf{J}(q, i, \mathbf{x})\dot{\mathbf{x}} = 0$	

Table 2.2 Generic Memristor

$(\varphi, q)$	$(v, i)$
$\varphi = \mathbf{f}(q, \mathbf{x})$	$v = \mathbf{R}(q, \mathbf{x})i$
$\dot{\mathbf{x}} = \mathbf{g}(q, i, \mathbf{x})$	$\dot{\mathbf{x}} = \mathbf{g}(q, i, \mathbf{x})$
$\dot{q} = i$	$\dot{q} = i$
$\mathbf{J}(q, i, \mathbf{x})\dot{\mathbf{x}} = 0$	

Table 2.3 Ideal Memristor

$(\varphi, q)$	$(v, i)$
$\varphi = \mathbf{f}(q)$	$v = \mathbf{R}(q)i$
$\dot{q} = i$	$\dot{q} = i$

Considering the above mentioned classification of memristors it is possible to note that  $\varphi - q$  models take into account also the behaviour of the device according to the state vector  $\mathbf{x}$ . This provides to the models a wider range of possible dynamics in the  $v - i$  domain. In other words for generic and extended memristors it is possible to describe through these models a *family of curves* in the flux-charge that lead to a family of curves in a voltage-current based approach. In [26] are shown simple examples of  $\varphi - q$  plains that generate from various values of the elements of  $\mathbf{x}$ .

## 2.3 Conductive Filament Formation and Rupturing in the HP Device

In this section Chua's constitutive memristor relations are constructed explicitly for Williams' famous  $TiO_2$  device [2] in terms of  $q = q(\varphi)$ . It is shown that this kind of model describes correctly the prevalent physical phenomena at the metal-oxide interfaces and is able to predict without any further parameters or assumptions, the dependence of  $V_{set}$  and  $V_{reset}$  voltages (i.e. the necessary voltages for the conductive filament formation and rupturing on the particular input voltage wave form. The impact of thermal (memory) effects on device performance has been explored and will be here shown through numerical simulations, other than the basic physical relations that describe the dynamics of the HP model.

### 2.3.1 General Overview of Memristor Models and HP Model Introduction

Since the 2008-dated sensational discovery of memristor behavior at the nano-scale, Hewlett Packard is credited for, a large deal of efforts have been spent in the research community to derive a suitable model able to capture the nonlinear dynamics of the nano-scale structures. The memristor was theoretically envisioned by Prof. Leon

O. Chua back in 1971 [1]. In Chua's description, a memristor is characterized by a nonlinear relation between charge and flux, i.e. the time integrals of current and voltage. It follows that the resistance of the memristor depends on the time evolution of the current flowing through the device or the voltage dropping across it, in case of charge or flux control, respectively. The memristor exhibits a set of unique fingerprints [5, 59, 60] among them a current–voltage pinched hysteretic loop under periodic bipolar excitation. However, as shown in [59], the current–voltage representation does not uniquely define a memristor. It is the charge–flux relation which does it instead [60].

A few years after the 1971 breakthrough the memristor was classified as the simplest element within a larger class of dynamical systems, namely the memristive systems [58]. It was recently proved [61] that although a classical purely passive electronic circuit made up of a nonlinearly-resistive two-port cascaded with a linear dynamic one-port acts as a volatile memristive system, a non-volatile memristive behavior may not be observed in any circuit employing conventional (i.e. non-memristive) circuit components. However, a sensational discovery, which took place at Hewlett Packard (HP) Labs [2] in 2008, demonstrated the existence of non-volatile memristive behavior in nature, specifically in a titanium dioxide-based nano-film. Since then, the industry has been engaged in the search for novel materials and technologies for the manufacture of memristive nano-structures [62]. In parallel, a considerable amount of work has been devoted to the development of mathematical models capable of reproducing the complex dynamics exhibited by the nano-devices. The availability of accurate, general and simple models is crucial for the investigation of the nonlinear dynamics of memristor–based circuits [55, 63], for the development of novel hybrid hardware architectures combining memory storage [64], for data processing in the same physical location and at the same time [65], and for explanation of the memristive behavior of biological systems [66, 67]. Many mathematical models of memristor nano-structures are reported in the literature (Pickett model [19], Joglekar's [68], Biolek's [16], Prodomakis' [69], the Boundary Condition Model (BCM) [70] and the Threshold Adaptive Memristor (TEAM) model [71]). The comparison between the memristor mathematical models and the Pickett's model is investigated in [72] through an optimization procedure based upon a smart combination of Simulated Annealing and Gradient Descent algorithms. The optimization strategy reveals that Biolek's model, the BCM and the TEAM model reproduce the memristive dynamics of the reference models more accurately than the other models.

The advantage of the first two models lies in their simplicity, although they are not based on Simmons' electric tunnel effect [73]. Moreover, the BCM is the only model for which a closed-form expression for the memristor state-flux relationship may be given under any input and initial condition combination [70]. The TEAM model reflects Simmons' physical model, but has a more complex mathematical formulation.

Windows-based memristor models have been very useful and versatile in describing memristor nano-structures regardless of the technological implementations [74]. As a memristor within a memristive circuit is subject to an unknown input, any useful memristive model has to be formulated independently of any particular current or voltage input. The only theoretically established way is to formulate a memristor model in terms of the charge and voltage flux [5, 25, 26].

Although a great amount of experimental and device modeling works has been produced, the limited repeatability of memristor devices has damped the technological advance in this field. Research community has mainly focused on switching memristor device in order to better understand the physical phenomena (e.g. the conductive filament forming and rupturing). Yang *et al.* [75] have investigated the critical role of Joule heating in the electro-forming of the filament based on oxygen vacancies. Alternative viewpoints of the Poole-Frenkel effect have been provided exploiting an energy trap-assisted tunneling memristor model [76]. A voltage dependence on the set/reset times of Hafnium oxide [77] and set/reset SPICE memristor models on Tantalum Oxide based [78] and Titanium Oxide based [79] have been also deeply studied.

The aim of this paper is to incorporate physical phenomena occurring at the oxide and metal interface into a charge-flux based memristor model. We focus on memristor devices made of metal-oxide-metal layers (i.e. similar to the Williams' famous  $TiO_2$  device).

In Figure 2.4 is presented the schematic representation of William's device [2]. The doped region, whose length is denoted by  $W$ , is the afore mentioned conductive filament. From the figure it is possible to understand the behaviour of the element through the variation over time of  $W$ :

1.  $W(t) = 0$  then  $R_{mem} = R_{off}$ ;
2.  $W(t) = D$  then  $R_{mem} = R_{on}$ ;

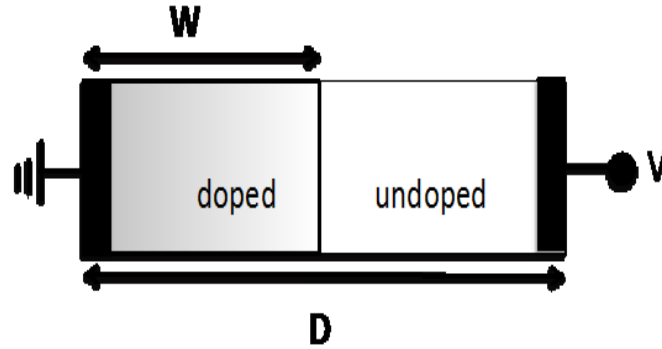


Fig. 2.4 Figurative example of the memristor developed at the HP labs by Strukov *et al.*  $W$  is the doped region of the device, or in other words the length of the conductive filament,  $D$  is the length of the whole device.  $V$  represents the input signal to the electrodes (full black areas at the devices' extremes), which according to Williams's configuration are made of platinum  $Pt$ .

$$3. \quad 0 < W(t) < D \text{ then } R_{mem} = R_{on}(W(t)/D) + R_{off}((D - W(t))/D);$$

with  $R_{off} > R_{on}$ . The case of  $R = R_{on}$  and sufficient negative flux should describe the rupturing or resetting of the device. As remarked already by Williams, his model as discussed before is based on purely ionic movement predicts that "even a small negative bias will switch it back to the off state". This questionable on general grounds, but is particularly troubling for the Williams model which assumes that ions are moving in the field of the doped region (i.e. with  $R_{on}$ ). When the device is in the ON state, the entire oxide is conductive where the erroneous Williams device should apparently apply. But it does not as Williams has stated himself. The situation is much more consistent with our model since the ions are driven into or away from the un-doped region by the electric field of the un-doped region. Since, when device is in  $R_{on}$ , there is no un-doped region, our model naturally implies that it cannot be applied to this situation because the driving force is zero. Hence, there is a need for a physical mechanism responsible for the rupturing. Such a model is developed in the following and brought into such an analytical form that the constitutive relation can be expressed as an analytic function.

Applying a negative flux to the device when in an ON state generates a current flow through the device in the border between the doped  $TiO_2$  and the  $Pt$  electrode. This current at the starting time point can be considered uniform over all the electrode. Probabilistically it is highly improbable that the doped  $TiO_2$  will detach completely

from the Pt border at the same time, thanks to the nature of the drift diffusive ionic transport. Asperities will generate on the  $TiO_2$  film, with regions that are not anymore in contact with the electrode, reducing considerably the conductive area. Thus, there will be a higher current density in the regions of the doped film still attached to the electrode. The higher current density will generate heating of the doped strand, and this heat will cause the rupture of the conductive filament. The rupturing point on the other hand is not to be considered on the Pt boundary, since its properties make the electrode a heat sink. The distance ( $\Delta$ ) between the electrode and the rupturing point (as described in details in paragraph 2.3.3) is function then of the thermal conductivity of the undoped region. The higher this value is, the easier to transport heat away from the filament, thus the higher is the distance  $\Delta$  from the Pt electrode. Also ambient temperature ( $T_0$ ) in which the memristor is confined affects the value of  $\Delta$ . The closer  $T_0$  is to the critical filament rupturing temperature, the closer is the rupturing point to the Pt surface.

In the following paragraphs it will be described in details the dependence of the filament's rupturing from  $\Delta$  and it will show also the model realized for the its formation. Moreover in paragraph 2.3.4 this section will show simulation results based on the presented model and its uniformity with experimental data present in literature.

### 2.3.2 Chua's Constitutive Memristor Relations for William's Device: Set Model

As in the case of Williams' analysis [2], we consider a thin semiconductor film of thickness  $D$  sandwiched between two metal contacts. The total resistance of the device is determined by two variable resistors connected in series. Specifically, the semiconductor film has a conductive region with a high concentration of dopants having low resistance  $R_{on}$ , and the remaining not-conductive portion has a low dopant concentration and much higher resistance  $R_{off}$ . The application of an external bias  $v(t)$  causes the boundary  $W(t)$  to move between the two regions. The resistance (or memristance  $M$ ) of the device composed of the conductive and non-conductive region is then given by [5]:

$$M(W(t)) = R_{on} \left( \frac{W(t)}{D} \right) + R_{off} \left( 1 - \frac{W(t)}{D} \right) \quad (2.43)$$

The boundary  $W(t)$  is the state variable for which a dynamical equation has to be established. In this paper and in contrast to Williams derivation [2], it is assumed that charged dopants drift into the undoped region by the electric field in the undoped region. Oxygen-deficient titanium oxide  $TiO_{2-x}$  is equivalent to a  $TiO_2V_x$ , a titanium oxide doped with oxygen vacancies  $V$ , which is known to be conductive, while the stoichiometric  $TiO_2$  is known to be insulating. Under a positive bias, an oxygen ion  $O_{2-}$  will migrate toward the anode leaving behind vacancies  $V$ . The additional vacancies are extending the doped region at the expense of the undoped region moving thus the boundary  $W$  toward the anode. William's derivation is based on the driving electric field in the conductive region. Accordingly, we obtain a different dynamical equation:

$$\frac{dW(t)}{dt} = \mu \frac{v(t)}{D - W(t)} \quad (2.44)$$

where  $\mu$  is the mobility of oxygen ions and  $v(t)$  is the time-dependent voltage waveform. The solution of the equation (2.44) is:

$$W(t) = D \left( 1 - \sqrt{1 - \frac{2DW_0 - W_0^2}{D^2} - \frac{2\mu}{D^2} \varphi(t)} \right) \quad (2.45)$$

with the initial boundary condition  $W_0 = W(0)$ . With this dependence of  $W(t)$  on flux, one can write the current-voltage relation as follows:

$$i(t) = \frac{v(t)}{M(W(t))} = \frac{1}{R_{on} \left( 1 + a \sqrt{1 - b \varphi(t)} \right)} \frac{d\varphi(t)}{dt} \quad (2.46)$$

where constants  $a$  and  $b$  are defined as:

$$a = \frac{R_{off} - R_{on}}{R_{on}} \frac{D - W_0}{D} \quad (2.47)$$

$$b = \frac{2\mu}{(D - W_0)^2}. \quad (2.48)$$

The time integral of the equation (2.46) can be solved analytically and yields:

$$q(\varphi) = \frac{2}{abR_{on}} \left[ \frac{1}{a} \ln \left( \frac{1 + a\sqrt{1 - b\varphi}}{1 + a} \right) - \sqrt{1 - b\varphi} + 1 \right]$$

The model described in equation (2.49) is valid for positive fluxes

$$0 \leq \varphi = \frac{1}{b}.$$

For the flux  $\varphi_{max} = 1/b$ ,  $W(t_{set}) = D$  and the memristor device is in a stable conductive state characterized by the resistance  $R_{on}$  for all  $t \geq t_{set}$ . It follows that, for all fluxes  $\varphi \geq \varphi_{max}$  we have:

$$q(\varphi) = \frac{\varphi}{R_{on}} \quad (2.49)$$

i.e. the memristor has become a conventional resistor.

As long the device is in a non-conductive state and  $W_0 > 0$  the model can be also applied for negative voltages and fluxes. In this case the boundary  $W(t)$  will be driven back to the grounded electrode, increasing thus the nonconductive portion of the solid electrolyte. In this case the negative flux will be bounded by  $\varphi_{min}$  given by:

$$\varphi_{min} = -\frac{(2DW_0 - W_0^2)}{2\mu} \leq \varphi \leq 0 \quad (2.50)$$

At  $\varphi_{min}$  the device reaches  $W(t_{reset}) = 0$  and the resistance of the device is in the stable OFF state characterized by  $R_{off}$  for all  $t \geq t_{reset}$ . It follows that, for negative fluxes smaller than  $\varphi_{min}$  (i.e.  $\varphi < \varphi_{min}$ ) we obtain:

$$q(\varphi) = \frac{\varphi}{R_{off}} \quad (2.51)$$

i.e. the memristor has become a conventional resistor.

All in all, the memductance,  $dq(\varphi)/d\varphi = G(\varphi)$ , of memristor device at a given initial  $W_0$  under positive and negative fluxes is given then by

$$G(\varphi) = \frac{1}{R_{on}} \quad W_0 = D, \quad \forall \varphi \geq \varphi_{max} \quad (2.52)$$

$$G(\varphi) = \frac{1}{R_{on} \left(1 + a\sqrt{1 - b\varphi(t)}\right)} \quad (2.53)$$

$$0 < W < D, \quad \varphi_{min} < \varphi < \varphi_{max}$$

$$G(\varphi) = \frac{1}{R_{off}} \quad W_0 = 0, \quad \forall \varphi \leq \varphi_{min}. \quad (2.54)$$

It should be noted that the Joules heat in the set model can be neglected. The set model describes the transition from the off-state to the very onset of the on-state. Because the entire set process evolves during various stages of the off-state, the currents are very low, and therefore the power dissipated in the device is very small, and, hence, can be neglected. Moreover, it is worth noting that the model is completely independent of the particular waveform of the input voltage. It is because of this independence, that it is able to predict the set voltage  $V_{set}$  as a function of a specific voltage waveform. This dependence will be discussed in the next section in more detail. Here, a typical behavior is analyzed for the experimentally prevalent linear voltage ramp  $r$  in units [V/s]. In case of a voltage ramp  $v(t) = rt$ , the time needed to SET the memristor device is given as  $t_{set} = V_{set}/r$ . Therefore:

$$\varphi_{max} = \int_0^{t_{set}} v(t) dt = \int_0^{\frac{V_{set}}{r}} rt dt = \frac{1}{2} \frac{V_{set}^2}{r} \quad (2.55)$$

Solving equation (2.55) for  $V_{set}$  and assuming that the critical flux  $\varphi_{max}$  that renders the device conductive at  $V_{set}$  is a constant for the device, one obtains

$$V_{set} = \sqrt{2r\varphi_{max}} \sim \sqrt{r}. \quad (2.56)$$

Indeed, it has been observed experimentally [80, 81] that the set voltage  $V_{set}$  increases with increasing ramp rate. Although, we don't have specific data for Williams device, the increase of  $V_{set}$  voltage as a function of the ramp rate is a universal observation in the resistive switching devices [82, 83]. A similar relation

can be derived for sinusoidal voltage signal  $v(t) = V_0 \sin(\omega t)$  where  $V_0$  is the voltage amplitude and  $\omega$  is the frequency; it is readily derived that

$$V_{set} = \sqrt{2\omega V_0 \phi_{max} - \omega^2 \phi_{max}^2} \quad (2.57)$$

It is clearly seen that  $V_{set}$  increases first with frequency for frequencies  $\omega < 2V_0/\phi_{max}$ , but it also depends also on the amplitude  $V_0$  of the signal.

$V_{set}$  has a maximum  $V_{set}^{max} = V_0$  at  $\omega = V_0/\phi_{max}$ .

When  $\omega$  approaches  $2V_0/\phi_{max}$ ,  $V_{set}$  decreases quickly to zero.

For  $\omega > 2V_0/\phi_{max}$  the device cannot be set. In Figure 2.5 a typical behavior of  $V_{set}$  as a function of frequency for three different amplitudes  $V_0 = \{1, 5, 20\}V$  is shown (for  $\phi_{max} = 0.01 [Vs]$ ). For  $V_0 = 1V$ , the device cannot be set beyond 100Hz, for  $V_0 = 20V$ , the device can be set at 1 kHz at rather large  $V_{set}$  of 17.3V.

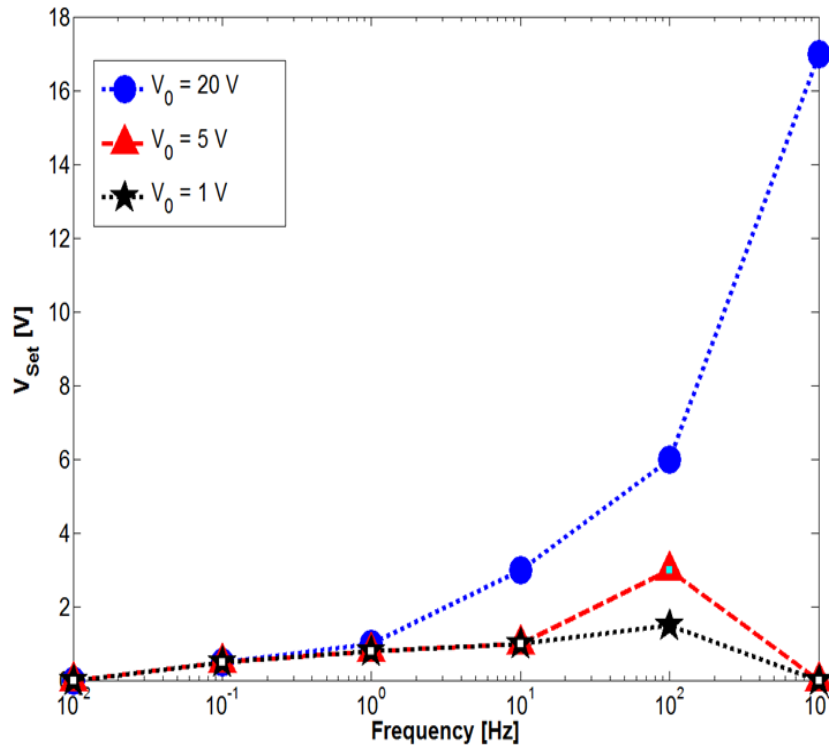


Fig. 2.5  $V_{set}$  as a function of frequency for three amplitudes  $V_0=1, 5, 20V$ .

When a memristor device is set at a given value  $V_{set} < V_0$ , in case of a sinusoidal signal this value  $V_{set}$  can be reached on the ascending branch of sine before  $V_0$  has

been reached, or in can be reached at the same voltage value but on the descending branch of sine, i.e. past the peak at  $V_0$ . Of course, critical flux will be different, with the flux for the latter case being significantly larger than for the first case. Such cases have been reported in the literature, e.g. Figure 3(c) in Williams' paper [2]. The voltage has reached its peak at  $1\text{ V}$  and is decreasing to set the device at  $0.65\text{ V}$ . From equation (2.57) and Figure 2.5 it can be seen that for a sinusoidal signal the device can be, in principle, set at  $0\text{ V}$  but a finite set time  $t_{set}$  corresponding to multiple of a half of a cycle. This is a special case when the critical flux has been reached when the voltage on the descending branch of sine just crosses  $0\text{ V}$ . As the voltage crosses  $0\text{ V}$  and becomes negative the flux start to decrease, and the device can no longer be set. Both  $V_{set}$  and  $t_{set}$  are functions of critical flux, amplitude and frequency of the driving voltage.

### 2.3.3 Chua's Constitutive Memristor Relations for William's Device: Reset Model

In [2] the purely ionic the model for the set operation applied to the reset operation predicts that "*even a small negative bias will switch it back to the off state*", as mentioned above. The model presented above for set operation cannot be used for reset, since the driving force is the electric field in the undoped region, which does not exist when the device has been fully set. Therefore a reset model from the on-state to the off-state is required. In the following a rupture model is developed based on the assumption that the rupturing of the conductive region (CR) is a combined result of high electric fields and of Joules heating which raises the temperature at the interface between the doped conductive oxide region and the right metal electrode (see Figure 2.5 and 2.6).

When the temperature at the interface is high enough the doping ions can be easily dislodged by drift-diffusion. On the other hand, the interface between the conductive solid electrolyte and the grounded metal electrode will not detach because there is an ample supply of ions in the conductive region next to it and an electric field driving the ions toward the left interface. However, at the right interface, the dislodged ions will be driven into the bulk of the  $TiO_2$  film. Therefore the right interface will detach in stages and create undoped regions close to the interface. This detachment will not be uniform across the device because of statistical nature of

drift–diffusion transport, the non–uniformity of the film composition, and all kinds of defects such as asperities of the  $TiO_2/Pt$  interface which could lead to locally enhanced electric fields which, in turn, would lead to nonlocal heating effects.

From then on, the detachment will proceed in an accelerated fashion: In the portions where the doped region are detached a negative electric field in the undoped regions will be established and will drive the ions toward the left interface according to the drift–diffusion model described before. Because of the partial detachment, the current will crowd in the few spots that are still connected to the right electrode, as indicated by the arrows in Figure 2.6. The resulting current crowding, in turn, will increase the local heating in the still undetached portion of the interface leading even more to a higher temperature and higher diffusion and thus to an accelerated detachment. The source of heating is resistive Joules heating. From a qualitative study of the Fourier temperature equation with Joules heating as the source, it is clear that the highest temperature will be not at the interface but deeper in the bulk, as indicated in Figure 2.6 by the concentric circles. This is mainly due to the boundary condition for the heat transport equation with the right  $Pt$  electrode which acts as an efficient heat sink. When a critical temperature  $T_{crit}$  has been reached ions become highly mobile and detach the conductive region of electrolyte from the metal electrode. The thermal effect is then supported by the strong electric field which sets in as soon as the detachment is realized and sweeps the still highly mobile ions back toward the left electrode, creating, thus, a final gap  $\Delta$  in between the conductive region and the electrode (see Figure 2.7). Thus the rupturing model describes the transition from the ON–state characterized by  $W = D$  to an OFF–state characterized by  $W_{\Delta} = D - \Delta$ .

A comprehensive numerical physical electro–thermal model of resistive rupturing in resistance–change memory has been recently presented [83]. Although the physics of the rupturing is more or less well understood, the challenge in this context is to describe this effect in terms of electrical flux  $\varphi$  as required by Chua’s constitutive memristor relation. The diffusivity  $D$  and mobility  $\mu$  of the ions depend on the temperature by the Arrhenius relation, i.e.  $\{D, \mu\} \simeq \exp(-E_a/kT)$ , where  $E_a$  is the activation energy and  $T$  is the absolute local temperature. The range of  $T$  is  $T_0 \leq T \leq T_{crit}$ , for small current temperature  $T$  will be close to the ambient temperature  $T_0$ , at high currents – as in the reset operations –  $T$  will approach  $T_{crit}$ . We postulate that the gap  $\Delta$  is created when the local temperature has reached a value

$T_{crit}$ , which according to several studies [83–85] is in the range of 650–800K. The dependence on Joule's heat and  $T_{crit}$  is given by:

$$kT_{crit} = kT_0 + \frac{Q_J}{mc_p} \quad (2.58)$$

where  $Q_J$  is the Joule's heat,  $m$  is the volumetric mass of the doped region and  $c_p$  is the specific heat capacity of the doped region. Joules heating is given by

$$Q_J = \int_0^{t_{reset}} \frac{v^2(t')}{R_{on}} dt'. \quad (2.59)$$

where, in case of a linear ramp,  $t_{reset}$  is determined by the experimentally measured  $V_{reset}$  value and the applied ramp rate  $r$ , i.e.  $t_{reset} = V_{reset}/r$ .

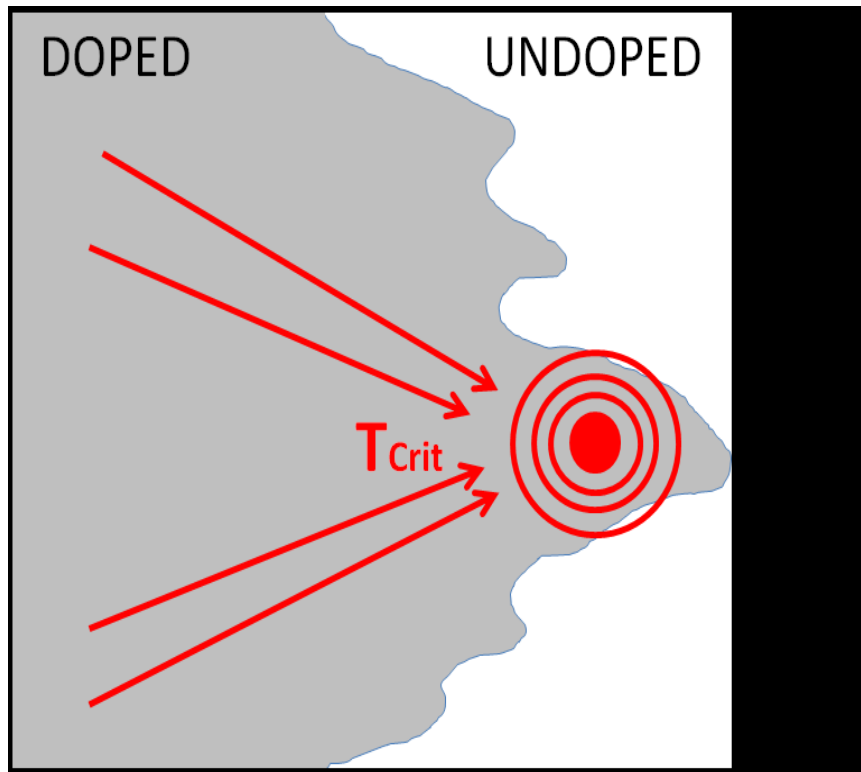


Fig. 2.6 The last stage of the detachment of the doped (conductive) electrolyte region from the metal electrode. The connection takes place only at a single asperity. The entire current, indicated by dashed arrows, crowds through the single asperity leading to a hot spot (concentric circles) characterized by  $T_{crit}$  in the center.

Although, there is no universal relation between Joule's heat and electric flux, for the purpose of this model  $Q_J$  and  $T_{crit}$  are modeled as follows:

$$kT_{crit} = kT_0 + \frac{Q_J}{mc_p} = kT_0 + c\varphi_{crit}^n \quad (2.60)$$

with exponent  $n > 3/2$  in order to match the first order expression of energy in powers of time and the constant  $c$  is a device constant specific to the memristor construction, i.e. the choice of the solid electrolyte material, the choice of the electrode material, and the nature of the interface between those materials. Constant  $c$  has to be fitted to experimental data of the device. Finally,

$$\varphi_{crit} = \sqrt[n]{\frac{k(T_{crit} - T_0)}{c}} \approx \sqrt[n]{\frac{kT_{crit}}{c}}. \quad (2.61)$$

If  $T_{crit} \gg T_0$ , the ambient temperature can be neglected when calculating  $\varphi_{crit}$ .

With the last equation the expression for  $G^{-1}(\varphi)$  can be written as:

$$G^{-1}(\varphi) = R_{on}[1 - \exp(-A(\varphi))] + R_{\Delta} \exp(-A(\varphi)) \quad (2.62)$$

$$A(\varphi) = \frac{E_a}{k} \left( \frac{1}{T_0 + c\varphi} - \frac{1}{\varphi_{crit}} \right) \quad (2.63)$$

$$R_{\Delta} = R_{on} \left( \frac{\Delta}{D} \right) + R_{off} \left( 1 - \frac{\Delta}{D} \right) \quad (2.64)$$

for  $\varphi \leq \varphi_{crit}$ .

For the conductance  $G(\varphi)$  we obtain therefore:

$$G(\varphi) = \frac{dq(\varphi)}{d\varphi} = G_{on}[1 - \exp(-A(\varphi))] + G_{\Delta} \exp(-A(\varphi)) \quad (2.65)$$

The equation (2.65) can be modified slightly without losing its functionality:

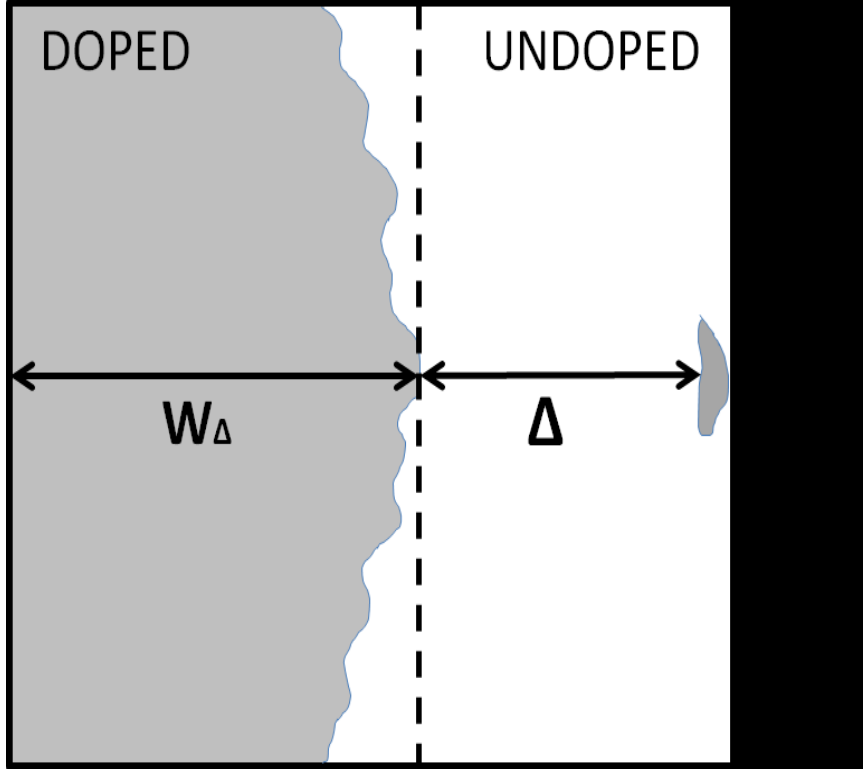


Fig. 2.7 Doped conductive region is completely detached from the metal electrode by the minimal gap  $\Delta$ . The resulting effective boundary  $W_{\Delta}$  separating the conductive electrolyte region from the non-conductive region is shown by the dashed line.

$$\begin{aligned} \frac{dq}{d\varphi} = & G_{on}[1 - \exp(-A(\varphi))] + G_{\Delta} \exp(-A(\varphi)) + \\ & - (G_{on} - G_{\Delta}) \frac{E_a \exp(-A(\varphi)) c n \varphi^{n-1} (\varphi_{crit} - \varphi)}{k(T_0 + c\varphi^n)^2} \end{aligned} \quad (2.66)$$

The last term in equation (2.66) has been constructed in such a way as to match very closely the functionality of  $dq/d\varphi$  for the entire range of applied fluxes  $\varphi$  and still allow analytical integration resulting in constitutive relation  $q = q(\varphi)$ , given by the analytical expression in equation (2.67):

$$q(\varphi) = \frac{\varphi}{R_{on}} + \frac{R_{\Delta} - R_{on}}{R_{\Delta} R_{on}} (\varphi_{crit} - \varphi) \exp(-A(\varphi)) \quad (2.67)$$

where  $\exp(-A(\varphi)) = 1$  for all  $\varphi \geq \varphi_{crit}$ . Note that relation (2.67) is valid for any positive exponent  $n$ .

This model describes the rupturing in the reset operation from fully conductive state characterized by  $W = D$  and  $R = R_{on}$  to a ruptured state characterized by  $W_{\Delta} = D - \Delta$  and  $R = R_{\Delta} \approx R_{off}$ . For continued resetting operation at negative fluxes, i.e. for driving  $W_{\Delta} = D - \Delta$  to a smaller  $W$  values, the drift-diffusion model derived in the paragraph 2.3.2 is to be used for negative flux with the initial boundary  $W_0 = W_{\Delta} = D - \Delta$ . At this point it is useful to discuss in more detail the role of the boundary  $W_{\Delta}$  in conjunction with the drift-diffusion and thermal reset models. When the thermal reset model is applied to the device in an on-state, the boundary  $W$  is specified by  $W = D$ . As discussed before, the thermal model causes the boundary  $W$  to move abruptly from  $W = D$  to  $W_{\Delta} = D - \Delta$ , where  $\Delta$  is the gap created in the filament (see Figure 2.7) when the critical temperature  $T_{crit}$  has been reached. At this point the thermal reset model has run its course. If a negative voltage is still applied to the device, the boundary  $W_{\Delta}$  will be driven back by the drift-diffusion model. Thus  $W_{\Delta}$  becomes the initial condition of the boundary  $W_0$  for drift-diffusion model, i.e.  $W_0 = W_{\Delta}$ .

As in the previous case, the reset voltage  $V_{reset}$  will be a function of a specific voltage input. However, the situation is slightly more complex than for the set model, because of the nature of the thermal effects that trigger the rupturing event. If we consider linear voltage ramp as a first example of a typical voltage input waveform, it is clear that if the ramp rate is high, of the order of 1 [V/s], the device will have little time to dissipate the heat accumulated at the conductive electrolyte-metal interface. The other extreme would be a very low ramp rate of 1 [mV/s] or lower, in this case the time over which the heat accumulates will be limited by the time dissipation constant  $\tau$  of the device. The issue of heat dissipation is still controversial with some researchers asserting that a typical dissipation time is in the nanosecond range. This dependence has been recently observed in *Cu/TaOx/Pt* resistive switching devices [81]. For fast ramps, we assume that the lower time boundary should be zero and results in the following expression:

$$\varphi_{crit} = \int_0^{\frac{V_{reset}}{r}} r t dt = \frac{1}{2} r \left( \frac{V_{reset}}{r} \right)^2. \quad (2.68)$$

It follows that

$$V_{reset} = \sqrt{2r\phi_{crit}} \propto \sqrt{r} \quad (2.69)$$

For fast ramp rates, the model predicts that the reset voltage  $V_{reset}$  increases with square root of the ramp rate.

In the extreme case of very low ramp rate one obtains:

$$\phi_{crit} = \int_{\frac{V_{reset}}{r} - \tau}^{\frac{V_{reset}}{r}} r t dt = \tau V_{reset} - \frac{1}{2} r \tau^2. \quad (2.70)$$

It follows that

$$V_{reset} = \frac{\phi_{crit}}{\tau} + \frac{1}{2} r \tau \propto r \quad (2.71)$$

can be seen that in this case the reset voltage  $V_{reset}$  increases linearly with the ramp rate  $r$ .

The overall dependence of  $V_{reset}$  on  $r$  can be given by the following function that contains the two limiting cases discussed above:

$$V_{reset} = V_{reset,min} + \frac{r}{\frac{2}{\tau} + \sqrt{\frac{r}{2\phi_{crit}}}} \quad (2.72)$$

where  $V_{reset,min} \neq 0$  is – as experimentally observed [82–85, 81] – the minimum  $V_{reset}$  voltage below which the device cannot be reset under any input voltage waveform, and, specifically, in case of linear voltage ramp, that cannot be reset at any voltage ramp rate. In other words,  $V_{reset,min}$  is a device constant. For sinusoidal signal a similar expression to equation (2.57) derived for  $V_{set}$ , can be derived in this context for  $V_{reset}$  as a function of frequency  $\omega$  and amplitude  $V_0$ .

### 2.3.4 Rupturing Model Simulation Results

The reset model (2.67) (i.e. rupturing of the filament due to thermal effect described in paragraph 2.3.3) can be used to compare the results of the simulation with the behavior of memristor devices available in literature. The scope of these numerical

simulations is to show the relation between the reset voltage  $V_{reset}$  with the critical flux  $\varphi_{crit}$ .

The device considered in the simulation is characterized by following ON and OFF memristances:  $R_{on} = 10\Omega$  and  $R_{off} = 100\Omega$ , which represent the two resistance characteristics of the device when the doped (i.e. conductive) region is at  $W = D$  and  $W = 0$ , respectively. The thermal effects are expected to be seen when the doped region is attached to the powered electrode and the conductive region asperities are being formed. For simplicity it is assumed that initial conditions  $W_0 = D/2$ . At this initial condition the ionic movement in the filament is not effected by Joules heating and the ion transport is characterized by drift–diffusion in the applied electric field described by the equations (2.52), (2.53) and (2.54).

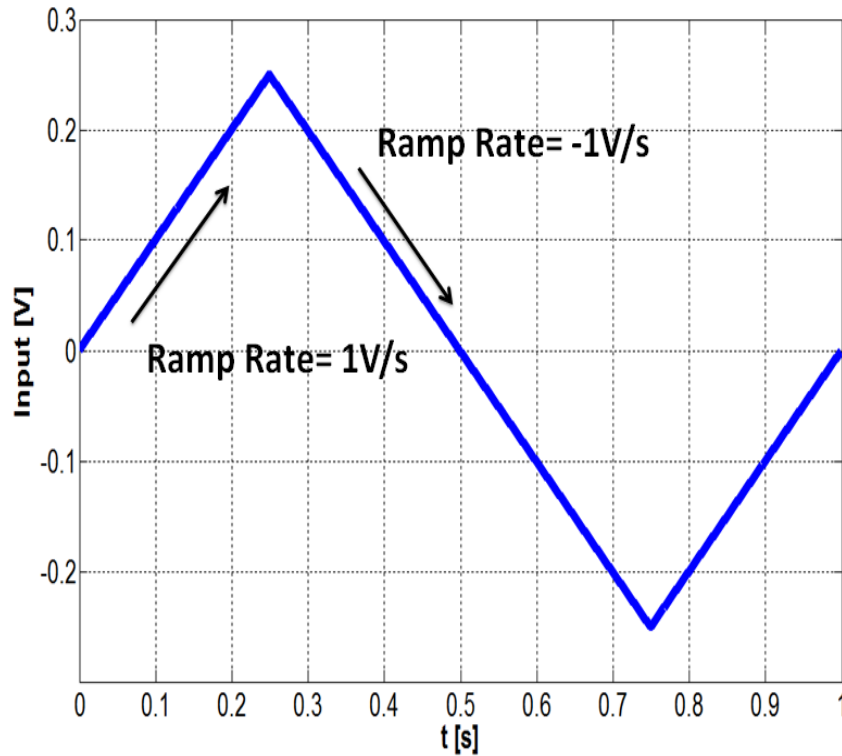


Fig. 2.8 Input voltage  $v(t)$  wave form used in numerical simulations of the memristor device modeled by (2.67). A seesaw wave form is chosen in order to have a constantly increasing and decreasing voltage during the essays.

The seesaw wave form shown in Figure 2.8 is commonly used in experiments and numerical simulations for electrical characterization of memristor devices. The amplitude and the frequency of the input voltage  $v(t)$  are set in order to reach

respectively  $\varphi_{max}$  and  $\varphi_{min}$ , that is required to achieve the formation and subsequently the rupturing of the filament. It turns out that the memristor device is flux controlled and so it is important to be aware at which time the voltage becomes negative in order to better understand the impact of the flux on the device.

A first simulation is performed comparing two different memristor models: the first model (named model A) is purely flux controlled and its internal dynamics are only determined by the ionic drift due to the electric field changes in the device; the second model (named model B) is the thermal detachment model. This allows to evaluate the differences of the  $i-v$  curves due to the thermal effects. For the model B a set of internal parameters have been preset as follows:  $T_{crit} = 100^\circ C$  (373.15 K) and the ambient temperature was set to  $T_0 = 25^\circ C$  (298.15K).  $T_0$  is considered in the computation of the critical flux since in this case  $T_{crit}$  was not set to a high enough value such that the ambient temperature could be considered negligible. The exponent  $n$  in equation (2.60) is chosen to be  $n = 2$ . For  $n = 2$  there are two possible solutions of  $A(\varphi) = 0$  (see Figure 2.9). The negative flux  $\varphi$  describes the physics underlying the rupturing of the filament, because it occurs only by applying a negative potential for a reasonably long time. It should be noted, in this context that Joules heat is independent of the polarity of the voltage or current. The red dashed line shows when  $A(\varphi)$  becomes negative due to a negative flux  $\varphi_{crit}$ .

The comparison between model A and model B has been performed by means of:

- similarity of the two  $i-v$  curves resulting from the  $v(t)$  given in Figure 2.8
- changes in the respective conductive region and in the memristance.

The  $i-v$  curves of model A and B are shown in Figure 7, respectively. The effect of  $A(\varphi)$  leads the memristance change when  $W = D$  and the applied voltage is negative. The transition between  $R_{on}$  and  $R_{\Delta}$  is not abrupt but gradual caused by the ionic movement of the filament at some positions along the boundary between conductive and not conductive regions ions move at first before in other locations and cause local detachment from the electrode. This leads to an instant memristance change followed by a slight gradual change until reached  $\varphi_{crit}$  and therefore  $R_{\Delta}$  and the rupture of the filament.

When the thermal model is implemented (see Figure 2.10B) the memristance change is gradual after an instantaneous abrupt change. Also the total amount of

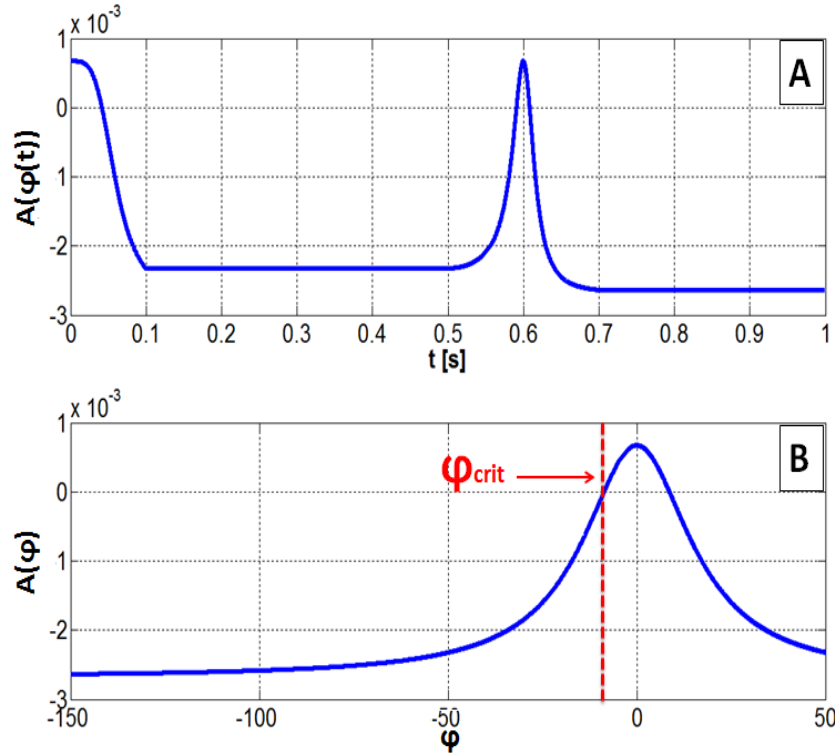


Fig. 2.9 (a) Graph showing  $A(\varphi(t))$ . From Figure 2.8 it is possible to see that the voltage crosses 0 V and becomes negative at  $t = 0.5s$ . From that instant  $A(\varphi)$  increases crossing 0 and becoming positive, since still in presence of a positive flux.  $A(\varphi)$  decreases afterwards reaching 0 again when  $\varphi_{crit}$  is reached. (b) The graph shows the dependency of  $A$  from  $\varphi$ . As afore mentioned there are two fluxes at which  $A(\varphi)$  is null.

current flowing through the device is higher in the second model due to a later change in the conditions of the system. The first instantaneous abrupt change is given by the energy accumulated in the ions forming the filament. Some of the ions move before the rupturing changing the memristance. The rest remain attached through the conductive  $TiO_2$  region until the critical flux is reached. The dynamical changes of the memristances and of the doped region are compared (Figure 2.11 and Figure 2.12).

In both cases the set dynamics (the set of the device to  $R_{on}$ ) are the same but the reset dynamics differ even when the same input voltage is applied. In the model B the boundary remains attached i.e.  $W = D$  for a longer period of time since most of the ions forming the filament have not experienced high enough temperature required for the rupturing. The filament is still intact until the critical temperature ( $T_{crit}$ ) is reached. This happens as long as the flux is smaller than the critical flux  $\varphi_{crit}$ .

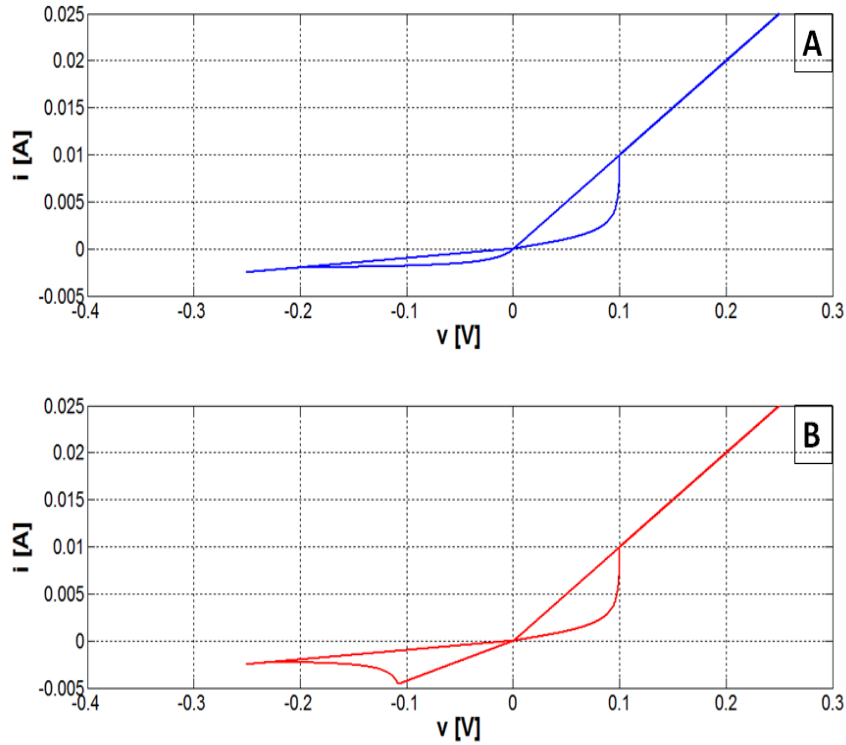


Fig. 2.10 (a)  $i-v$  curve for the general memristor without the implementation of the thermal detachment model. (b)  $i-v$  curve for the memristor with the implementation of the thermal detachment model (with the values described above).

Once  $\varphi = \varphi_{crit}$  then there is a sudden transition of the boundary  $W$  from  $W = D$  to  $W = D - \Delta$ . Accordingly the memristance changes from  $R_{on}$  to  $R_{\Delta}$  as described in equation (2.62). This change is also observed in the  $v-i$  characteristics of the memristor with model B. The model A presents a change of the boundary  $W$  at time instant  $t = 0.5s$ , the instant in which the input voltage crossed  $0V$  and became negative. In such a case the filament detachment results to be abrupt as soon as the flux begins to decrease. For the same simulation conditions also the memristance changes in time have been plotted and evaluated.

The memristance of the model A changes only according to flux. At the time instant  $t = 0.5s$  (when the flux begins to decrease) there is a sudden memristance decrease. The memristance of the other device decreases also abruptly at the same time instant, but to a given value which is given by the behavior described by  $R(A(\varphi))$ . The memristance of the model B has the same behavior until the critical flux is reached. From that instant on the memristance of the model B follows the drift-diffusion model with  $W_0 = W(t_{reset}) = D - \Delta$ .

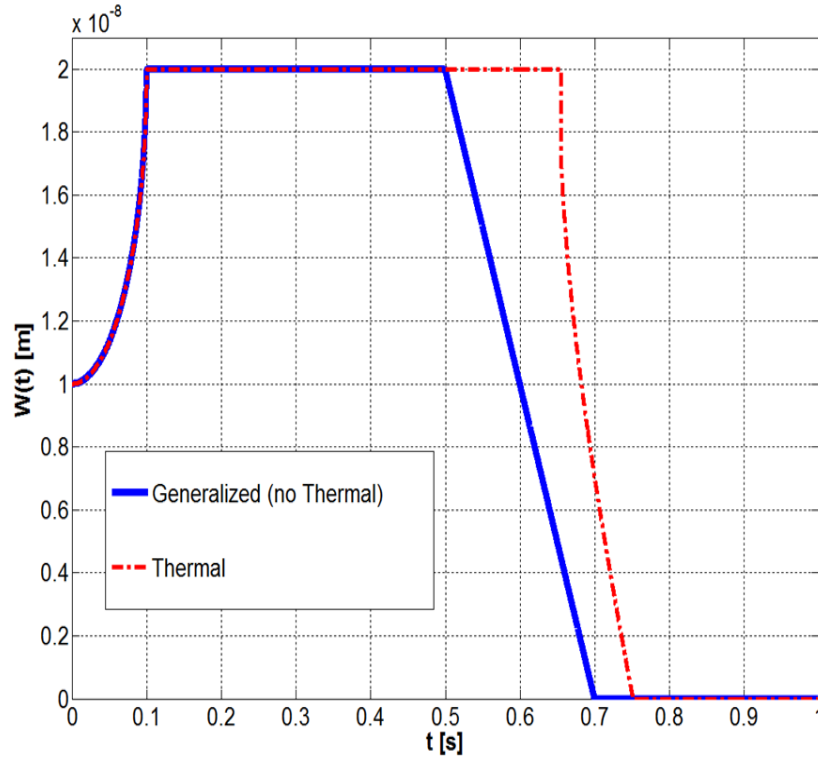


Fig. 2.11 Change of the doped region  $W(t)$  over time both for the general (no thermal model implemented) memristor and the device which resents from the thermal detachment effect.

A second set simulations has been performed for the model B only considering five different critical temperatures  $T_{crit}$ . The change of the critical temperature causes the critical fluxes of the device to change resulting in different rupture dynamics. Using the dependance of  $A(\varphi)$  on the flux it is possible to study the device's sensibility to ambient temperature  $T_0$ .

A higher  $T_{crit}$  requires larger Joules heat. Since the input voltages are the same for each device, the critical fluxes are reached at a later point in time by the devices with higher  $T_{crit}$ . Figures 2.13 and 2.14 illustrate the different behaviors of the devices. Considering the different  $v - i$  characteristics, the devices with higher critical temperatures permit a greater amount of current flowing through the device since the conductive on-state is maintained for a longer time for the same voltage waveform. The equation (2.61) implies that increasing the critical temperature increases also the critical flux.

Fixing the critical temperature to  $T_{crit} = 1000^\circ C$ , the activation energy is increased. This increased the ratio  $E_a/kT$ , where  $k$  is the Boltzmann constant, increas-

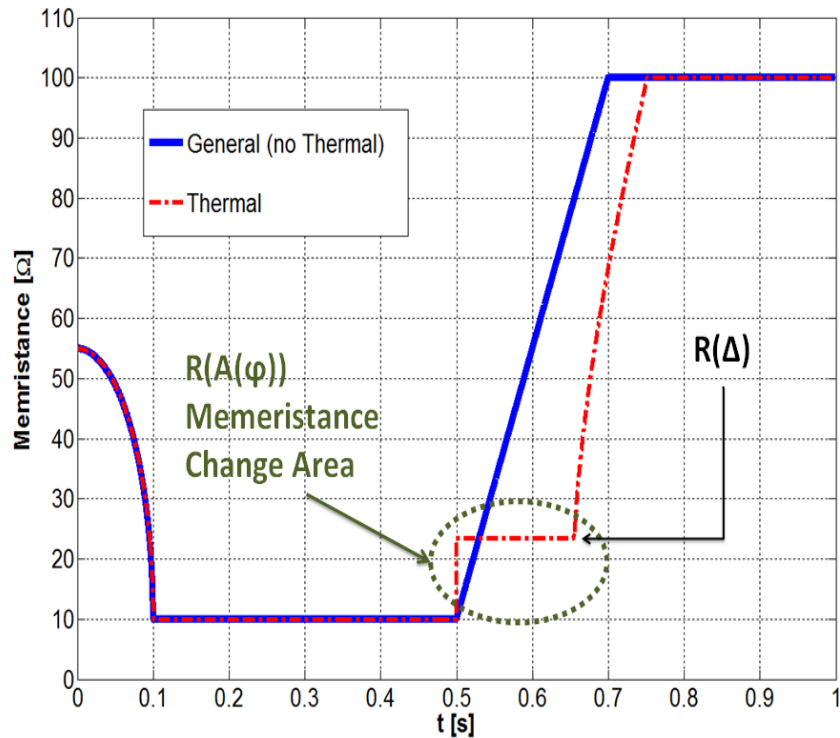


Fig. 2.12 Memristance change comparison for the general model and for the memristor element in which the thermal detachment model was implemented. The region in which there is the memristance change due to the thermal effects (conductive filament not yet ruptured) is put in to evidence by the green dashed square. In that region the memristance of the thermally controlled device follows  $R(A(\varphi))$  described behavior.

ing accordingly  $A(\varphi)$ . The increase of the activation energy of the thermal rupturing or detachment model changes the shape of the  $i-v$  curve of the device for negative voltages as shown in Fig. 2.14 and Fig. 2.15.

### 2.3.5 Discussion and Conclusions

The importance of the model is that it is formulated exclusively in terms of circuit variables total charge and electrical flux. The resulting  $v-i$  characteristics are only specific manifestations of the model that strongly depend on the specific input wave form. As emphasized by Chua [5], memristor models for  $v-i$  characteristic cannot be used to predict the current response to any other voltage excitation wave forms different from the wave form used for a particular  $v-i$  characteristic that has been used for the model. In paragraph 2.3.4 it has been verified that changing parameters

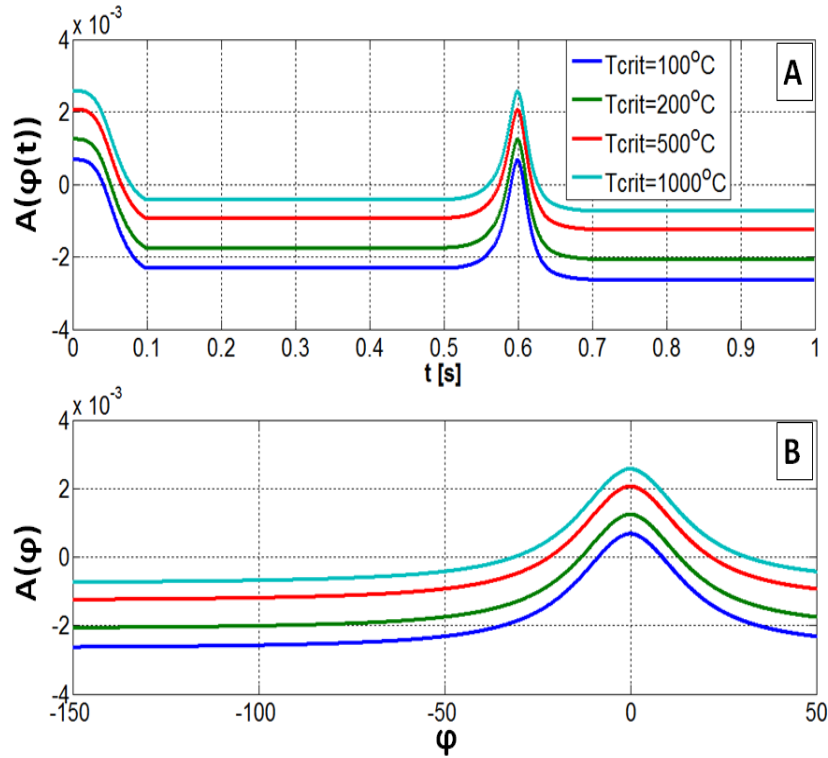


Fig. 2.13 (a) Representation of  $A(\varphi(t))$  at different  $T_{crit}$ . (b) Representation of  $A(\varphi)$  for different  $T_{crit}$ . At different  $T_{crit}$  critical fluxes change accordingly. Since higher critical temperature needs a higher flux to be reached, the devices with higher  $T_{crit}$  will reach rupturing rater than the others.

such as ramp rate  $r$ , voltage amplitude  $V_0$ , or  $\omega$ , or changing the wave forms of  $v(t)$  may result in completely different responses. This is particularly important for a simulation of a circuit of memristors. While a pinched  $v - i$  hysteresis loop measured from any experimental two-terminal device implies that the device is a memristor, the pinched loop itself is useless as a model since it cannot be used to predict the voltage response to arbitrarily applied current signals, and vice-versa. In the case of a memristor circuit, one cannot work with models describing  $v - i$  characteristic but with charge and flux models as postulated by Chua to account for the shared memory evolution between the memristors involved. The preceding derivation shows that all internal state variables, such as the barrier  $W(t)$  between the doped and undoped region or the temperature responsible for the rupturing effect have been expressed in terms of the flux variable. No memristor unfolding parameters, i.e. a vector of state variables associated with the device and its physical operating mechanisms, are required. Of course, with more additional variables the

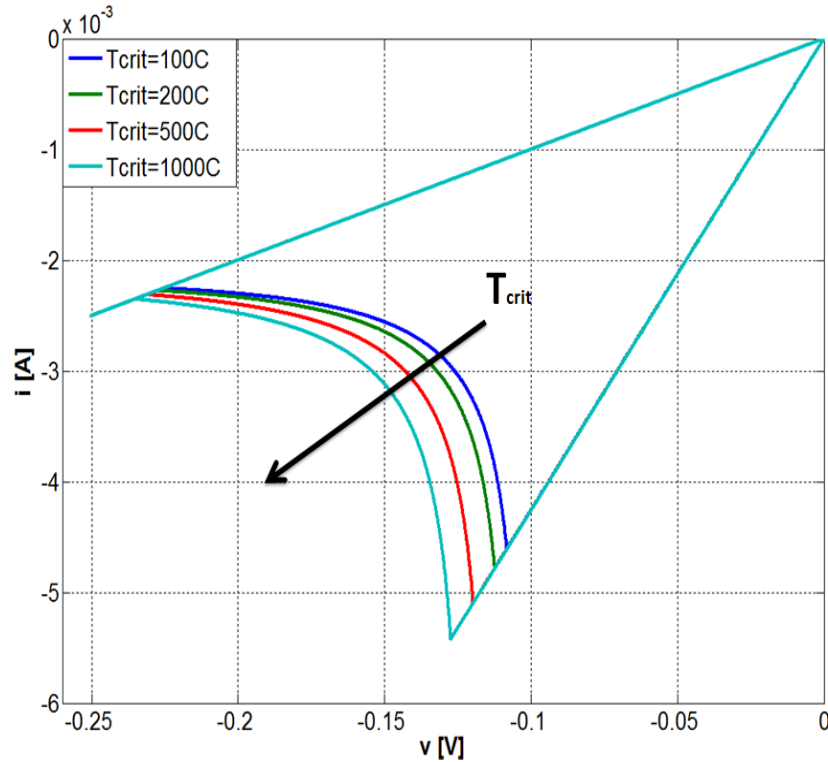


Fig. 2.14  $i-v$  curves of the five devices with different  $T_{crit}$ . Higher  $T_{crit}$  maintain the conductive region of the filament attached to the electrode longer, since more energy is required for the rupture.

modeling task is easier to accomplish, as the resulting nonlinear scalar function can be used to fine-tune the corresponding pinched hysteresis loop into almost any shape which best approximates the experimental data.

Here a charge-flux memristor model has been proposed to characterize crucial physical mechanism at the metal-oxide interfaces during switching behavior of a resistive memristor. Recognizing that  $i-v$  pinched hysteresis curves are just specific manifestations of the memristor device under a particular excitation, the proposed model is described exclusively in terms of total charge and voltage flux as postulated by Chua [5]. In particular, it is shown that all internal state variables (e.g. the position  $W(t)$  of the interface between  $TiO_2$  and  $TiO_{2-x}$  and the temperature responsible for the detachment of the doped conductive region from the metal electrode can be described in terms of the flux variable only. The model then automatically describes the dependence of  $V_{set}$  and  $V_{reset}$  voltages as a function of the particular input voltage wave form that has been applied to the device. In principle,

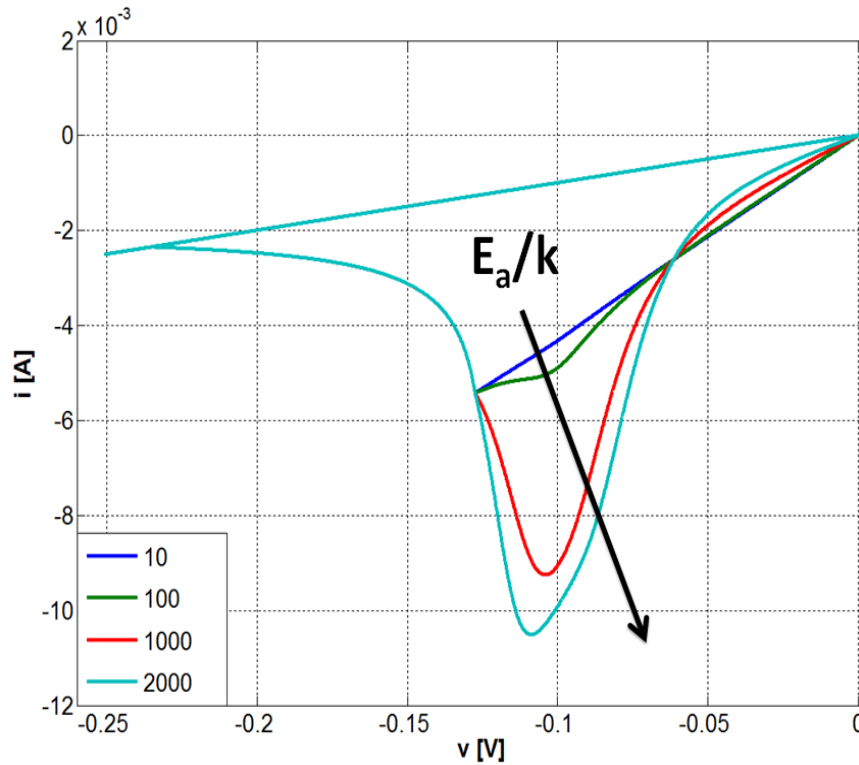


Fig. 2.15  $i-v$  curves at increasing  $E_a/k$  ratio. The critical temperature for the device was fixed to  $1000^\circ\text{C}$ .

this includes the entire history of the voltage stress on the device. This history, can be characterized by a boundary condition for the boundary  $W_0$  between the conductive and non-conductive regions of titanium oxide. This boundary condition has to be known in order to predict the result of the a new voltage stress of the device. Numerical simulations have been presented to illustrate the influence of thermal effects on the device performance and the reset process. The proposed memristor model is useful for the design of a resistive switching cell as well for the simulation of nonlinear memristive circuits where the interactions between the connected memristors cannot be predicted *a priori*.

## 2.4 $\varphi - q$ Modeling of Phase Change Memories

PCMs are one of the most promising non-volatile memory technologies and is finding applications in areas such as storage-class memory and emerging non-von

Neumann computing systems. Even though powerful physics-based models have been developed for these devices, there is a lack of simple and accurate circuit models to describe these elements. Here it will be exploited *memristor theory* to obtain a simple and reliable circuit model based on electrical variables such as *charge* and *flux*. The model here proposed is based on experimental measurements of PCM devices fabricated in the 90nm technology node.

### 2.4.1 Introduction to PCMs and Physical Description

Phase change memory is arguably the most advanced among emerging non-volatile memory technologies [86]. PCM has emerged as a promising candidate to bridge the performance gap between the main memory and storage in computing systems typically referred to as storage-class memory [87, 88]. More recently PCM has also found application in non-von Neumann computational paradigms such as neuromorphic computing and memcomputing [89–91].

The phase change memory concept is based on the reversible phase change of materials such as  $\text{Ge}_2\text{Sb}_2\text{Te}_5$  (GST) from the ordered crystalline phase to the disordered amorphous phase. The resistance of PCM devices depends on the amorphous-crystalline phase configuration. The PCM device exhibits a rich dynamic behavior and is described by an interconnection of electrical, thermal and structural dynamics. There is significant on-going research on understanding this dynamics and physics-based models are being developed [92–94].

In parallel, significant developments were also being made in the theory of memristive devices. *Memristors* are two-terminal nonlinear circuit elements capable of changing and maintaining the resistive state depending on the "whole history" of the voltage applied to and/or the current flowing through the device [41, 2]. The integrals between  $-\infty$  and  $t$  of the voltage and of the current represent the voltage momentum and current momentum, respectively [26]. Since as described in section 2.2 and as shown in the case of the HP model (section 2.3), a pinched  $v$ - $i$  curve is found to be just the response to a specific input (i.e. a mathematical description of memristor  $v$ - $i$  curves is not a circuit model), a comprehensive classification of memristor devices in terms of flux-charge electrical variable is provided [26]. One such example of a flux-charge model of  $\text{TiO}_2$  memristor devices can be found in [42].

Given the behavioral similarity between PCMs and memristors, it will be of significant interest to develop a  $\varphi$ - $q$  memristor model for PCMs thus connecting the research activities in these two hither-to distinct fields. This will also have significant practical ramifications such as having a simple and reliable analytical circuit model that can be included in standard circuit-level simulation tools. It can also benefit the emerging applications of PCMs in non-von Neumann computing.

A schematic illustration of a mushroom-type PCM device used for the experimental study is shown in Figure 2.16(a). The device was fabricated in the 90nm technology node with a sub-lithographically defined bottom electrode. The phase change material is doped GST of approx. 100nm thickness. In an as-fabricated device, the phase-change material is typically in the crystalline phase. To create an amorphous region, a voltage pulse of sufficiently high amplitude is applied to the device. The resulting Joule heating melts a substantial portion of the phase-change material. If the voltage pulse is stopped abruptly, the molten material quenches into the amorphous phase due to glass transition. The effective thickness of the amorphous region is denoted by  $u_a$ . The amorphous phase blocks the bottom electrode and the device is in a high resistance state referred to as the RESET state.

A characteristic DC  $I$ - $V$  behavior of the PCM cell in the RESET state is shown in Figure 2.16(b). The electrical transport in amorphous phase change materials has a strong field dependence [95, 96]. However, for the sake of simplicity, we assume that at low and intermediate fields, the transport is fairly Ohmic. Hence the electrical resistance is given by

$$R(u_a(t)) = \frac{\rho}{\pi r_E^2} u_a(t) \quad (2.73)$$

where  $\rho = 0.1\Omega m$  is the low-field resistivity of melt-quenched amorphous GST and  $r_E = 20nm$  is the effective radius of the bottom electrode. However, beyond a certain bias voltage denoted by  $V_{th}$ , the amorphous phase change material goes into a low resistance state. This phenomenon is known as threshold switching, the physical origins of which is being actively researched to-date [97, 98]. In our devices, for a  $u_a \approx 50nm$ ,  $V_{th}$  is approximately equal to 1.25V. Note that this is a purely an electronic phenomenon and the phase change material is still in the amorphous phase. The resistance of the device drops to an ON-state resistance value of  $\approx 7.5k\Omega$  which is mostly independent of the thickness of the amorphous region.

To induce amorphous to crystalline phase transition, voltage pulses have to be applied to the PCM device such that the temperature reached within the cell is in

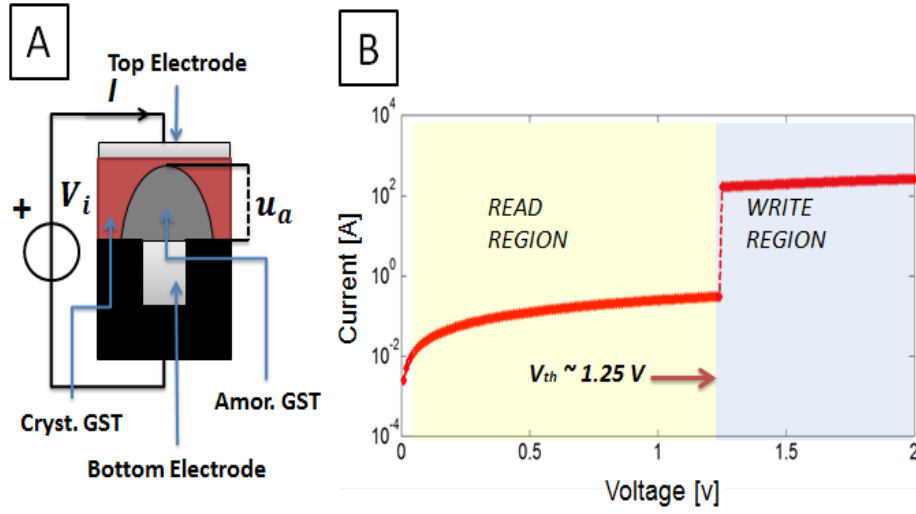


Fig. 2.16 (a) Schematic representation of a mushroom-type PCM device. In the RESET state, the phase change material in the amorphous phase blocks the bottom electrode and the device is in high resistance state. The effective thickness of the amorphous region is denoted by  $u_a$ .  $V_i$  denotes the voltage applied to the device and  $I$  denotes the resulting current flowing through the device. (b) A characteristic  $I-V$  behavior is shown. It can be seen that above the threshold switching voltage ( $V_{th}$ ), the device exhibits a much lower resistance even in the RESET state. The READ and WRITE regions of the  $I-V$  curve are shaded in yellow and blue respectively.

the regime where there is substantial crystal growth at the amorphous-crystalline interface. To pass sufficiently large current through the device and thus induce sufficient Joule heating, it is imperative that the voltage pulses should have an amplitude  $V_s \geq V_{th}$ . These type of pulses that induce phase transition are referred to as write pulses.

When such write pulses are applied, the evolution of  $u_a$  is given by

$$\frac{du_a(t)}{dt} = -v_g(t) \quad (2.74)$$

where  $v_g$  denotes the crystal growth velocity,  $[t_0, t]$  corresponds to the time interval in which  $v_i(t) = V_w \geq V_{th}$  is applied and  $u_a(t_0)$  is the initial amorphous thickness. The value of  $v_g$  depends on the temperature at the amorphous-crystalline interface

denoted by  $T$  given by

$$T(u_a(t)) = T_{amb} + R_{th}(u_a(t)) \frac{V_w^2}{R_{on}} \quad (2.75)$$

$T(t)$  depends on the ambient temperature,  $T_{amb}$  as well as the temperature rise due to Joule heating. The latter in turn depends on the electrical power that is dissipated and the effective thermal resistance,  $R_{th}$  which is function of the GST thickness  $u_a(t)$ .  $R_{th}(u_a)$  captures the thermal resistance of all possible heat pathways and naturally has a strong dependence on  $u_a$ . An estimate of  $R_{th}(u_a)$  obtained via experimental means is presented in Figure 2.17(a) [94]. It shows that the hottest region within the mushroom-type PCM device is close to the bottom electrode while the top electrode is substantially cooler. What is also shown is an approximate analytical description of  $R_{th}(u_a)$  given by

$$R_{th}(u_a(t)) \approx A_r \exp \left( -\frac{1}{2} \left( \frac{u_a(t) - \mu_r}{\sigma_r} \right)^2 \right) \quad (2.76)$$

where  $A_r = 2.2K/\mu W$ ,  $\mu_r = 10.62nm$  and  $\sigma_r = 32nm$ .

In Figure 2.17(b), an experimentally obtained estimate of the temperature dependence of crystal growth velocity is shown [94]. At low temperatures, crystal growth is insignificant while the maximum occurs at a temperature of approximately 750K. It is also not possible to crystallize beyond the melting temperature of  $T_M \approx 900K$ . An approximate analytical description of  $v_g(T)$  can be obtained given by,

$$v_g(T(u_a(t))) \approx A_g \exp \left( -\frac{1}{2} \left( \frac{T(u_a(t)) - \mu}{\sigma} \right)^2 \right). \quad (2.77)$$

where  $A_g = 0.548nm/ns$ ,  $\mu = 752K$ , and  $\sigma = 78K$ .

### 2.4.2 Memristor Model for PCM devices

In this section accurate memristor models are developed for PCM devices based on the physical description presented earlier. It was recently shown that memristor devices can be grouped into three classes: ideal memristors, generic memristors and extended memristors [26]. The ideal memristor is defined by a nonlinear relationship

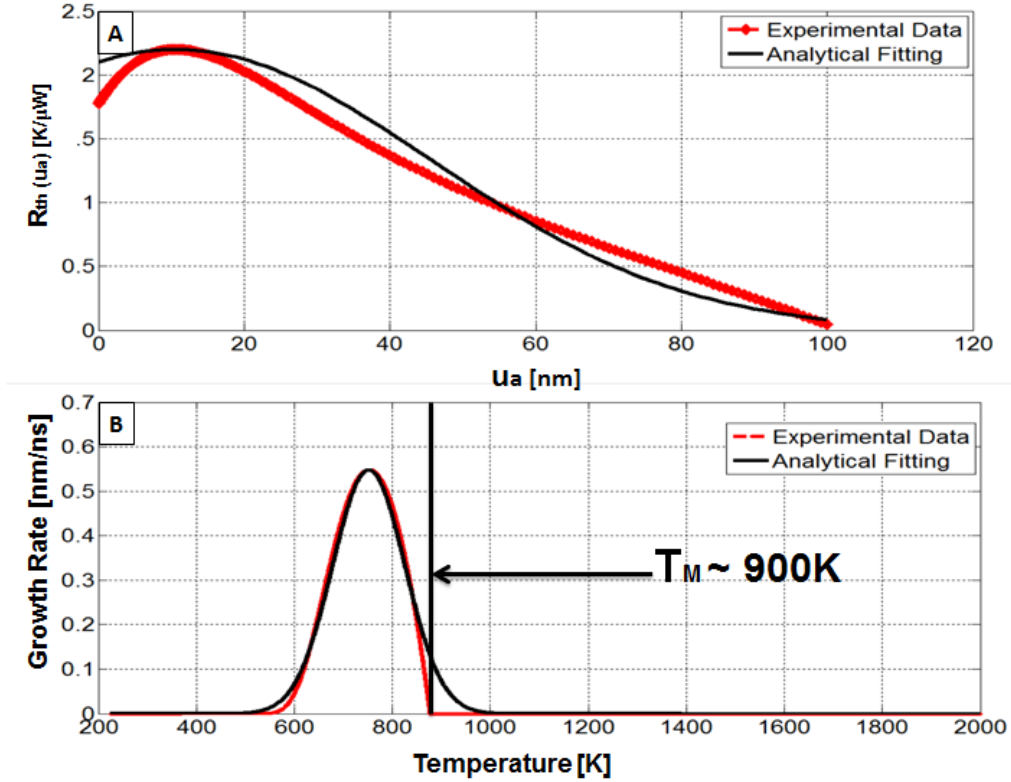


Fig. 2.17 Experimentally obtained estimate of (a) the effective thermal resistance as a function of the amorphous thickness and (b) the temperature dependence of crystal growth velocity.  $T_M$  is the melting temperature of the GST, and from that point on the growth velocity can be considered negligible. Also shown are analytical approximations.

$q = f(\varphi)$  corresponds to the original definition given by Prof. L. O. Chua [1]. Theorem 1 in [26] provides the necessary and sufficient condition to describe any memristor devices in term of both  $(\varphi, q)$  and  $(v, i)$ . In addition, Theorem 2 in [26] specifies the whole class of ideal memristors (also named *memristor siblings*).

Under the assumption that Theorem 1 holds, let us consider a (flux–controlled) general memristor described by (see [26] for further details):

$$q(t) = f(\varphi(t), u_a(t)) \Rightarrow i(t) = G(\varphi(t), u_a(t))v_i(t) \quad (2.78)$$

$$v_g(t) = g(v_i(t), u_a(t)) \Rightarrow v_g(t) = g(v_i(t), u_a(t)) \quad (2.79)$$

$$\dot{\varphi}(t) = v_i(t) \Rightarrow \dot{\varphi}(t) = v_i(t) \quad (2.80)$$

where the left-hand side represents the flux-charge description and the right hand-side is the description in terms of the voltage and current. The Ohm's law is recognizable where the memconductance  $G(\varphi(t), u_a(t))$  depends also on the internal memristor state variable  $u_a(t)$  (GST thickness).

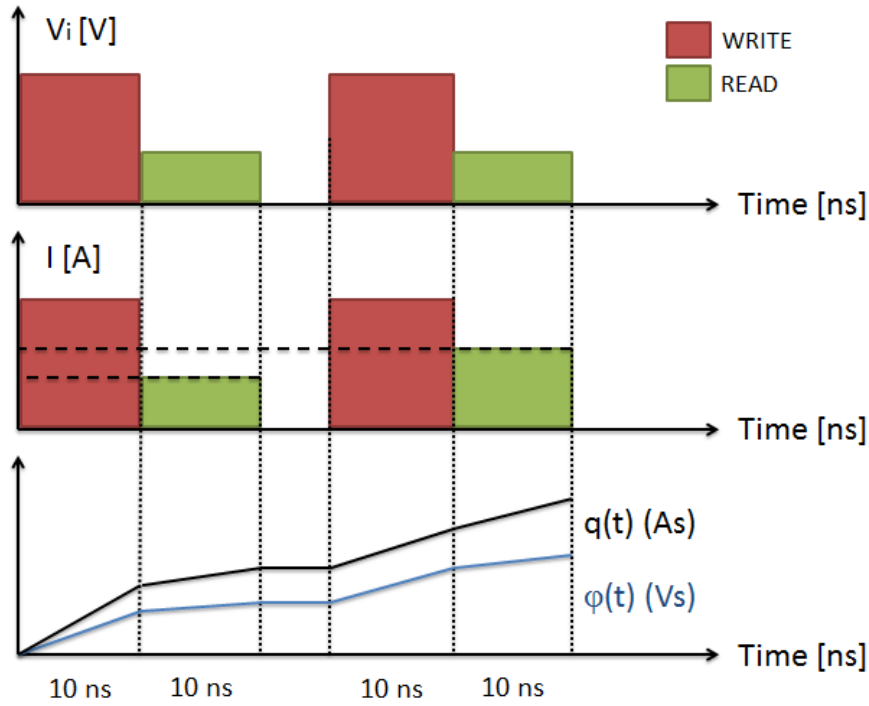


Fig. 2.18 Figurative example of an input voltage waveform, related to the output current and the respective flux  $\varphi(t)$  and charge  $q(t)$ . The case shown is an example of constant writing voltage ( $V_w$ ) inputs given to the PCM cell. From the graphs it is possible to note that  $\varphi(t)$  and  $q(t)$  are calculated as the sum of the areas of the input voltages and output currents respectively. From the last graph it is possible to see that the flux of the reading voltage ( $V_r$ ) can be considered negligible with respect to the flux of  $V_w$ . On the other hand the charge of the current the reading phase increases at every input step.

To investigate the mapping between the flux, charge and the interfacial temperature, Equations (2.74) and (2.75) were used to simulate the behavior of the PCM device when excited by appropriate voltage signals. These signals comprise of two consecutive square pulses. The first is the writing pulse  $V_w$  which is set to an amplitude ranging from 1.25V to 2V, with a 0.05V step, and a duration of 10ns. The second is a reading pulse  $V_r$  which has the scope to not modify the amorphous GST thickness, so is set to an amplitude of 0.05V which is lower than  $V_t$ . The duration of  $V_r$  is set to 10ns. The duration of the writing and reading impulses respectively were

chosen in order to consider the increase of the flux ( $\varphi$ ) given by  $V_r$  negligible with respect to the voltage momentum increase given by  $V_w$ . The ambient temperature is  $300K$ . The simulations were conducted to study the various scenarios such as (i)  $v_i(t)$  increasing ramp, i.e. constant increase of the  $V_w$  in ten steps; (ii)  $v_i(t)$  decreasing ramp, i.e. constant decrease of the  $V_w$  in ten steps; (iii)  $v_i(t)$  triangular waveform, i.e.  $V_w$  increases in five steps and decreases in five steps; (iv) with ten inputs of constant amplitude with  $V_w$  ranging from  $1.25V$  to  $2V$ , with a  $0.05V$  step. In Figure 2.18 is presented a figurative example of an input voltage waveform and the resulting output current respectively related to the momentums generated.  $\varphi(t)$  and  $q(t)$  can be calculated as the sum of the areas below the curves. From the same figure it is possible to note how the flux of  $V_r$  does not sensibly increase the overall momentum given by  $V_w$ . On the other hand, considering  $q(t)$ , as expected, the charge calculated from the output current read in the reading phase increases at each input step.

The resulting data from the previously described simulations is represented in the  $(\varphi, T, q)$ -phase space and interpolated in order to obtain the relationship among  $\varphi$ ,  $u_a(t)$  and  $q$ . Figure 2.19 and Figure 2.20 the interpolating surface and the interpolating lines respectively showing the relations amongst the three variables. Moreover in Figure 2.21 is presented the interpolating surface showing the relationship between the flux  $\varphi$ , the charge  $q$  and the interface temperature  $T$ . From the latter figure it is possible to derive the following relationship among  $\varphi$  and  $T$  taking into account  $T_M$  and the *initial temperature*  $T_0 = R_{th}(u_a(t_0))V_w^2/R_{on} + T_{amb}$  of the PCM,

$$\frac{T(\varphi) - T_0}{\xi} = \operatorname{erf}\left(\frac{k}{\xi}\varphi\right), \quad (2.81)$$

where  $\xi = (T_M - T_0)$  and the constant  $k = 2 \cdot 10^{-9} K/Vm$ . Expression (2.81) is a direct consequence of the integration of the Gaussian functions used to approximate  $R_{th}(u_a(t))$  and  $v_g(t)$  (i.e. equations (2.76) and (2.77)). Through the same equation it is possible to formulate the relationship between  $u_a(t)$  and  $\varphi$  in terms of temperature as

$$\frac{u_a(\varphi) - u_{a0}}{\lambda} = -\operatorname{erf}\left(\frac{T(\varphi)}{T_M} - 1\right), \quad (2.82)$$

where  $\lambda = v_g(T_0)k_1$  and  $k_1 = 1nm$ . The value  $v_g(T_0)$  is the crystal growth velocity, and  $u_{a0}$  is the GST thickness at the time point  $t_0$  and the first can be calculated from equation (2.77). It turns out that (2.82) corresponds to the solution of equation (2.79) describing the dynamics of the internal memristor variable and takes into account the

GST thickness  $u_a(t)$ . Furthermore the expression (2.82) takes also into account from equation (2.81) the diffusion phenomena between two bodies of different temperature ( $T_0$  and  $T_M$ ). Moreover from the same equation it is possible to note that the interface temperature  $T_0$  is to be considered as *hidden variable* according to [26].

From what above described, the relationship between  $\varphi$  and  $q$  results to be:

$$q(\varphi) = Q_0 \varphi \exp(T(\varphi)\alpha). \quad (2.83)$$

where  $Q_0 = k\beta \exp(-T_0\alpha)$ ,  $\beta = 1 \cdot 10^{-13} \text{VsAs/K}$  and  $\alpha = 1 \cdot 10^{-3.5} \text{K}^{-1}$ . As a proof that equations (2.82) and (2.83) are suitable to describe the behavior of the PCM cell, a fitting test has been performed between the data obtained from the simulation and the analytical results. The test has returned a reliability factor  $R^2 = 0.944$ , which denotes an accurate matching between the simulated behavior and the memristor model (2.82)–(2.83). Equation (2.83) is valid for  $\varphi \geq 0$  since from equation (2.75) the interface temperature depends on  $V_w^2$ . From this consideration the PCM cell can be considered as an unipolar element. Moreover it is worth noting that the PCM memristor model presented in equation (2.83) is valid for  $T(\varphi(t)) \in [T_0, T_M]$  and as a consequence for GST thicknesses  $u_a(T(\varphi)) \in [0, 100\text{nm}]$  and permits to express the charge as function of only the flux, that is the PCM turns out to be an ideal memristor (sibling) as described at the beginning of this paragraph (2.4.2).

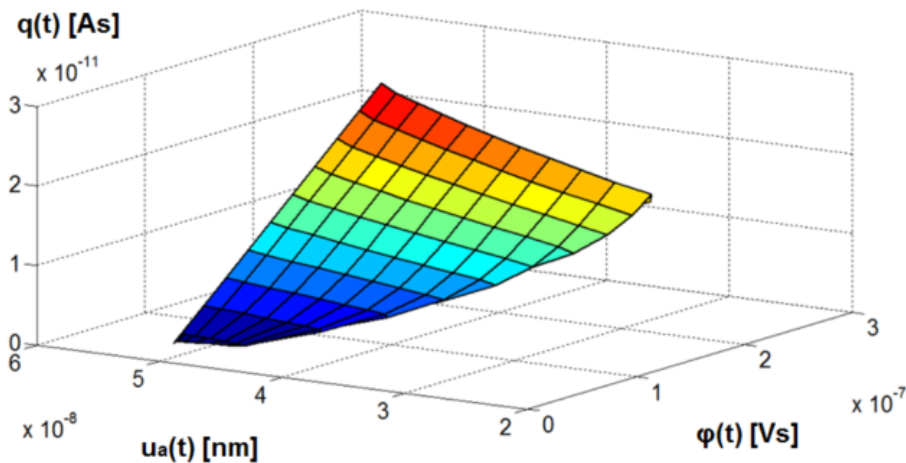


Fig. 2.19 Surface interpolating the experimental data in the  $(\varphi, q, u_a)$ -domain. The solid black lines highlight the curves that show the actual relationship built through the interpolation of the data obtained from all the simulations.

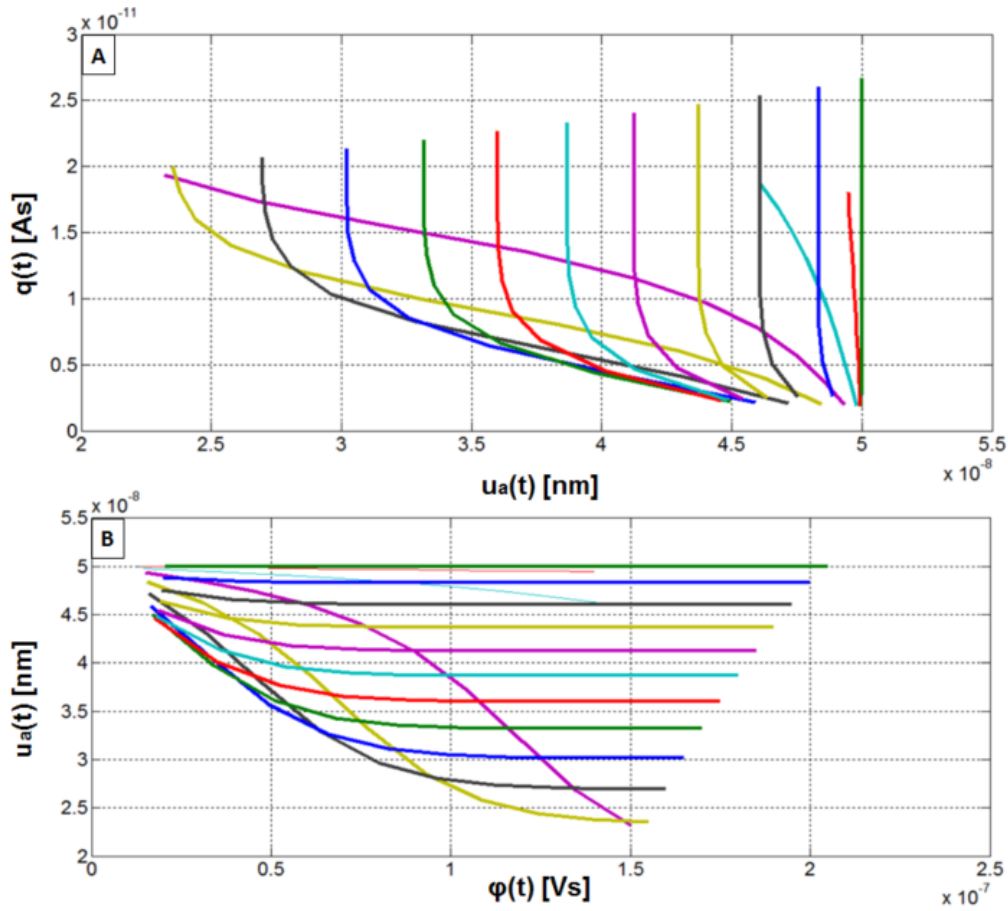


Fig. 2.20 Interpolating lines derived from the  $(\phi, q, u_a)$  surface in Figure 2.19. (a) Interpolating lines that show the family of curves describing  $q(u_a(t))$  and (b)  $\phi(u_a(t))$  obtained from the simulations.

### 2.4.3 Derived Conclusions on PCMs as Memristors

PCM technology is a leading non-volatile memory technology that could play a key role in future memory and computing systems. There is a significant understanding of the dynamics of PCM devices which is governed by an interconnection of electrical, thermal and structural dynamics. Even though the PCM devices exhibit significant behavioral similarity with other memristive devices, there have been no attempts at developing a flux-charge based memristor model for PCM devices. In this section, such a  $\phi$ - $q$  model is derived based on experimentally obtained estimates of the temperature dependence of crystal growth and the thickness dependence of temperature distribution within a mushroom-type PCM device.

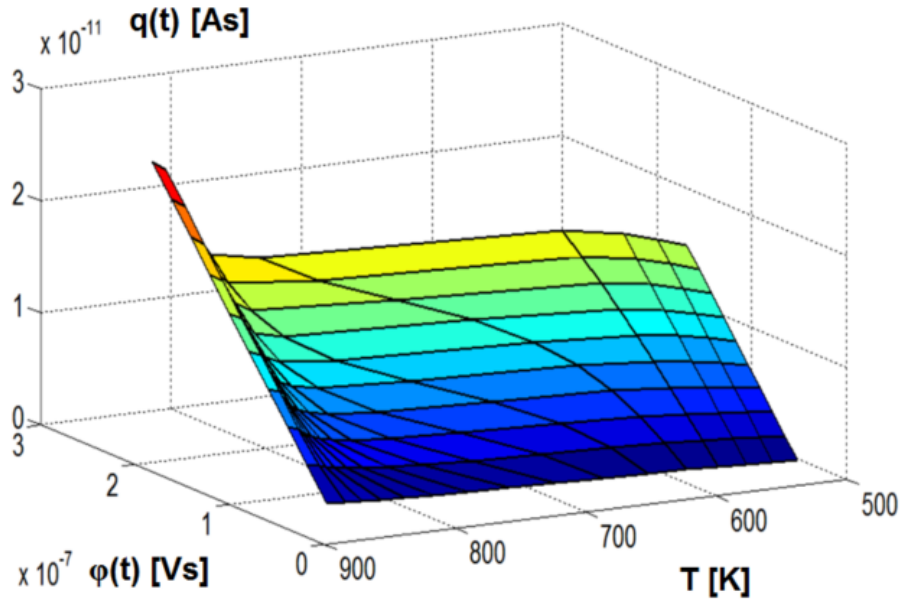


Fig. 2.21 Surface interpolating the experimental data in the  $(\varphi, q, T)$ -domain.

## 2.5 Memristive-RC Switching Dynamics of *Si* Nano-Wire Biosensors

Sandro Carrara *et al.* studied and developed in the recent years a new kind of biosensor that shows memristive dynamics under certain determined conditions [15]. The biosensor discussed is a *Si* nano-wire (SiNW) clamped between two *SiNi* junctions, obtained from a three step fabrication method. At first a photoresist line defines the wire position on the wafer, then a deep reactive ion etching is performed to obtain a scalloped trench. Finally, the trench is reduced to a suspended nano-wire after wet oxidation. Figure 2.22 shows a SEM image of the SiNW biosensor.

The SiNW biosensor is functionalized with several bio-molecules such as rabbit antibodies in order to sense the relative antigens. The bio-molecules with which the SiNW is functionalized are covalently bonded to the *Si* bulk. The device demonstrates its sensing capabilities when excited with an electric potential between the *SiNi* junctions presenting two different electric behaviours. Afore the functionalization, the device acts as non-linear resistor, with very similar dynamics to a memristor. When functionalized the dynamics change with a behaviour very similar to a resistor-capacitor series (RC unit). Plotting the device's dynamics on a  $v - \ln(i)$  plot before

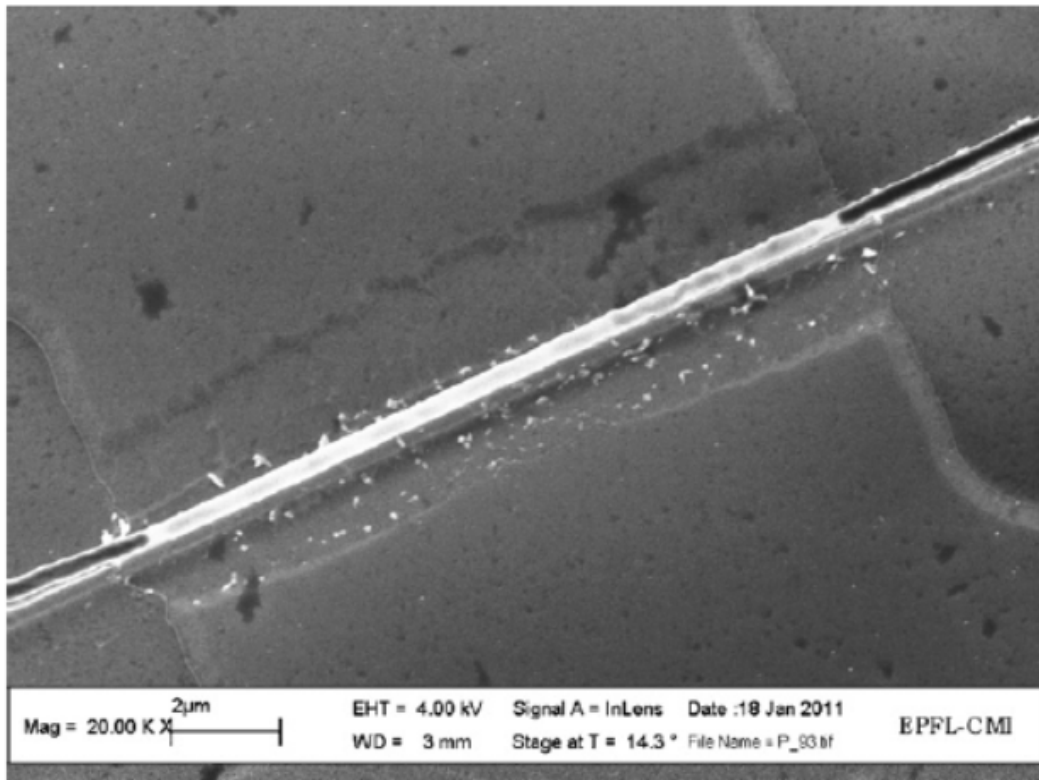


Fig. 2.22 SEM image of the SiNW after fabrication. The nano-wire is suspended between two *SiNi* electrodes [15].

and after the functionalization it is possible to notice the appearance of a voltage gap, which is symptom of the addition of bio-molecules bonded on the nano-wire itself as shown in Figure 2.23. When the biosensor actually senses the relative molecules for which the SiNW is functionalized, with an electric potential excitation, changes its dynamics increasing and decreasing the voltage gap.

The bio-sensing functionality of the device is performed as follows after the functionalization of the SiNW. The device is absorbed in a solution or in an environment in which there is the presence of the desired bio-sensed molecule. After the absorption, the SiNW is dried and put in a dry condition environment, where an electric potential excitation is applied on the *SiNi* electrodes. Depending of the concentration of the bio-molecule intended to be found in the solution, the voltage gap changes from the original functionalized non-bonded condition of the SiNW. The device also showed to be extremely sensitive to other kinds of factors regarding the analyzed solution, such as its pH [99].

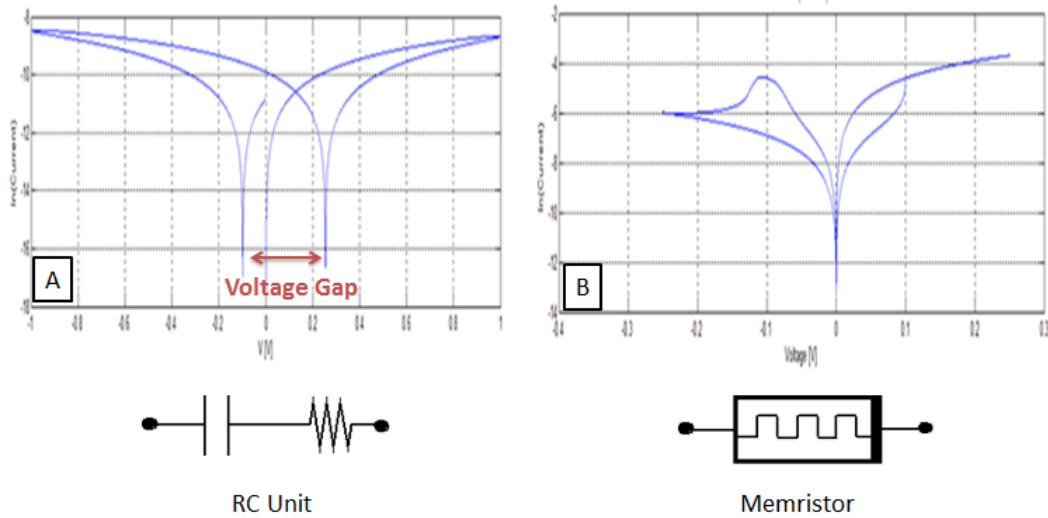


Fig. 2.23  $V - \ln(I)$  curves showed by the SiNW after (a) and before (b) functionalization, when applied a sinusoidal input signal. In panel-A it is evidenced the voltage gap that gives evidence of the covalent bonding of bio-molecules on the nano-wire. Under each panel are reported the circuit elements that show similar behaviour when excited by the same kind of signal.

The electrical dynamics of the SiNW are very interesting as show a memristor-RC switching behaviour under certain conditions. In order to design a model that fully describes this dynamics it is necessary to deeply uptake a broad knowledge of the memristor element and to compare it with the electrical behaviour of the studied device. As described in section 2.1, the memristor as it was first theorized by Professor Leon Chua in 1971 [1] can be described as a non-linear resistor capable of changing its value according to the "history" of the voltage applied to the element (flux controlled) or the total amount of current flowing through the device (charge controlled). Moreover, though from the previous sections of this work  $v - i$  curves are a satisfactory manner to describe memristors, the pinched loop can still be exploited as a useful tool to make a first classification of the element (i.e. whether it is a memristor or not). As from Chua's theory memristors, or more in general memristive elements must be able to show the following "fingerprints" [14]:

1. when excited with a periodic waveform, it must present a "pinched" hysteresis loop on the  $v - i$  curve (as shown in Figure 2.2);

2. the hysteresis loop must be frequency dependant resembling more and more to a passive resistor with the decrease of the period of the excitation waveform (still shown in Figure 2.2);
3. though charge or flux controlled, a memristor should always obey to Ohm's law as shown in equations (2.3) and (2.5).

Starting from these fundamental considerations, in the next paragraph it will be introduced an equivalent circuit that is able to reproduce the particular dynamics of the SiNW shown by Carrara *et al.* The circuit here reported implements an ideal memristor (on the basis of [26]) simulated through the GBCM model introduced in chapter 1 and explained in [21].

### 2.5.1 Electronic Approach Model

Through the electronic approach it is possible to design a simple equivalent circuit from the experimental data obtained from the SiNW. In order to design the equivalent circuit, it was necessary to have a deeper understanding of the behaviour of the device also depending on the frequency of the excitation waveform. In Table 2.4 are reported general overview observations of the frequency response of the system obtained through experimental data [100].

Table 2.4 SiNW Conditional Behaviour

Before Functionalization (BF)	Memristor Behavior
After Functionalization (AF)	Capacitor Addition
Frequency $\rightarrow \infty$	Voltage Gap Increase
Frequency $\rightarrow 0$	Voltage Gap Decrease

From the afore mentioned observation the circuit model shown in Figure 2.24 was designed. The voltage generator  $V_{in}$  coupled with resistance  $R$  form a "real" generator tacking into account all the internal resistance factors of the system, such as the ones that are given by the cabling and the electrode coupling with the SiNW. The actual system is described by the parallel coupling of the memristor  $M$  and the capacitor  $C$ . When a DC signal is applied to the system, the capacitor works as an open circuit, letting all the current flow through the memristor. When the frequency

is higher the memristance becomes higher than the resistance given by the capacitor leading to a  $RC$  series unit behaviour of the SiNW as given from experimental data.

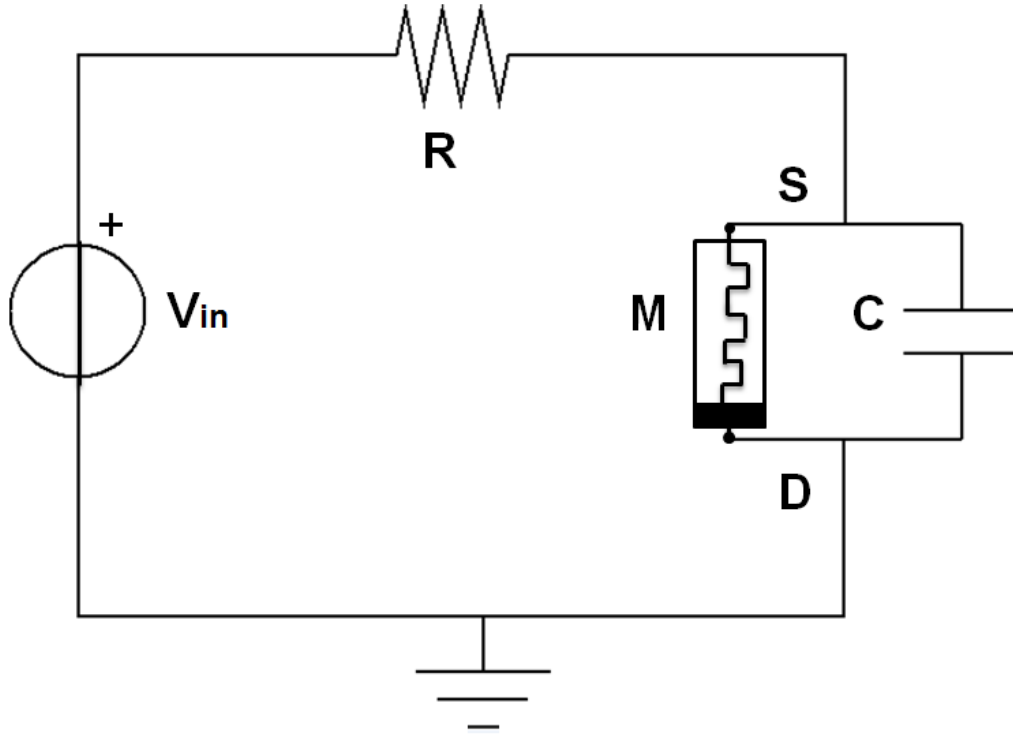


Fig. 2.24 SiNW equivalent electronic circuit. The values that were taken into account in order to evaluate the response of the simulation are the voltage drop over the SiNW ( $V$ ) and the total current flowing through the circuit ( $I$ ).

The circuit presented in Figure 2.24 was simulated numerically through SPICE simulation tools and analytically through Matlab. The equations that describe its dynamics are hereafter reported.

$$M(q) = R_{off} \left( 1 + \frac{\mu_v R_{on}}{D^2} q(t) \right) \quad (2.84)$$

$$I = \frac{V_C}{M(q)} + C \frac{dV_C}{dt} \quad (2.85)$$

$$V_C = V_{in} - (I_C + I_M)R \quad (2.86)$$

$V_C$  is the voltage drop on the capacitor  $C$  and on the memristor  $M$ .  $M(q)$  denotes the memristance under charge control ( $q(t)$ ).  $I_C$  and  $I_M$  are the currents flowing

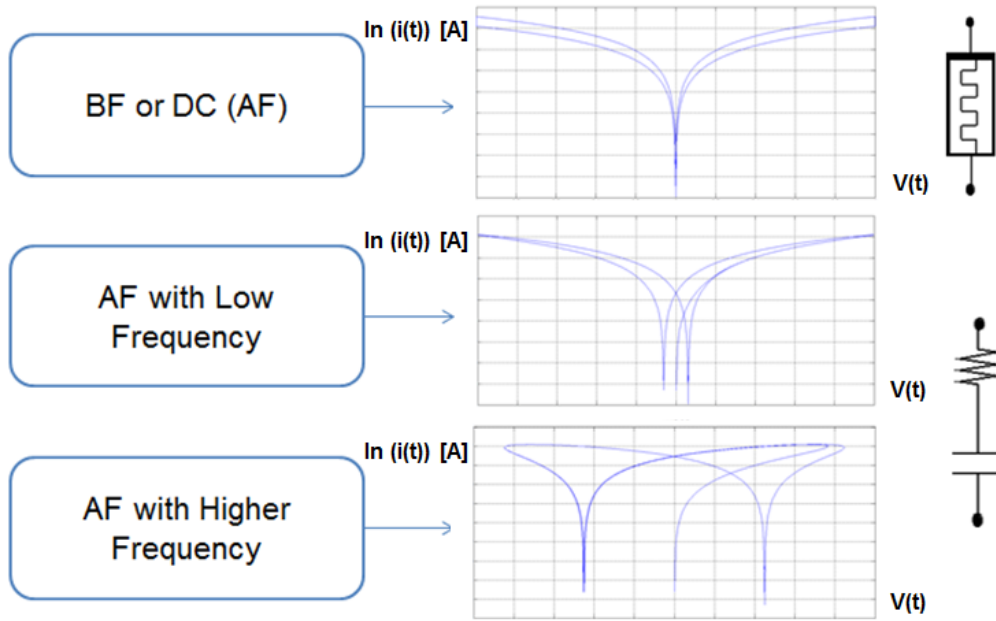


Fig. 2.25 Simulation results of the equivalent circuit model of the SiNW. Next to each  $V - I_n$  graph are reported the simulation conditions and the circuit element that generate such behaviour.

through the capacitor and the memristor respectively. In the first equation of structure 2.84  $\mu_v$  and  $D$  denote the ion motility of the oxygen vacancies and the thickness of the  $TiO_2$  bulk of the HP memristor model described in [2].  $R_{off}$  and  $R_{on}$  are the highest and lowest resistance values of the memristor  $M$  respectively.

Inserting equations (2.84) and (2.85) in (2.86) we obtain a differential equation over the Bernoulli's dominion. To solve the structure analytically it was necessary to approximate the memristor model with a piecewise linear memristor model function obtaining

$$V_C(t) = V_{C0}e^{-(A/C)t} + \frac{A \sin(\omega t) + C \omega \cos(\omega t)}{A^2 + (\omega C)^2} \quad (2.87)$$

$$A = \frac{R}{M(q)} + 1 \quad (2.88)$$

$$V_{C0} = -\frac{C \omega}{A^2 + (\omega C)^2}. \quad (2.89)$$

On the other hand in the SPICE simulation, the HP memristor model was rendered through the General Boundary Condition Memristor (GBCM) model described and developed by Ascoli *et al.* [21]. Both simulations (analytical and numerical) were performed using different excitation waveforms, equal to the ones used to obtain the experimental data. Both simulations were able to perfectly fit the experimental data and as shown in Figure 2.25 and to precisely reproduce the actual device's dynamics.

### 2.5.2 SiNW Memristor Classification

As explained in the paragraph 2.5.1 in order to model the device the HP memristor model was used. The element has been simulated through the GBCM model introducing the characteristics described in section 2.3. Under an electrochemical point of view the device has been studied in details by Puppo *et al.* in [101].

In their study it has been shown how charges are transported throughout the device. The charges themselves can be classified in different groups depending on the origin. First of all the as described at the beginning of this section, the SiNW is functionalized with bio-molecules that present a charged residuals. Secondly the spare electrons and vacancies given by the defects of the Si bulk composing the nano-wire must be taken into account when modeling charge transportation. Spare electrons and vacancies generate locally augmented and diminished charge densities respectively in the nano-wire. Moreover charged molecules present in the system at all levels, depending on their polarity, can be assumed of three types: donors (positive), acceptors (negative) and neutral traps.

In [101] it has been proved that the charge transportation on the device can be of three different kinds:

1. charge transport on the oxidation layer present on the surface of the SiNW (by diffusive and drift phenomena);
2. charge transport through the bulk of the nano-wire (still by diffusive and drift phenomena);
3. charge transport through the Shottky contacts at the electrodes (see [100] for clarifications).

Without entering in the details of the physical-mathematical description provided by Puppo *et al.* it is possible to notice, from equations (2)-(11) of their paper that regarding the surface transportation the current strongly depends on the number of acceptors and donors that are present ( $n_a$  and  $n_d$  respectively). In the other cases, these phenomena depend on the voltage drop on the whole device (bulk transport) and at the electrode interfaces (Shottky-based transport).

From the experimental data ([15, 99, 100]) it is clear that the presence of a dopant, or in other words a functionalization molecule, on the oxidation layer of the SiNW generates the capacitive behaviour described in the previous paragraphs of this section. In [101] it is shown that the local variations of  $n_a$  and  $n_d$  over time depend on the voltage drop over the device ( $V$ ) and these variations strongly affect the drift phenomena on the surface. On the other hand, the original charge density of the functionalizing molecule on the oxidation layer affects the diffusive current phenomena.

It results that the memristive effects are given by the other two transportation phenomena (Shottky and bulk charge transport). Regarding the bulk current, it can be considered as the sum of two distinct factors: a drift current, which depends on the resistivity of the  $Si$ , and a diffusion current which depends on the voltage drops over the two Shottky barriers at the electrodes (equation (9) of [101]). On the other hand the current components from the Shottky contacts depend as well on the voltage drop over the energy barrier (equations (10) and (11) in [101]). From these considerations the following descriptive memristor equations can be written:

$$q(t) = f(\varphi(t), V_j(t)) \Rightarrow i(t) = G(\varphi(t), V_j(t))V(t); \quad (2.90)$$

$$\dot{V}_j(t) = g(V(t), V_j(t)) \Rightarrow \dot{V}_j(t) = g(V(t), V_j(t)); \quad (2.91)$$

$$\dot{\varphi}(t) = V(t) \Rightarrow \dot{\varphi}(t) = V(t); \quad (2.92)$$

where  $V_j(t)$  is the voltage drop over the Shottky barrier which depends on the input voltage  $V_{in}$ . From these equations it is possible to state the the use of the chosen memristor model was appropriate for the performed simulations (paragraph 2.5.1) since the SiNW, when presenting memristive behaviour, acts as an ideal memristor.

## 2.6 Memristor Emulator Circuit Based on Static Non-linear Two-Ports and Dynamic Bipole

Since memristors are widely studied and the range of applications developed for these devices are getting broader and broader, circuital implementations exhibiting fingerprints of memristive behaviour become properly relevant. A class of memristor circuits was obtained by cascading a static nonlinear two-port with a dynamical one-port. In general, these circuits are classifiable as extended memristors [26] and may be controlled either in charge or in flux. The novel element from this circuit class here presented may also experience various complex behaviours including periodic oscillations and chaos. A thorough investigation of the rich nonlinear dynamics emerging in the proposed circuit may shed light into the most interesting engineering applications such a memristor may be suited for.

The leap in the use of memristive device became evident since further investigation took place in the field of CCNs and perceptrons [29, 41, 34]. Memristors are theoretically capable of maintaining more memory states in the same device, leading to new frontiers in electronic system development. In most cases, as afore mentioned, memristors have been exploited in the design of circuits able to perform machine learning [102]. In the following years several devices were designed and tested computationally and analytically. All these devices took inspiration from neural networks, and the memristor (or memristive elements) have been properly used to simulate biologic neuron synapses thanks to their incredible similarity in the dynamics with real biologic cells.

Another interesting path of research concerns the identification of new circuits falling into the class of extended memristors. The lack of possibility to use these kind of elements and their still poor availability set the mathematical modeling of this structures as the key factor for future developments in this field. In [61] it was theoretically proven that a circuit composed of a few passive two-terminal elements from classical circuit theory namely a two-port employing 4 diodes in Graetz bridge configuration, loaded by a linear filter consisting of an inductor in series with the parallel combination between a capacitor and a resistor behaves as an extended memristor at the input port of the full-wave voltage rectifier. In this paper we give proof to the possibility of developing a real ready-to-use circuit as the one presented in [61]. Exploiting structure given by the cascade between a static two-port of 4

nonlinear resistors and a dynamical one-port, defined by a DAE set falling into the class of extended memristors (see paragraph 2.2.3). The circuit presented also exhibits the 3 fingerprints of memristor behaviour as described in [14, 103].

### 2.6.1 Circuit Design and Analysis

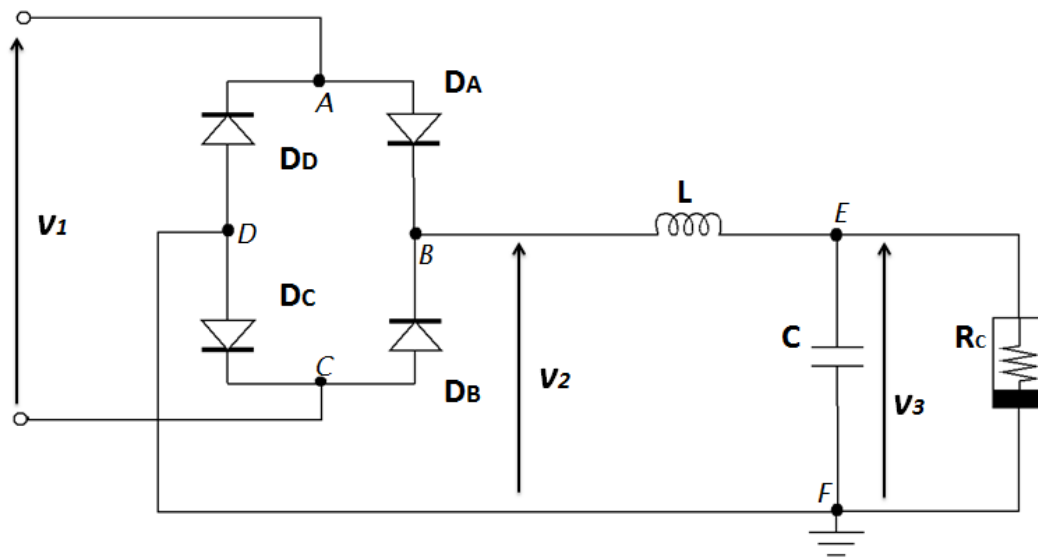


Fig. 2.26 Versatile circuit presented that shows memristive properties [104]. In the paper the currents flowing through the various elements and the voltages applied to them will be cited with  $i$  with the subscript of the interested element. For instance the current flowing in the diode  $D_A$  will be named  $i_{D_A}$ . The current entering the circuit from the voltage source  $v_1$  (flowing into node A and outflowing from node C) will be named  $i_{in}$ .

Figure 2.26 shows the proposed solution for the static one-port cascaded with the dynamic two-port. The port nodes A and C are the entrances of the extended memristor. Ports B and D are the entrances of the dynamic one-port.  $R_C$  is a nonlinear resistive element which, as it will be described afterwards in the paper, can be assumed as a Chua diode with continuous third-order dynamics. In Figure 2.26 the static two-port is represented by four diodes, that for the sake of proof will be at first described as nonlinear resistors.

Let the current  $i_k$  of nonlinear resistor  $\mathcal{R}_k$ ,  $k \in \{D1, D2, D3, D4\}$ , be expressed in terms of the voltage  $v_k$  across it through

$$i_k = I_1 \tilde{f}(v_k) + I_0, \quad (2.93)$$

where  $I_0 \in \mathbb{R}_-$  and  $I_1 \in \mathbb{R}_+$  are real parameters expressed in [A] units. Let us introduce the following assumptions on the real function  $\tilde{f}(\cdot)$ :

1. It is *one-to-one*.
2. Its sign is *positive* for all values of the argument.
3. It is differentiable everywhere with  $\frac{d\tilde{f}}{dv_k} > 0 \quad \forall v_k \in \mathbb{R}$ , i.e.  $\mathcal{R}_k, k \in \{D1, D2, D3, D4\}$ , is locally-passive.
4. It exhibits the zero-crossing property, i.e.  $I_0 = -I_1 \tilde{f}(0)$ <sup>1</sup>.
5. Given  $y_j = \tilde{f}(x_j), j \in \{1, 2\}$ , it fulfills  $\tilde{f}^{-1}(y_1) + \tilde{f}^{-1}(y_2) = \tilde{f}^{-1}(y_1 y_2)$ .
6. For any  $x_1, x_2 \in \mathbb{R}$ , it has  $\tilde{f}(x_1 + x_2) = \tilde{f}(x_1) \tilde{f}(x_2)$ .
7. It satisfies  $\tilde{f}(-x) - \tilde{f}(x) \propto x$ .

These assumptions define the class of functions  $\tilde{f}(\cdot)$  in equation (2.93). Elements from such class include functions of the type  $\rho^{\kappa(\cdot)}$ , with  $\rho \in \mathbb{R}_+$  and  $\kappa \in \mathbb{R}$ . Through the same assumptions the nonlinear resistive elements can be assumed to be ideal diodes described by Shockley's equation:

$$i_D = I_s (e^{\frac{v_d}{V_T}} - 1) = \tilde{f} \quad (2.94)$$

where  $i_D$  is the current density flowing through the diode,  $v_d$  is the voltage applied,  $V_T$  is the thermal voltage on the P-N junction (around 26mV) and  $I_s$  is the saturation current of the element. Furthermore, through the same assumptions and basic circuit theory analysis it is possible to understand that (still referring to Figure 2.26):

$$v_1 = v_{D_A} - v_{D_B}, \quad (2.95)$$

$$i_{in} = i_{D_A} - i_{D_D}, \quad (2.96)$$

---

<sup>1</sup>Assumptions 3) and 4) imply that  $v_k i_k \geq 0$  at all times, i.e. the 4 nonlinear resistors are also passive.

while the formulas for output voltage and current of the two-port are given by

$$v_2 = -v_{D_A} - v_{D_D}, \quad (2.97)$$

$$i_2 = -i_{D_A} - i_{D_B}. \quad (2.98)$$

Further, constraints are found to relate voltages and currents of each pair of parallel nonlinear resistors in the bridge, specifically

$$v_{D_B} = v_{D_D}, \quad (2.99)$$

$$i_{D_B} = i_{D_D} \quad (2.100)$$

for  $D_B$  and  $D_D$ , and

$$v_{D_A} = v_{D_C}, \quad (2.101)$$

$$i_{D_A} = i_{D_C}. \quad (2.102)$$

Figured the afore mentioned circuital constraints it is possible to study the memristor class of the circuit implemented. A memristor of order  $n$  (i.e.  $\mathbf{x} \in \mathbb{R}^n$ ) from the proposed class is characterized by the following properties:

1. It is a voltage (current)-controlled two-terminal element if  $v_{in}$  ( $i_{in}$ ) in Figure 2.26 denotes the input  $u$ . In the first (latter) case  $i_{in}$  ( $v_{in}$ ) represents the output  $y$ .
2. It is a voltage (current)-state one-port if  $v_2$  ( $i_L$ ) in Figure 2.26 is one of the  $n$  components in  $\mathbf{x}$ . In the first (latter) case a linear or nonlinear capacitor (inductor) with voltage  $v_2$  across it (current  $i_L$  through it) is part of the dynamical bipole.
3. Its second stage, i.e. the load to two-port, is a  $n^{th}$ -order dynamical one-port containing linear or nonlinear electrical components from circuit theory. The memristor is a volatile memory if the dynamical one-port is purely passive.

4. It may be modelled by a DAE set falling into the class of extended memristors.

In the case of a voltage controlled memristor several assumptions have to be made on the circuit proposed. For instance it is possible to express  $v_{DA}$  and  $v_{DB}$  using equations (2.95) and (2.97), and inserting the voltage constraint defined in equation (2.99) into the latter, as functions of  $v_1$  and  $v_2$  as follows:

$$v_{DA} = \frac{v_1 - v_2}{2} \quad (2.103)$$

$$v_{DB} = -\frac{v_1 + v_2}{2} \quad (2.104)$$

Replacing  $v_a$  and  $v_b$  with these expressions into equations (2.98) and (2.96), and inserting the current constraint defined in equation (2.100) into the latter equation, the input and output currents of the two-port may be cast as

$$i_{in} = I_1 \left[ \tilde{f} \left( \frac{v_1 - v_2}{2} \right) - \tilde{f} \left( -\frac{v_1 + v_2}{2} \right) \right] \quad (2.105)$$

$$i_L = -I_1 \left[ \tilde{f} \left( \frac{v_1 - v_2}{2} \right) + \tilde{f} \left( -\frac{v_1 + v_2}{2} \right) \right] - 2I_0 \quad (2.106)$$

Using assumption 7), from equation (2.105), after calculating the same current in terms of  $v_1$  and  $i_L$ , the memductance function  $G(i_L, v_1)$  may be expressed as

$$G(i_2, v_1) = \frac{1}{v_1} \frac{\tilde{f} \left( -\frac{v_1}{2} \right) - \tilde{f} \left( \frac{v_1}{2} \right)}{\tilde{f} \left( -\frac{v_1}{2} \right) + \tilde{f} \left( \frac{v_1}{2} \right)}. \quad (2.107)$$

which fulfills the condition  $G(i_2, 0) \neq \infty \forall i_2$ . The memductance function –as well as the state evolution function of the  $v_1$ -controlled  $i_L$ -state memristors depends on both state and input. As a result the  $v_1$ -controlled  $i_L$ -state circuits are *extended memristors*.

Concluding the circuit analysis, the nonlinear resistance  $R_C$  was assumed to be as afore mentioned a model of Chua's diode, which conductance is expressed in terms of  $v_3$ . By these means it is necessary to compute the voltage drop on the capacitor  $C$  in order to have the complete dynamics of the circuit.  $C$  is assumed to be a linear capacitor in parallel with a nonlinear element. The voltage applied to the resulting impedance is function of current  $i_2$  which was expressed earlier on the basis of the

dynamics of the diodes composing the static one port. Considering a normal  $RLC$  (with linear resistance) circuit it is possible to describe the associated equations as:

$$\frac{dv_3}{dt} = \frac{-i_2}{C} - \frac{v_3}{RC} \quad (2.108)$$

Let us assume that the current-voltage relation of  $R_C$  is the continuous cubic function  $i_{R_C}(v_3) = g_1 v_3 + g_3 v_3^3$ . Manipulating equations (2.105) and (2.108), the DAE set modelling this memristor is found to be (once again we set  $v_3$  and  $i_L$  as first and second component of the state vector):

$$\frac{dv_3}{dt} = -\frac{i_2}{C} - \frac{1}{C} (g_1 v_3 + g_3 v_3^3) \quad (2.109)$$

$$\frac{di_L}{dt} = \frac{v_3}{L} + \frac{2}{\kappa L \ln \rho} \ln \left( \frac{-i_L - 2I_0}{I_1 (\rho^{\kappa \frac{v_1}{2}} + \rho^{-\kappa \frac{v_1}{2}})} \right) \quad (2.110)$$

$$i_1 = (i_L + 2I_0) \frac{\rho^{-\kappa \frac{v_1}{2}} - \rho^{\kappa \frac{v_1}{2}}}{\rho^{\kappa \frac{v_1}{2}} + \rho^{-\kappa \frac{v_1}{2}}}, \quad (2.111)$$

Regarding the nonlinearity of the resistors in the static two-port, we let  $\rho = e$ ,  $I_1 = 0.9A$ ,  $I_0 = -0.9A$ , and  $\kappa = 1V^{-1}$ . The parameters in the current-voltage relation of Chua's diode are set to  $g_1 = g_0 n_1$  and  $g_3 = g_0 n_3$ , with  $g_0 = \frac{2}{3}S$ ,  $n_1 = -\frac{8}{7}$  and  $n_3 = \frac{4}{63}V^{-2}$ .

## 2.6.2 Spice Modeling and Simulation Results

The circuit afore described shows various elements that can be assimilated to commercial devices easily available on the market. The proposed circuit was set as a netlist on spice and a simulation was ran in order to better essay the memristive behaviour of the device. The state equations afore explained were not inserted in the netlist, as such the program automatically deduces the equations performing a numerical simulation.

The parameters for the inductor and capacitor in the dynamic load of the static two-port were set to:  $L = 2.5\mu H$ ,  $C = 4\mu F$ . Chua's diode was set as a voltage driven current source with the cubic continuous dynamics mentioned in the previous section.

The four diodes were set to have the same parameters which are:  $I_s = 2.682nA$  and  $V_T = 25mV$ , referring to equation (2.94).

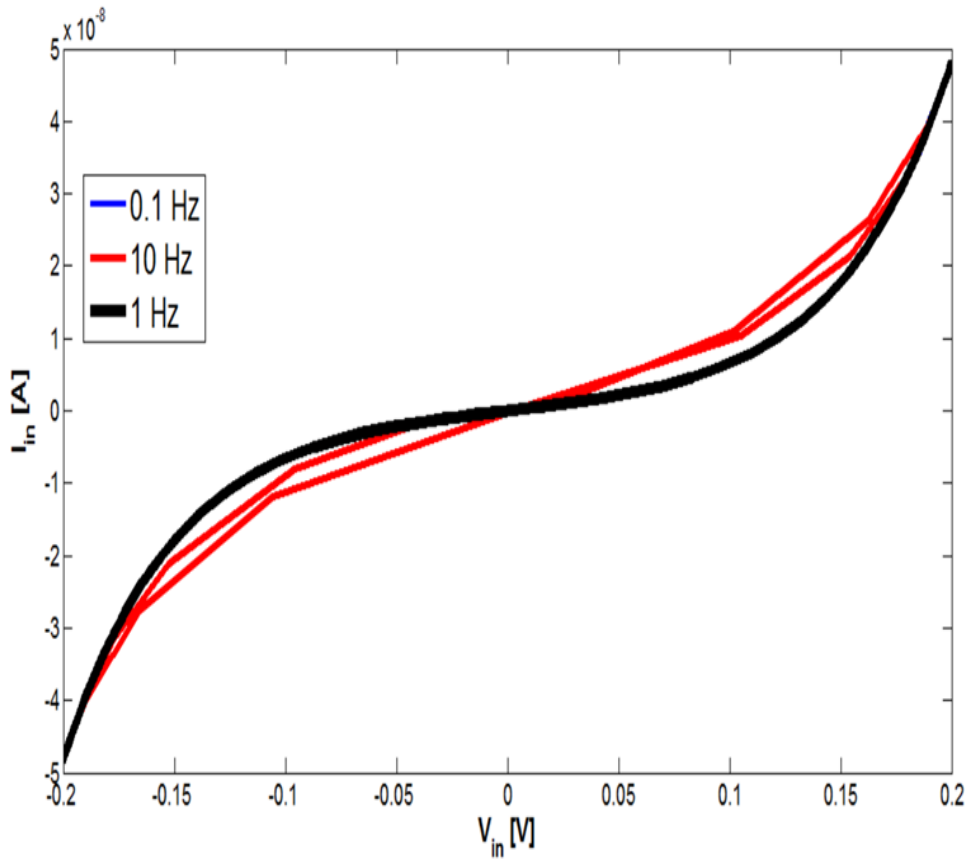


Fig. 2.27  $V$ - $I$  curve obtained by applying three different sinusoidal input voltages to the circuit. All three signals have same amplitude ( $0.2V$ ), but differ from the frequency ( $0.1$ ,  $1$  and  $10Hz$ ). In the figure is mentioned the output of the  $0.1Hz$  sinusoid but it is not visible since it is completely overlapped by the output of the  $1Hz$  signal.

Three different sinusoidal signals were sent to the device with different frequencies ( $0.1$ ,  $1$  and  $10Hz$ ). All three sinusoids have the same amplitude ( $0.2V$ ). Figure 2.27 shows the output of the system to the different voltage signals applied. The mentioned figure shows only two traces out of three. The output of the system to the input signal of  $0.1Hz$  was found completely overlapped to the one of  $1Hz$ . In any case the circuit proposed shows dynamics which are assimilable to a memristive device. Though the loop is very thin for lower frequencies, it gets sharper for higher ones. This characteristic is one of the properties described by Professor Chua in [14].

From the Spice simulations results it is proven that the memristive class circuit proposed in this paper can be easily built. As afore mentioned in the introductory section the lack of memristive devices renders several difficulties to developers to pass from a mathematical modeling stage to a more implementing phase. The possibility to build circuits of this kind of class, given that the elements used in the simulation can be exploited also in SMD technology for PCB implementations without major space expenses, can lead to a second step in developing systems that are intended to substitute in time classic digital electronics.

## Chapter 3

# Memristors-Based Systems for Machine Learning

Memristors have been described in chapters 1 and 2 as emerging devices that promise the efficient implementation of *synapses* in artificial neural networks. Memristors have permitted the processing and analysis of a large amount of data in evolutionary learning artificial systems through signals that can be assimilated to human brain-like neurotransmitters and synapses. In this chapter will be presented a memristor-based circuitual system capable of implementing the Stochastic Belief Propagation Inspired (SBPI) algorithm, which takes inspiration from the Belief Propagation Inspired (BPI) [34]. Such algorithm is able to efficiently classify sets of data inputs inferring the related imposed rule to the various given sets, using binary (switchlike) synaptic weights. Neural Networks trained with these kinds of algorithms are able to learn a number of associations close to the theoretical limit in time that is sublinear in the number of input. It is well known that perceptrons with step function type nonlinearity can be implemented by a suitable class of Cellular Neural/Nonlinear Networks [102].

First, as introduced in chapter 1 it will be shown how memristors were described through a mathematical model that is ready to use and is able to emulate several kinds of memristor models. This model is known as the *Generalized Boundary Condition Memristor* (GBCM) model, developed by Ascoli *et al.* [21], and it will be described in details in the following sections. It will be shown, through the use of the GBCM, how to implement the key features of a machine learning algorithm through real world circuitry.

The following chapter will introduce the design of the memristor based perceptron that implements SBPI algorithm. Moreover it will present several essays and simulations that have the scope to prove the efficacy of the system and its data classification capabilities relative to the algorithm's original mathematical formulation.

### 3.1 General Introduction to Perceptrons and SBPI

Memristors are often used to implement biologically inspired algorithms, such as in neuromorphic systems thanks to their low power consumption, their capability mimicking a synapse. Besides power consumption, another important factor is element density. The human brain's estimated neuron population is around  $10^{11}$  [105–107]. CMOS technology and electronic elements that can be used to simulate or emulate simplified biologic synapses, such as micro-processors or common control logic technology, use a large amount of space when implemented on embedded boards. The use of memristors for these purposes is the key factor for the growth of this field in recent times considering its low energy consumption and its reduced size [2]. Recently Prezioso *et al.* demonstrated that it is possible to implement simple neural networks (in his case a single layer perceptron) with only memristor crossbars excluding CMOS components [108]. Despite the low number of memristors used in their work, it is a valid proof-of-concept for future developments of *solo* memristive neuromorphic systems.

The general interest on neuromorphic systems arose thanks to the fact that bigger and bigger amounts of data have to be processed with higher and higher efficiency every day. Big data is a problem that arises in many aspects of everyday life and which usually involve critical decision making [32]. For this reason modern life schemes are powered by machine-learning, which is the engineering response to the problem of processing a great request of information automatically and rapidly [109]. Machine learning systems are used to identify objects in images [110], transcribe speech into text through speech recognition algorithms [52, 111], or as in this specific case to classify data patterns. Biologically inspired and brain-like algorithms, such as neuromorphic systems aided in this problem thanks to their perspective low power energy consumption. Three orders of magnitude of improvement was given by digital technology compared to the first speak-and-spell devices [112]. Neuromorphic systems implemented on computational devices promise a further

improvement of five orders of magnitude with respect to analog signal processing approaches.

The model network used as a proof-of-concept is the simplest possible, i.e. a single layer network known as the perceptron [113]. This kind of network has limited computational capabilities by itself, but it is the building block of multi-layer networks which are at the heart of the recent resurgence of interest in applications of neural networks in machine learning and artificial intelligence applications. The idea behind this kind of approach is to mimic the learning process occurring in real brains, in which the system is able to autonomously infer rules from examples, and subsequently apply those rules when new inputs are presented. This kind of learning is widely believed to occur through mechanisms of synaptic plasticity. Despite a huge amount of experimental data documenting various forms of plasticity, as e.g. long term potentiation and long term depression, the mechanisms by which a synapse changes its efficacy and those by which it can maintain these changes over time remain unclear. In artificial networks, it is usually assumed that the synaptic efficacies can assume a large number of different values, and the network themselves are generally trained by algorithms which are variants of the stochastic gradient descent algorithm (also known as back-propagation in this context [114]); in the case of single layer networks, this approach leads to what is generally known as the "perceptron algorithm". A prototype of an electronic device which implements a perceptron, using memristors to model the synapses, and uses the perceptron algorithm to perform *in situ* learning, was recently demonstrated by Alibart *et al.* in [115]. The main difficulty in this kind of approach lies in the inherent limitations of current memristive technology, which offers a relatively low level of consistency and robustness, while the learning algorithm employed relies on precise control of the synaptic states.

Real world synapses are also working in an extremely noisy environment, and thus need to be vary robust to perturbations and – presumably – to not rely excessively on computational precision. Experimentally determining the granularity of the synaptic efficacy is an arduous task; recent experiments, however, have suggested that each synapse would only be able to store very few bits of information, between 1 and 5 [116, 117]. This low synaptic precision can be very helpful in reducing the sensitivity of the devices to noise, while on the other hand posing problems to a naïve implementation of a classic learning algorithm such as back-propagation. The Stochastic Belief-Propagation-Inspired (SBPI) algorithm [34] has the proposition

to overcome the problem of training neural networks with binary synapses while still being sufficiently simple to be biologically plausible. As it turns out, for the reasons explained above, this algorithm also appears to be particularly well suited for a memristor-based hardware implementation: it is similar to the standard perceptron learning algorithm, and thus is very simple, with two core differences:

1. it uses an "internal" (or "hidden") multi-state variable for each synapse, which however is only required during learning and has very limited requirements in term of precision and robustness;
2. it requires an additional rule for synaptic transitions that occur only if a currently presented pattern is "barely correct", a condition which is easily detectable.

On tests performed and presented in the following sections of this chapter on random classification and generalization tasks, this algorithm was shown to be able to learn a number of associations close to the theoretical limit in a time that is almost linear in system size, and to be remarkably robust to different kinds of noise. The algorithm can even to some extent be generalized to multi-layer networks, and perform well on real-world classification tasks [118], thus making the perspective of a hardware implementation even more appealing.

### 3.1.1 Stochastic Belief Propagation Inspired Algorithm

Stochastic belief propagation inspired algorithm represents one of the most promising learning strategy that has been developed in the last years with the advance of machine learning techniques. Such techniques have the scope to train Neural Networks (NNs) to react automatically to given input pattern without a previous programming stage. Recently it has been shown that the BPI algorithm permits to implement pattern recognition systems by means of neural networks with binary synapses and binary output.

The simplest BPI-based neural network (i.e. the perceptron) with  $N$  presynaptic binary input  $u_i \in \{0, 1\}$  and one binary output  $y \in \{0, 1\}$  is described by the following equation (see [34] for a detailed analysis):

$$y(t) = \sum_{i=1}^N \Theta[w_i(h_i(t))u_i(t) - \theta] = \sum_{i=1}^N \Theta[y_i - \theta] \quad (3.1)$$

where  $\Theta[\cdot]$  is the Heaveside function and the evolution of the binary synapse  $w_i = \Theta(h_i(t)) \in \{0, 1\}$  depends on a "hidden internal variable"  $h_i(t) \in \mathbb{R}$ .

The statistical and theoretical properties of NNs with SBPI are extensively studied by Baldassi *et al.* have shown that:

1. such a system is able to learn a number of associations close to the theoretical limit in time that is sublinear in  $N$ ;
2. the performance of the NN with BPI is optimal for a finite number of hidden states that becomes very small for sparse coding;
3. the proposed algorithm is the first on-line algorithm that is able to achieve efficiently a finite number of patterns learned per binary synapse

As afore mentioned the SBPI algorithm shares similarities with the standard perceptron algorithm [113]: training patterns are presented to the network one at a time, together with a desired output, and in case of an error a signal is back-propagated that can modify the synaptic values in a direction which makes it less likely to repeat the error in the future. At variance with the perceptron learning scheme, the changes only affect an internal ("hidden") variable in each synapse, which then in turn determines the synaptic weights, which are binary. The algorithm also has an additional update rule, which is applied in case the presented pattern has been classified correctly, but only barely so.

From what mentioned above, it is possible to indicate with  $N$  the size of the network (the number of synapses), with  $h_i \in [-1, 1]$  the hidden variables (where  $i \in \{1, \dots, N\}$  is the index of the synapse), and with  $w_i \in \{0, 1\}$  the binary synaptic weights. At any given time, the synaptic weights are determined from the hidden states as follows:

$$w_i = \frac{1}{2} (\text{sign}(h_i) + 1) \quad (3.2)$$

The hidden states  $h_i$  are discrete variables which can assume  $K$  different states, equally partitioned between positive and negative values.

Given a set of  $p = \alpha N$  binary patterns  $\zeta^x \in \{0, 1\}^N$ , where  $x \in \{1, \dots, p\}$  and  $\alpha > 0$  is a parameter that describes the size of the training set, two kinds of outputs must be considered: the desired output  $\sigma_d^x \in \{0, 1\}$  is provided by the user and describes the association rule which the system needs to infer, while the real output  $\sigma^x$  on the other hand is calculated for each pattern  $x$  as

$$\sigma^x = \Theta \left( \sum_i^N w_i \zeta_i^x - \theta \right) \quad (3.3)$$

where  $\Theta(\cdot)$  is the Heaviside function and  $\theta$  is the threshold for the current outflowing from the system, according to equation (3.1). At each discrete time  $\tau$ , a pattern  $\zeta^\tau$  is chosen randomly from the training set, and from that and the current state of the network (encoded in the weights  $w^\tau$ ) we need to compute the "stability parameter"  $\Delta = (2\sigma_d^\tau - 1)(I - \theta)$  where  $I = \sum_i w_i^\tau \zeta_i^\tau$ . Note that  $\Delta < 0$  implies that the network made an error. The learning scheme then consists in choosing one of 3 update rules depending on the value of  $\Delta$ , as follows:

R1) if  $\Delta > 1$ , then  $\forall i: w_i^{\tau+1} = w_i^\tau$  (i.e. do nothing);

R2) if  $\Delta < 0$ , then  $\forall i: h_i^{\tau+1} = h_i^\tau + \frac{1}{K} \zeta_i^\tau (2\sigma^\tau - 1)$ ;

R3) if  $0 \leq \Delta \leq 1$

a) if  $\sigma^\tau = 0$ , with probability  $p_s$ , if  $w_i^\tau = 0$ , then  $h_i^{\tau+1} = h_i^\tau - \frac{1}{K} \zeta_i^\tau$ ;

b) otherwise do nothing.

The hidden variables  $h_i$ , as mentioned above, can assume a number  $K$  of values (states), and their initial value is not particularly important. The number  $K$  of states should generally scale as  $\sqrt{N}$  and has an optimum whose precise value depends on the details of the problem under consideration. The probability  $p_s$  in rule R3 must be larger than 0 and also generally has an optimal value which leads to the highest storage capacity and/or fastest convergence to a solution. Simulation experiments, however, showed that the precise choice of neither of these two parameters is critical to achieve good performances, provided both are sufficiently large.

As it will be shown in the next sections, the binary synapses with hidden state can be accurately emulated by means of a memristor thanks its property of being modulated via flux or charge and eventually some additional state variables. Following the definition of memristor given in [1, 26], considering equations (2.3) and (2.5)

it is possible to write  $\bar{y}_i = M(x_i; \bar{u}_i)\bar{u}_i$  where  $x_i$  is a memristor state variable,  $M(\cdot)$  is the (normalized) memconductance and  $\bar{y}_i$  and  $\bar{u}_i$  are the (normalized) current and voltage, respectively. Assuming that the (normalized) voltage applied to memristor  $\bar{u}_i$  is the binary pulse  $u_i$  (i.e.  $\bar{u}_i = u_i$ ), the (normalized) current has a binary values ( $\bar{y}_i \in \{0, 1\}$ ) defined as follows:

$$\bar{y}(t) = M(x_i, u_i)u_i = H[G_{on}x_i + G_{off}(1 - x_i) - G_\theta]u_i \quad (3.4)$$

where  $G_\theta = 0.5(G_{on} + G_{off})$ ,  $G_{on}$  and  $G_{off}$  are memductance of the memristor at the high and low conductive states respectively. It follows that the perceptron composed by a single layer of memristor binary synapses is able to implement the SBPI algorithm, considering equation (3.1).

From what above described it is possible to note that that, since the actual output of the device only depends on the sign of  $h_i$ , and since the update rules only define increments and decrements of those quantities with no regard for their actual value except for the sign, this system is inherently capable to deal with significant levels of noise and heterogeneities in the behaviour of the memristive elements. In other words, the values of  $h_i$  don't need to be controlled with the same level of precision and reliability which is commonly required in standard digital electronic elements (and which would be required by a more traditional neural network model with multi-state synapses and trained via back-propagation such as the one prototyped in [115]).

## 3.2 Memristor-Based SBPI Perceptron Design and Implementation

In the following paragraphs it will be presented the layout and the design of a memristor based circuit capable of implementing the afore described SBPI algorithm. The circuit was designed on a Spice simulation software and has been assessed to understand whether the system is able to reproduce with fidelity the desired learning scheme.

The choice of the correct memristor model, that is capable of simulating the desired element to implement in the system is crucial for the understanding of the

system's behaviour during its functioning. Taking inspiration from the work of Ascoli *et al.* (the GBCM model) it is possible to simulate with high efficacy a wide range on memristive elements based on their behaviour.

In the following paragraphs of this section a brief description of the GBCM is provided as well as a deep insight of the memristive circuit used for this analysis.

### 3.2.1 Generalized Boundary Condition Memristor Model

From the considerations of Prof. Eshraghian [119] a good memristor model should take into account activation-based dynamics in certain physical memristors, such as memory cells exhibiting bipolar off-to-on (on-to-off) resistance switching under supra-threshold excitation due to dynamic metallic filament formation (rupture). Let  $D$  denote the length of a nano-film and  $x = w/D \in [0, 1]$  represent the longitudinal extension of the conductive part of the nano-film (e.g. the length of the  $TiO_{2-x}$ -based layer in the Titanium dioxide memristor or the length of the metallic filament in CBRAMs). The model equations are:

$$dx/dt = ki(t) f_p(x(t), v(t)) \quad (3.5)$$

$$i(t) = W(x(t))v(t) \quad (3.6)$$

where  $k \in \mathbb{R}$  is a constant depending on physical properties of the memristor (its dimensions are  $C^{-1}$ , thus it is also referred to as memristor charge normalization factor).  $W(x(t))$  describes the state-dependent memory-conductance expressed by:

$$W(x(t)) = \frac{G_{on}G_{off}}{G_{on} - \Delta Gx(t)} \quad (3.7)$$

where  $G_{on}$  and  $G_{off}$  indicate the memory conductance of the device in the on- and off- state respectively.  $\Delta G = G_{on} - G_{off}$ . On the other hand  $f_p(x(t), v(t)) \in [0, 1]$  is a parametrizable function that describes the activation dynamics of the device under boundary conditions. In our model  $f_p(x(t), v(t))$  is described as follows:

$$f_p(x(t), v(t)) = b + \frac{a-b}{2}(\text{sign}(u - u_{t0}) - \text{sign}(u + u_{t1})) \quad \text{if } x \in (0, 1) \quad (3.8)$$

$$f_p(x(t), v(t)) = c \text{ stp}(u - u_{th0}) \quad \text{if } x = 0 \quad (3.9)$$

$$f_p(x(t), v(t)) = c \text{ stp}(-u - u_{th1}) \quad \text{if } x = 1 \quad (3.10)$$

where  $a$ ,  $b$  and  $c$  are constant parameters that depend on the physical properties of the material regarding the device. The values  $u_{t0}$  and  $u_{t1}$  are the energy thresholds needed to observe an increase of the evolution of the activation and deactivation dynamics respectively, and  $u_{th0}$  and  $u_{th1}$  are the energy thresholds needed to observe a formation or a rupture of the oxide filament respectively.  $\text{sign}(\cdot)$  and  $\text{stp}(\cdot)$  are unitary sign and step function respectively. In the Figure 1.2 shown in the work of Ascoli *et al.* [21] it is can be observed that the memristance *per se* is controlled through the capacitor  $C$  which is connected to two state cells (on and off). These two cells have the purpose of maintaining the charge of the capacity in its boundary given conditions. In our case the voltage with which it is possible to charge  $C$  was set to be  $v_x \in [0V, 1V]$ . The activation cell charges the capacity following the trend set by  $f_p(x(t), v(t))$  when  $x(t) \in (0, 1)$ .

### 3.2.2 Memristor-Based Perceptron Circuit Design

In order to implement a circuit able to perform the tasks required for the SBPI algorithm, it was necessary to generate a binary response to the  $\zeta$  patterns presented to the system. Figure 3.1 shows the circuit that was designed to enable a binary response for each memristor implemented in the system, named Binary Synapse Unit (BSU). In figure are represented two branches, one named "reference" branch and the other "synapse" branch. The latter is recognizable from the figure since it is the one connected with the memristor. The voltage source on the "synapse" branch  $V_s$  has the scope to deliver the given input to the system ( $\zeta_i$ ) or to give an impulse able to change the memristance according to the SBPI algorithm (see paragraph 3.1.1 for details). In other words the impulses received by the memristor have to be of two kinds: "reading" inputs and "writing" inputs, which will be characterized in paragraph 3.3.1. When a "reading" input is delivered by  $V_s$ , the currents flowing through the "synapse" branch, and so through the memristor, must be summed and compared with the reference current ( $I_{\text{ref}}$ ) representing the threshold. Still in Figure 3.1 the resistance on the "reference" branch must have a value equal to half of the memristive dynamics ( $R_{\text{mem}} = (R_{\text{off}} + R_{\text{on}})/2$ ). This choice was done in order to compute a "high" or "low" value of  $w_i$  with respect to a  $h_i$  state supra- or under-threshold.

A current comparator was designed with a pMOS current mirror. In order to prevent an inverse flow of current from the memristors, a nMOS current mirror was used. Both are shown in Figure 3.2. The two outputs were then compared through

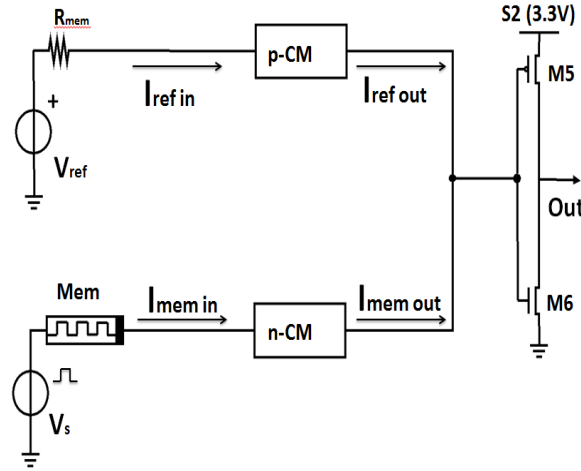


Fig. 3.1 BSU implementing a memristor. In the figure "CM" stands for Current Mirror.  $V_s$  and  $V_{ref}$  are the input and reference voltage generators of the binary synapse unit. "Mem" identifies the memristor in the device. Refer to the following figures for the specific circuit element implementation.

the use of a CMOS comparator in order to obtain two logic states (0 or 1), depending on the current flow from the memristors. CMOS technology in fact is capable of a current "pull-up" and "pull-down" thanks to its pMOS-nMOS connections. In this case the CMOS system was cabled as a logical NOT port. All the CMOS logic and the circuit elements of the system are powered through the pins S1, S2 and S3 (referring to Figures 3.1, 3.2 and 3.4) from a supply voltage  $V_{Al} = 3.3V$ .

In order to perform the SBPI algorithm all the outputs of each binary memristor unit must be somehow summed and, referring to equation (3.3), compared with the threshold  $\theta$  and to compare the outputs of the system with the desired response  $\sigma$ . Figure 3.3 shows the Memristor Contribution Sum Unit (MCSU) which was implemented with an op-amp with an adder configuration (in figure labeled as  $\Sigma$ ). As in most cases, also the SBPI perceptron is made up by an array of synaptic elements, as to render more realistic soma dynamics [120–126]. This solution permits to sum the binary voltages instead of the currents which results to be more efficient on the circuitry design level, avoiding the entrance of noise phenomena. The output of the MCSU ( $I_{Sum}$ ) is sent to the sigma Calculator Unit (SCU) depicted in Figure 3.4. This unit compares the output of the memristor binary synapses at the given time point  $\tau$  with the desired output of the specific pattern  $\zeta^x$ . The  $\theta$  threshold is given by the  $V_\theta$  (Figures 3.3 and 3.4) through a voltage supplier and the comparison is made

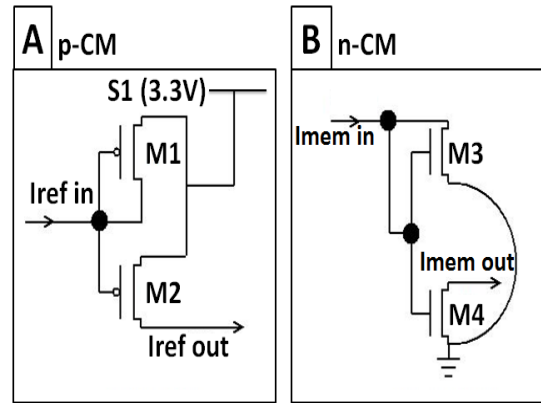


Fig. 3.2 (a) pMOS current mirror and (b) nMOS current mirror layout.  $I_{ref}$  and  $I_{mem}$  represent the reference current and the memristor current that flow through the resistive or memresistive elements, respectively, present in the two branches. Refer to Figure 3.1 for the complete layout implementation.

by pMOS/nMOS current mirrors as in the binary synapse generator unit (shown in Figure 3.1).

The whole system was then connected to a control unit (CU) whose purpose is to perform a back propagation of the resulting  $\Delta$  for the given pattern. During the back propagation the CU performs three different tasks. If the stability parameter shows that for the analyzed pattern its desired output is given correctly by the system, and that the flipping of single variable would not change this ( $\Delta > 0$ ), then sends to the binary synapse, as well to the rest of the system, the next pattern in line. In the case the sigma calculator unit computes a given  $\Delta < 0$ , the CU sends a "writing" input to the binary synapse able to change the memristances to the according  $h_i$  state (rule R2), then sends the next input pattern in line. Lastly, when a small  $\Delta$  is computed (more precisely  $0 \leq \Delta \leq 1$ ), it sends "writing" inputs to the memristors according to the afore described rule R3. Rule R3 is triggered by the stochastic variable  $p_s$ , but in order to understand which memristance has internal state  $w_i$  close to 0 a positive unitary writing input, followed by a negative one (zero mean signal) is sent to each BSU singularly. If during this phase the output of the single synapse changes then the given memristance is changed according to the rule. As afore mentioned, the precise characterization of the "writing" and "reading" signals is presented in paragraph 3.3.1.

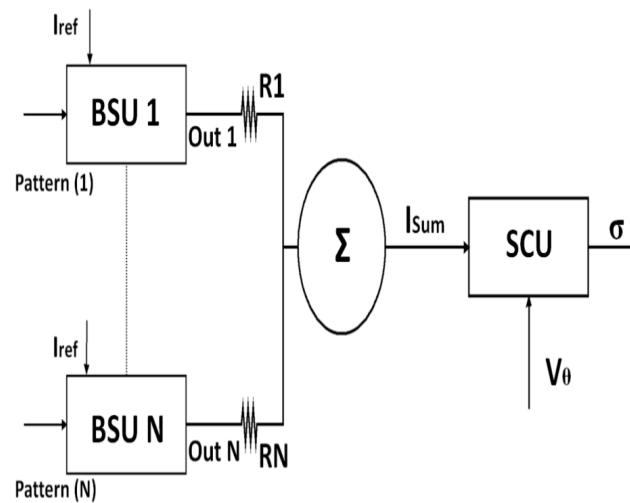


Fig. 3.3 MCSU. The elements represented in the figure refer to the other descriptive circuit figures. The *SCU* is the sigma calculator unit depicted in Figure 3.4, while the *BSU* are the binary synapse units depicted in Figure 3.1. The resistances  $R_1$  to  $R_N$  have all the same value, so that the contribution of each synapse to the system depends only on the memristance value obtained through the algorithm.

In conclusion, the CU can be seen as a changing state machine with nine states. Figure 3.5 shows the workflow diagram of the CU and the conditions for the state changes. State 0, which resets the system, is called when the perceptron is programmed to learn a new rule from a whole new set of  $\zeta$  patterns. In this case all the memristors are set to the internal state  $h_i = -1$  so  $R_{\text{mem}} = R_{\text{off}}$ . The pattern generation implemented in State 1 on the other hand has the purpose to send to the binary synapses the next pattern of the set. As mentioned at the beginning of this paragraph, the inputs sent to the memristors must be of two kinds: a "writing" one and a "reading" one. While in the first case the impulse has the ability and the scope to change the memristance, and thus the internal state of the given element, the reading input must not change the memristance, but must generate at least a low current flow through the memristor.

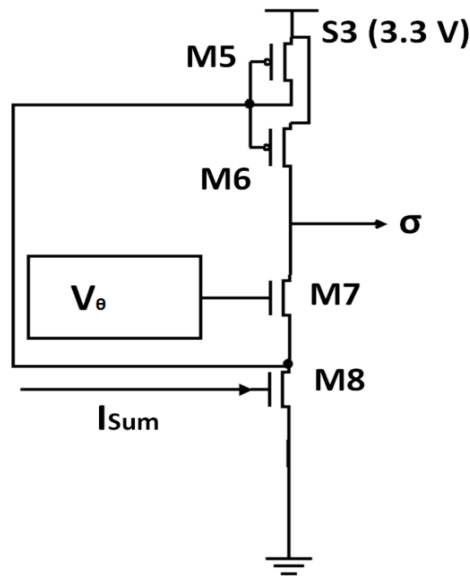


Fig. 3.4 SCU. The output of this unit ( $\sigma$ ) is the input of the control unit (CU) and with respect to its value the SBPI perceptron will perform the algorithm according to the computed stability parameter  $\Delta$ .  $I_{Sum}$  is the current out-flowing from the MCSU (refer to Figure 3.3), acting as an input to this unit in order to perform the SBPI.

### 3.3 Functional and Learning Efficiency Essays on the Memristive Perceptron

The circuitry described in paragraph 3.2.2 was designed on a Spice simulation tool, and several essays were performed in order to evaluate the functionalities of the binary synapse with the GBCM model and the learning efficiency of the system itself. The functional simulations were done on simple circuits composed of the memristor alone connected to a voltage supply and an ammeter and on the binary synapse system. In the first case the goal was to evaluate the writing and reading inputs since, as previously explained, the reading impulses must not change the memristance, so the element must work as a passive resistor. The trials on the binary synapse circuit alone were performed to evaluate and dimensionally establish the voltage  $V_{ref}$ , in order to set the binarization threshold at half of the memristor dynamics.

In a second set of tests, the whole perceptron was trained, to evaluate the learning behaviour and efficiency of the system while varying the  $\theta$  threshold and the  $\alpha N$  number of  $\zeta$  patterns per set, and subjecting the system to different kinds of noise conditions. For all the mentioned simulations (all performed on PSpice), the memris-

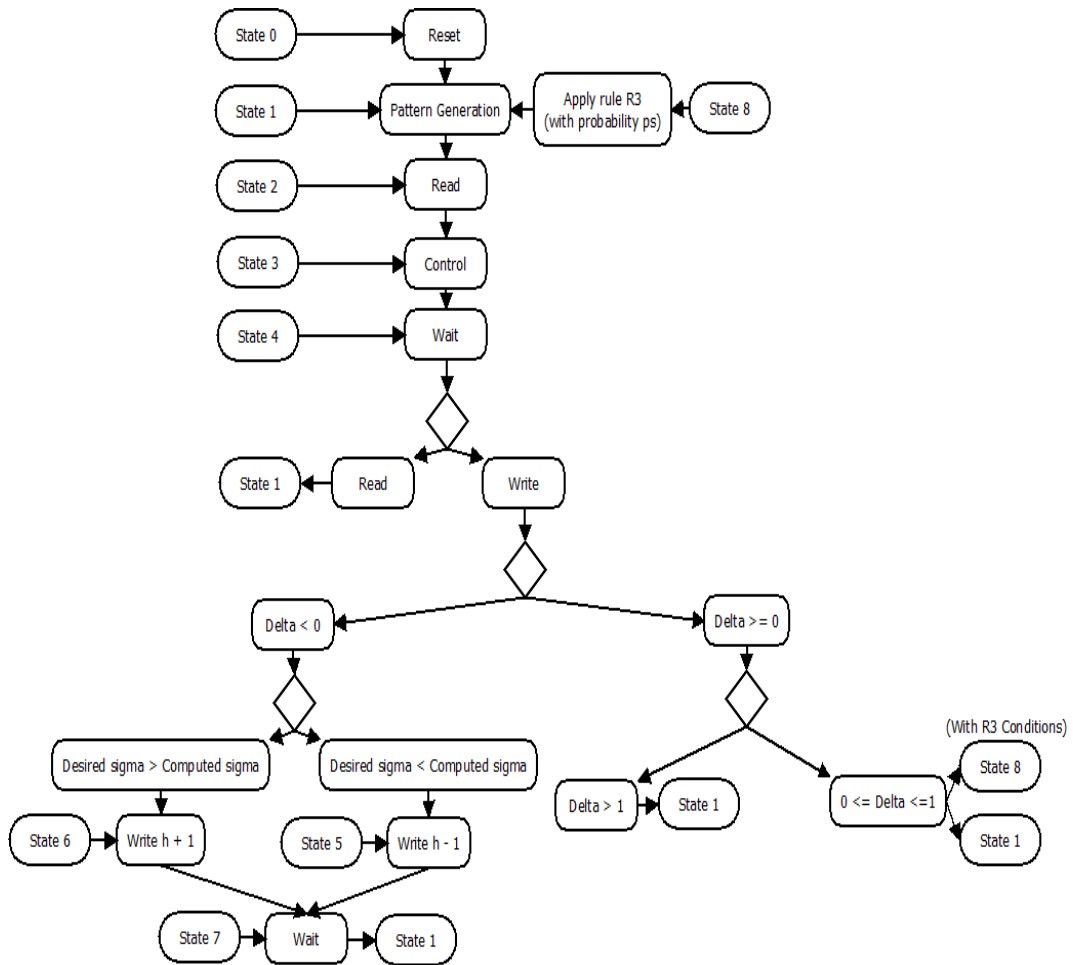


Fig. 3.5 Workflow diagram of the Control Unit designed as a changing state machine.

tors were set to have  $R_{\text{on}} = 10\Omega$  and  $R_{\text{off}} = 1k\Omega$  and the perceptron was mounted implementing  $N = 700$  memristors. In the following subsections each trial will be presented with their respective results, and their implementation will be explained more in detail.

### 3.3.1 "Read" and "Write" Impulse Characterization

As previously described, a simple circuit presenting a memristor coupled with a voltage source and an ammeter was designed and used for this essay. Considering that in our specific case the perceptron was designed to be controlled by voltage impulses to the memristors, our elements are to be considered flux-controlled. The perceptron as presented in the introductory section of this work is based on logical digital circuit elements. In order to better engineer the control on the memristance variation we chose to design a system which differentiates its reading and writing inputs by their time duration rather than amplitude. This choice allowed us to generate the impulses directly from the supply voltage of the system (set at 3.3V).

Several single impulses were given to the memristor at the same amplitude (3.3V) while varying their frequency. Since the dynamical behavior of the memristor (when  $R_{\text{on}} < R_{\text{mem}} < R_{\text{off}}$ ) is non-linear with an exponential trend, the memristor was set to  $R_{\text{mem}} = 0.95(R_{\text{on}} + R_{\text{off}})$ , since the memristance changes more for smaller values of  $\phi$  when it is closer to  $R_{\text{on}}$ . This phenomenon can be explained by the length of the conductive nano-filament in the device. When the  $w/D$  ratio is higher, the nano-filament is closer to the border opposite to its origin. In this case smaller values of flux can determine greater changes in the length, compared to when  $w/D$  is close to 0.

From Figure 3.6 it is possible to see the variation of the memristance with respect of the frequency of the impulses. As predicted the variations are lower for high frequencies since the voltage fluxes in the device are lower. A frequency of 1GHz was considered to be acceptable since the memristance in this particular case the memristance changed from a value of  $R_{\text{before}} = 959.5\Omega$  to a resistance value of  $R_{\text{after}} = 961.71\Omega$ . Considering that the memristor will be coupled with the rest of the binary synapse circuitry, the equivalent resistance "seen" by the element will be considerably higher, so we would expect even lower memristive changes to the same kind of input. By these means a perceptron with a synchronized control unit was

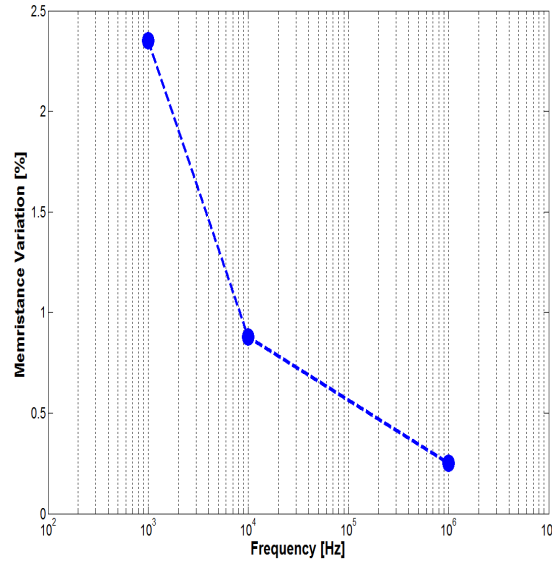


Fig. 3.6 Memristance variation vs. single input frequency.

designed. By programming the control unit with an internal clock with frequency around  $1GHz$  it was possible to vary and identify reading and writing inputs by simply controlling the time period of the various impulses sent to each element. This was done by setting the duration of States 5 and 6 in the changing state machine according to the required  $K$  internal state subdivision of the memristances.

### 3.3.2 Binary Synapse Threshold Characterization

Referring to Figure 3.1 the binarization of the synapse depends on the comparison of the current flowing through the pMOS mirror (reference) and the one flowing through the

return a current with a "high" logical state value, while on the other hand with a "low" one. Since the current flowing through the pMOS mirror is fixed and will never change, the variation between the two logic states is only given by the variation of the memristance on the nMOS mirror branch. By setting  $R_{mem} = (R_{on} + R_{off})/2$  and the voltage given by the voltage supply  $V_{ref} = 3.3V$  and sending a DC voltage with the same amplitude to the memristor, we could verify that the binarization threshold was set at half of the memristive dynamics ( $h_i = 0$ ).

From Figure 3.7 it is possible to see that the response of the system changed to a high logical state (1 in the figure) as soon as the memristance reached half of

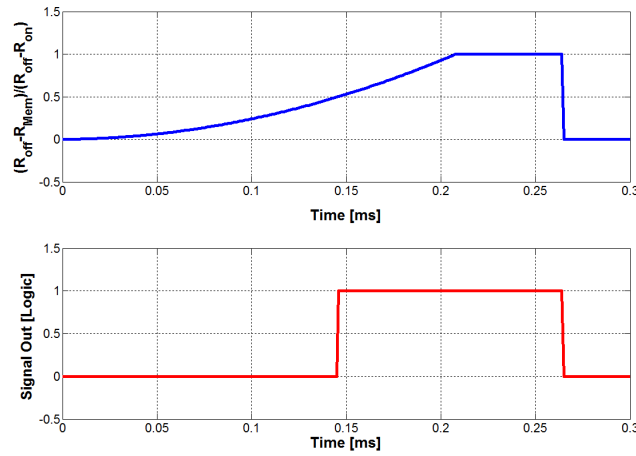


Fig. 3.7 Memristance change vs. logical state output of the binary synapse. In the first graph it is shown the difference between  $R_{\text{off}}$  and  $R_{\text{mem}}$  over  $\Delta R$ . In the second, the output of the system is described as a logical binary response.

the element's activation dynamics. Referring to the SBPI algorithm, described in the previous sections, this kind of response allows the computation of the synaptic weight  $w$  for each element composing the perceptron.

### 3.3.3 Perceptron Learning Efficiency Essays

The perceptron efficiency essays were performed using two different perceptrons, one functioning as *teacher* and the other as *student*. The teacher and the student were built with the same number of synapses. The teacher was built as a completely passive system whose synaptic weights were randomly chosen and fixed, and its purpose was to determine the desired output for each given randomly generated input pattern  $\zeta$ . The student on the other hand evolved and changed the internal states of its synapses according to the SBPI algorithm. With this setting, the goal for the student is learning to reproduce as closely as possible the behaviour of the teacher from a limited set of examples.

While the teacher perceptron is purely computational and used as a tool to interact with the system, the student perceptron model was mounted using PSpice and Simulink simulation tools in order to simulate a model for the circuitry and the control unit of the system respectively. The two tools were set to communicate thanks to the Cadence simulation tool SLPS. Thanks to the tests described in the

previous sections it was possible to set all the parameters of the system in order to operate in a more realistic and precise manner. The number of synapses was arbitrarily set to be  $N = 700$  and the number of internal states per synapse was set to  $K = \sqrt{700}$ . This subdivision does not derive from an internal characteristic of the elements. The number of internal states is given by the precise choice of the time period of the writing inputs sent to the memristive layer since it indirectly affects the total number of patterns that can be acquired by the system. With the chosen value, at each step the resistance variation would be around the 3% of the total resistance span.

The goal of the test was to train the student to reproduce the behaviour of the teacher, changing the parameters used to perform the algorithm. At first a set of  $\alpha N$  training input patterns ( $\zeta_{train}$ ) were sent to the teacher, whose synaptic weights are fixed. The teacher's outputs to each pattern were recorded and used to train the student as desired outputs ( $\sigma_d$ ). Each input pattern was then sent to the student with the respective desired output and its memristances changed according to the rules of the SBPI through "writing" impulses as described in the previous paragraph. After all the patterns in the training set have been presented to the student, a second set of  $\alpha N/5$  of inputs ( $\zeta_{test}$ ) was sent both to the teacher and to the student. In this case the input patterns were sent to the student with "reading" impulses, without changing the synaptic weights. The outputs of the two systems were compared giving the learning efficiency of the system as shown in Figure 3.8. This whole procedure was repeated until the student achieved a perfect pattern classification efficiency, or a predetermined maximum number of presentations of the whole training set was reached. For each presentation the given training input set was never changed, while on the other hand a new test input set was generated from scratch every time.

For this kind of test the parameter that most affects the learning efficiency of the system is the number of patterns used to train the student ( $\alpha N$ ). For this reason a set of  $\alpha$  values was chosen ranging from  $\alpha = 0.01$  to  $\alpha = 0.1$  with intervals of 0.01 and from  $\alpha = 0.5$  to  $\alpha = 1.5$  with intervals of 0.25. For each  $\alpha$  value, 100 training and test procedures were performed. For each essay a  $\theta$  threshold was randomly chosen from a set that ranged from  $\theta = 0.06N$  to  $\theta = 0.36N$ . The maximum number of presentations of the training set to the system was set to 700. The rule R3 probability parameter was set to  $p_s = 0.3$ .

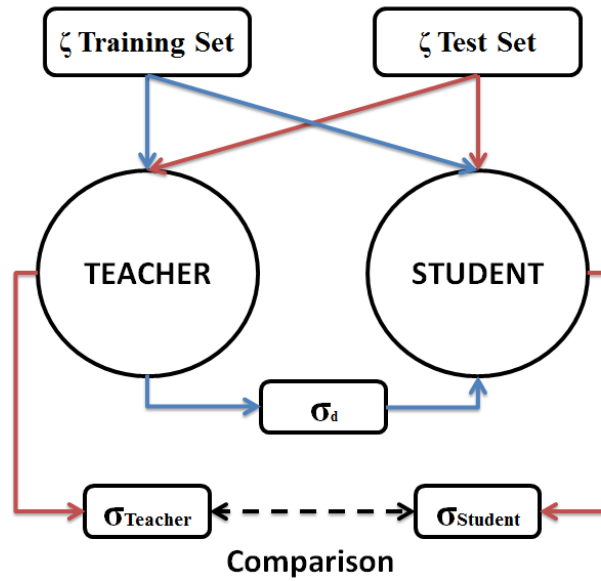


Fig. 3.8 Graphical description of the test and training procedure performed on the system. Two sets of inputs are given to both the student and the teacher. The student has the goal to return the same outputs of the teacher, learning its "implicit" rule. The colours of the arrows state the relation between the inputs and the given outputs.

Figures 3.9 and 3.10 show the results obtained by training the system with different training set sizes. In Figure 3.9 it is possible to see that, as expected, with small values of  $\alpha$  (i.e. in the so-called *under-sampling* regime) the system was not able to apprehend precisely the rule imposed by the teacher, not even in 700 set presentations (as showed in Figure 3.10).

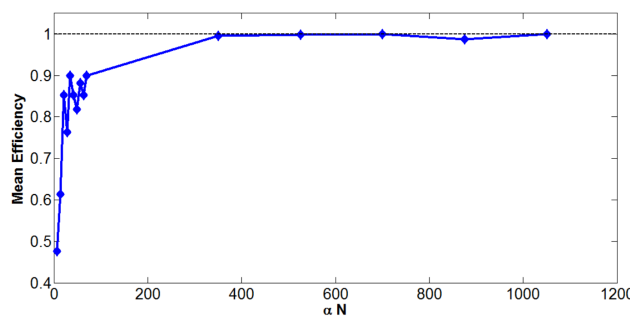


Fig. 3.9 Graph showing  $\alpha$  vs. mean efficiency of each training-test trial. Increasing the size of the training input set it is possible to notice that the efficiency of the SBPI perceptron reaches 100%.

On the other hand, as shown in Figure 3.10, greater values of  $\alpha$  tend to decrease the needed number of presentations in order to reach the maximum efficiency. The

results reported in Figures 3.9 and 3.10 show that if the training input set is too small, when there is not enough information contained in the training data about the rule, the student is only able to approximate the teacher's behaviour, while given enough patterns the learning becomes perfect after just a few presentations per pattern (only one for  $\alpha = 1.25$  or greater).

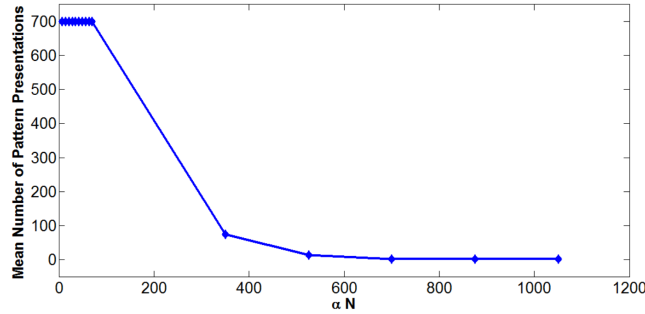


Fig. 3.10 Graph showing  $\alpha$  vs. mean number of presentations needed for each training-test trial. For small  $\alpha$  values there is not enough information in the training set to infer the teacher's rule, and thus the number of presentations per patterns is saturated without reaching efficiency 1; beyond a critical value of  $\alpha$ , however, only a few presentations per pattern are sufficient to achieve perfect learning.

### 3.3.4 Statistical Analysis on the Learning Efficiency of the Memristor-Based SBPI Perceptron

A further analysis has been done on the memristor-based SBPI perceptron regarding its learning efficiency related to the input sets given to the system. The scope of this essay is to understand whether the SBPI perceptron's response is affected on how the rule is posed during the training session changing the parameters of the system.

A simulation model of the SBPI perceptron was built with the possibility to tune the thresholds  $\theta \in \{0.06N, 0.11N, 0.16N, 0.21N, 0.26N, 0.31N, 0.36N\}$  chosen around the optimal value  $0.21N$  provided in [34]. The perceptron for this simulation is built with a number of synapses  $N = 700$ . For each  $\theta$ , 1000 binary random input pattern sets and the correspondent binary desired outputs is created. For each input set the system is trained according to the SBPI and the learning efficiency is computed (as reported in the previous section). After the efficiency is computed all the memristor synapses are reset to the initial conditions  $G_\theta$  (see paragraph 3.1.1)

before beginning the next training session. All the desired outputs in the training sessions are calculated according to four logic rules (proposed in [127]):

- F1*) **Not**: if more than the 50% of the inputs is 1 return  $y = 0$ ;
- F2*) **Buffer**: if more than the 50% of the inputs is 1 return  $y = 1$ ;
- F3*) **And**: if more than 50% of the first 350 inputs and more 50% of the second 350 inputs is 1, return  $y = 1$ ;
- F4*) **Nand**: if more than 50% of the first 350 inputs and more 50% of the second 350 inputs is 1, return  $y = 0$ .

The four logic rules  $F_k (k = 1, \dots, 4)$  are chosen randomly with equiprobability at each training essay. In order to find eventual outliers among the data two different methods are used: the Chauvenet and the Modified Inter-Quartile Range method (MIQR) [128].

Due to the large number of samples, MIQR is preferred to the simple IQR, that in this case could be too restrictive. The acceptance range of the MIQR is between  $4IQR$  and  $4IQR(1 + 0.1\log(n = 10))$ . Considering  $Q1$  and  $Q3$  the first and third quartiles respectively, the data that resides between  $Q1 - 1.5IQR(1 + 0.1\log(n = 10))$  and the acceptance range, and between  $Q3 + 1.5IQR(1 + 0.1\log(n = 10))$  and the acceptance range are considered mild outliers. All the rest are considered extreme outliers.

On the other hand, Chauvenet developed a method to detect outliers through the belief that in any kind of observation, one out of two replications of the same experiment is observed with a measurement mistake. The probability to mistake the measurement is to be considered approximately equal to  $p \approx 0.5/n$ , where  $n$  is the number of observations. Probability  $p$  can be used to mark off the two tails of the data distribution, where the experimental results should be considered outliers. According to the number of the observation, MIQR method should be less strict, while Chauvenet's strictness is less dependent from the size of the set of data. In both cases no outliers were detected from the data.

By evaluating Figures 3.11 and 3.12 it can be seen that the data is not to be considered normally distributed. Through the evaluation of the histograms (see Figures 3.11 and 3.12) it can be noticed a bimodal shape, entailing the presence of a mixture. In other words the data distribution might be obtained by the sum of two or

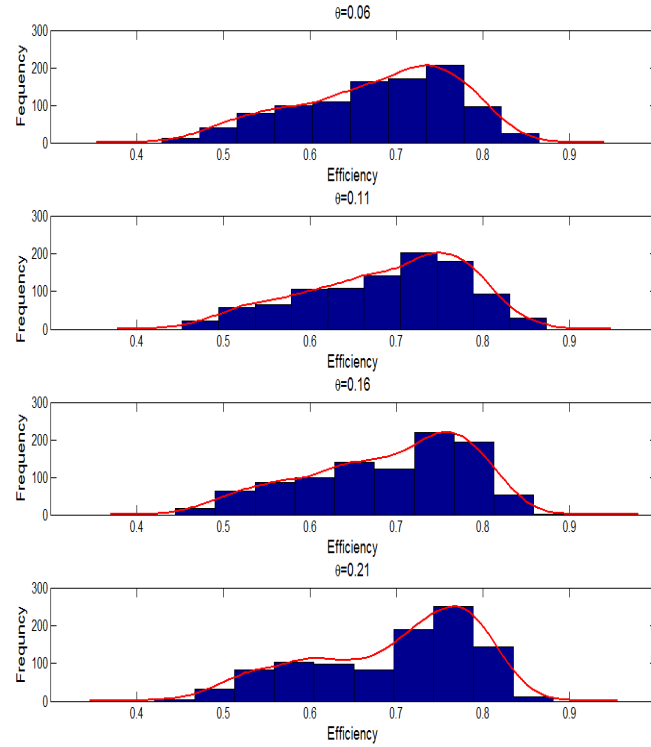


Fig. 3.11 Frequency histogram for  $\theta = 0.06N$ ,  $\theta = 0.11N$ ,  $\theta = 0.16N$  and  $\theta = 0.21N$  with overlapped kernel curve (red line).

more normal distributions with different characteristics. In order to better understand this phenomenon, for each data set (and for each value of  $\theta$ ), a frequency histogram is plotted overlapped with a kernel. The kernel has the scope to envelope the data through a low-pass filter in order to obtain the curve which can better represent the distributions. Figures 3.11 and 3.12 show the frequency histograms for each chosen  $\theta$  value with the computed kernel overlapped.

Observing the various kernels the mixture assumption might be considered true. In order to prove this a  $\chi^2$  analysis is performed for each distribution. In some cases the kernels can be considered to be composed of two curves in other cases ( $\theta = 0.11N$ ,  $\theta = 0.16N$  and  $\theta = 0.21N$ ) whereas there are cases in which the kernel can be considered composed of three curves. In Table 3.1 are reported the obtained values of this analysis.

The variables shown in Table 3.1 are the results on the  $\chi^2$  analysis for each kernel. Furthermore,  $\mu$  are the mean values of the distributions composing the kernel and  $\sigma$  are the respective standard deviations,  $\chi^2_{upper}$  and  $\chi^2_{lower}$  are the upper and

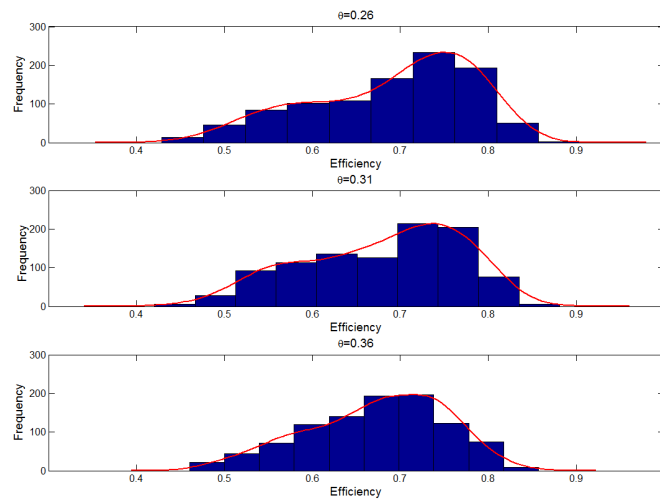


Fig. 3.12 Frequency histogram for  $\theta = 0.26N$ ,  $\theta = 0.31N$  and  $\theta = 0.36N$  with overlapped kernel curve (red line).

lower boundaries of the  $\chi^2$  distribution (with  $\alpha = 0.05$ ) and the given degrees of freedom ( $DOF$ ). Finally,  $\chi^2_{experim}$  are the values obtained of the  $\chi^2$  analysis of the experimental data of the given distributions and  $\%_1$ ,  $\%_2$ , and  $\%_3$  are the coverage percentages of the normal distributions forming the curve.

Table 3.1 Results of the  $\chi^2$  Analysis for Each Kernel

$\theta$	0.06	0.11	0.16	0.21	0.26	0.31	0.36
$\mu_1$	0.58	0.54	0.58	0.54	0.59	0.58	0.59
$\mu_2$	0.73	0.68	0.66	0.60	0.75	0.73	0.70
$\mu_3$	-	0.75	0.80	0.76	-	-	-
$\sigma_1$	0.05	0.05	0.03	0.06	0.05	0.07	0.05
$\sigma_2$	0.03	0.04	0.05	0.02	0.03	0.04	0.02
$\sigma_3$	-	0.02	0.05	0.01	-	-	-
$\%_1$	0.18	0.09	0.04	0.12	0.26	0.24	0.20
$\%_2$	0.82	0.34	0.06	0.19	0.74	0.76	0.80
$\%_3$	-	0.55	0.90	0.69	-	-	-
$\chi_{upper}^2$	32	32	33	30	32	32	32
$\chi_{lower}^2$	8	8	9	8	8	8	8
$\chi_{experim}^2$	30	24	15	22	27	31	27
$DOF$	18	18	19	17	18	18	18

From the results in the table follows that the kernels are to be assumed as mixtures of two or three normal distributions. As a consequence the set input should be considered as formed by two or three groups of data suffering from the effect of one factor in systematically different ways, or suffering each one the effects of two or three different factors. This could be a possible cause of the actual formation of the mixture of normal distribution observed.

From the point of view of the SBPI perceptron it has been possible to identify the causes that led to a bi-modal distribution of the learning efficiency. Since the patterns are presented to the single layer of memristive binary synapses are randomly chosen, the respective sets could or could not be well selected. As a matter of fact the memristor based perceptron presented and described in this chapter presents a higher learning efficiency when the "true states" present in the input pattern set are higher than the "false" ones in a given range. The best true/false ratio was found to be around 60% true and 40% false for all the chosen  $\theta$  threshold values. The SBPI perceptron must be able to recognize true facts rather than patterns which mathematically are excluded from the sub-set regarding the given rule.

As a matter of fact only false patterns would set all the memristors in a low state, avoiding the flow of current through the perceptron (i.e.  $y = 0$ ). On the other hand only positive patterns would set all the memristors in a high state which would be

too sensible. Numerical simulations has allowed to make clear how the performance of the SBPI algorithm are strongly influenced by the input training patterns.

## Chapter 4

# Memristive Systems for Clinical Assessment of Chronic Wounds

In chapters 2 and 3 it has been introduced and presented a thorough analysis of memristive devices and systems proving their computing capabilities and their theoretical implementation. From the knowledge gained it is possible to design systems that have real life utility for a specific application. In this chapter it will be introduced a system capable of gathering images through a digital camera and analyze them detecting specific objects and taking measurements through an algorithm named *cellular automaton* [31]. Moreover it will be demonstrated how this system is capable, with additional light sources, to return 3-dimensional information from the detected objects. The possible applications for such system are many that range from industry to defence. In our particular case the device here introduced has been built, thanks to the cooperation of the *Associazione Italiana Ulcere Cutanee (AIUC)* and its former president and founder Dr. Elia Ricci, for the remote and automatic detection and assessment of *chronic wounds*.

In this chapter, after a brief overview on the clinical aspects regarding chronic wounds, a deep description of the developed system will be provided. It will be introduced the cellular automaton as a powerful computational bio-inspired algorithm and how it has been implemented in the proposed system. Moreover it will be provided a description and analysis of the design of the device that was developed as will be provided the results of the pre-clinical trials performed on more than 200 patients, proving the classification and processing capabilities of the system.

## 4.1 Clinical Overview

Chronic wounds are wounds that have failed to proceed through an orderly and timely reparative process to produce anatomic and functional integrity over a period of three months [129]. Chronic wounds are traditionally divided into three major groups: venous leg ulcers, diabetic foot ulcers, and pressure ulcers. In developed countries, 1-2% of the population will experience a chronic wound in their lifetime [130]. It is expected that the number of chronic wounds will increase worldwide due to an increase in lifestyle diseases, such as diabetes, obesity, and cardiovascular diseases.

In the United States, chronic wounds affect 5.7 million people, costing an estimated 20 billion dollars annually, and there has been an increase in hospital stays for pressure ulcers by approximately 80% from 1993 to 2006 [131].

The lack of appropriate clinical assessments of patients with chronic wounds has often led to longer treatment periods and improper or ineffective care [131–133]. Therefore, it is essential to accurately and frequently monitor disease progression in order to give physicians a chance to optimize therapy. Today's treatment methodology consists of weekly examinations where the doctor evaluates the granulation tissue and the size, depth, colour of the wound. The most common methods used by clinicians are mainly based on manual approaches for estimation of the area of the wound and, therefore, suffer from high inaccuracy. These methods may be divided into techniques that measure area and perimeter, and techniques that measure volumetric information. The first method uses a ruler (or a caliper) to measure the major and minor axes of the lesion. Based on these two measurements, the area of the wound is estimated as a rectangle or as an ellipse. In either model, the decision of the major axes is subjective and has an impact on the variability of the method. In the second approach a transparent film is placed over the wound and the outline is traced with a permanent marker. Afterwards, the film is placed on a metric grid and the area is measured by counting the number of squared millimetres contained within the outline. This process is also prone to human error. Several studies have shown that the predominant factor contributing to measurement errors is the incorrect and inconsistent identification of the wound border due to poor definition or subjectivity of the process. In addition, the number of partial squares on the grid inside the outline and the thickness of the marker may cause some inaccuracy.

All the described techniques require direct contact with the wound to measure or estimate its area. Some other techniques have been evaluated, including digital planimetry, photography, stereophotogrammetry, digital videometry, and laser scanning. All these techniques have displayed limits due to subjective interpretation and changing environmental conditions.

As it will be shown in the following sections of this chapter the system here presented is able to detect wounds in pictures taken with digital photography devices and as afore mentioned measure and gather 3D information from them that are useful to the physician for the correct diagnosis, posology and classification of the wound [134]. Thus, direct contact with the wound is not necessary. By using this approach, we believe that the quality of life for patients could be improved and that physicians would be able to treat more patients due to robust digital support.

## **4.2 Cellular Automaton and Discrete Time Cellular Neural Networks**

A cellular automaton (CA) is a discrete time-space model used to study computability theory [31]. It was first theorised by Stanislaw Ulham and John von Neumann in the late 1940s and later defined by Stephen Wolfram. Cellular neural networks took inspiration from CAs when were developed. The assimilation between the two is possible since memristive CAs are able to perform similar functions due to their dynamic non-linear structure defined by coupling identical simple dynamical elements named cells [102]. Since the 2008 first nanoscale memristor industrial fabrication [2], the impact of CAs in the scientific community was enhanced due to the fact that physical memristive elements could be implemented in systems performing such algorithm.

As mentioned above CAs can be used in different fields of computational theory. Mostly they are exploited for image processing and through them it is possible to model several operators (example in Figure 4.1). Moreover they are proved to be a powerful tool for simulating and predicting local phenomena: for example it is used to predict DNA filament movement or the mitigation of sound in buildings.

The CA consist in a regular grid of cells, each one with a finite number of states. The grid must be of finite dimensions. The states of the cells composing the grid at

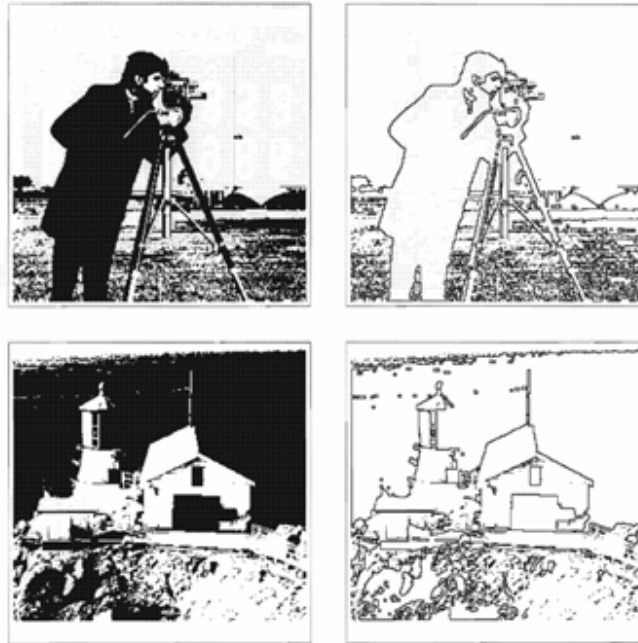


Fig. 4.1 Two examples of CA used for image processing. In both pictures the CA was used for detecting the edges of the subjects. This is one example of image processing operand that can be rendered through CAs.

time instant  $t=0$  are the initial states of the automaton and are arbitrarily set. At each time point the combination of the cell's states forms a generation. The generational evolution occurs at specific discrete time instants and it depends on the state of the previous generation. More precisely each cell changes its state from a generation to another depending on its previous state and/or on the states of the surrounding cells. The possible number of rules that the system can implement strongly depends on surrounding radius that effects the change of the given cell. Supposing to have an array of  $n$  cells and the generational evolution of a given cell of the system is given by its actual state (1 or 0) and the state of the two adherent cells then there are  $2^3 = 8$  possible combinations that lead to  $2^8$  possible rules.

From Wolfram's definition a system must present the following characteristics in order to be defined a CA [31]:

1. there must be a spatial representation of the involved entities;
2. uniformity: or in other words all the entities must have the same characteristics and must be identical other than interchangeable;

3. locality: each entity changes its state from a generation to the other taking into account the states of the entities within a given surrounding radius.

Still, from Wolfram's theory, CAs can be described as a fourfold  $\langle d, Q, N_n, f \rangle$  where

1.  $d$  is the dimension of the CA;
2.  $Q$  is the space of the states which the cells can assume;
3.  $N_n$  is the neighborhood index which describes the region of influence of the other cells for the given cell's state change;
4.  $f$  is the generation transition function which describes the state change of each cell at each time instant  $t = \tau + nT$ , and must be a function of a cell neighborhood described by parameter  $N_n$ .

Furthermore, as described in details in [41], memristive CNNs, in particular *discrete time cellular neural networks* (DTCNNs), can be assimilated to memristive CAs. As reported Itoh and Chua first described an implementation of a cellular automaton with inputs using memristors. the dynamics of their system were given by

$$y_{i,j}(nT) = M \left( \sum_{g,l \in (-1,0,1)} a_{g,l} y_{i+g,j+l}((n-1)T) + \sum_{g,l \in (-1,0,1)} b_{g,l} u_{i+g,j+l}((n-1)T) + \Delta T \right) \quad (4.1)$$

where  $y$  is the output or in other words the state of the cell and  $u$  are the external inputs of the system.  $T$  is the time period in which there is a new input and, therefore, a new generation change in the system, while  $\Delta t$  represents the charge accumulation in the memristor during the previous generations.  $a_{g,l}$  and  $b_{g,l}$  are elements of two distinct matrices  $A$  and  $B$  which both have size  $G \times L$ .  $A$  is the template that contains the weights given to the neighbour cell states (feed-forward) and  $B$  contains the weights given to the external input (feed-back).  $A$  and  $B$  are the necessary sufficient elements, which describe the imposed rules to the memristor CA. Function  $M(\cdot)$  denotes the memristance change function. The circuit implementation of Itoh and Chua for a memristive CA is shown in Figure 4.2.

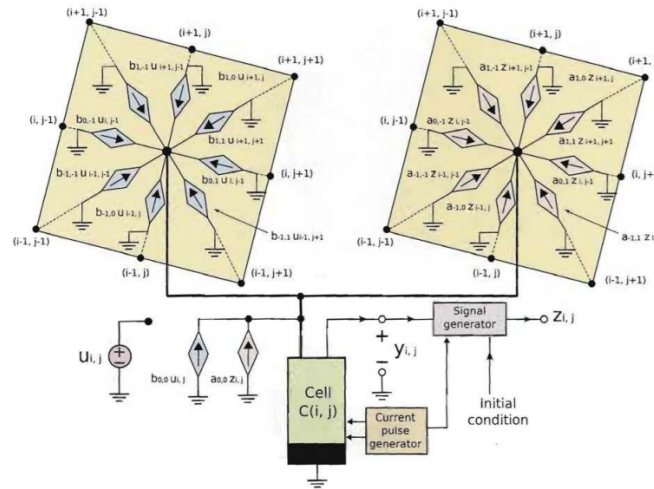


Fig. 4.2 In figure the theoretical circuit memristor implementation for a memristive CA taken from [41]. From their model it is possible to see that the inputs to the cell are given through a signal generator. The inputs can be of two kinds: internal (the state of the surrounding cells) and external (the inputs that come from the external environment), in figure represented with pink and blue signal generators respectively.

### 4.2.1 Cellular Automata and Stochastic Belief Propagation Inspired Perceptron Equivalence

Previously in this section, was introduced the cellular automata by which Itoh and Chua managed by the memristances of each cell [41]. The CA that is presented hereafter exploits the BPI algorithm (described in paragraph 3.1.1). Initially for the first simulations, the cells have been assimilated with mathematical models of memristors (see [42] and [21] for further details, introduced in chapters 2 and 3 respectively). Though the SBPI has been deeply described in the previous chapter, in this paragraph will be briefly reported once more the general rules for the sake of clarity with the equivalence here provided.

The SBPI algorithm [34], as mentioned before works throughout a single layer of cells called synapses. Each synapse returns a binary value, which depends on the actual memristance values of each cell. For the SBPI, it is necessary to compute the "normalized" memristance of each cell  $h_i \in [-1, 1]$  subdivided in  $k$  discrete steps. The highest possible resistance of the single element ( $R_{off}$ ) corresponds to  $h_i = -1$ , and viceversa the lowest possible value ( $R_{on}$ ) corresponds to  $h_i = 1$ . All the normalized memristances are to be commuted into synaptic weights as

$w_i = \frac{1}{2}(\text{sign}(h_i) + 1)$ , where  $\text{sign}(\cdot)$  represents a signum function. According on the given rule intended to be learned by the system, it is necessary to set a threshold parameter  $\theta \in [0, N]$  where  $N$  is the number of cells composing the array. Given a set of binary input patterns  $\zeta_i$ , and for each pattern a desired output  $\sigma_d$ , which as said is also binary, that follows the implemented rule it is possible to calculate the total current flowing from the cells as  $I = \sum_{i=1}^N w_i \zeta_i$ . Once computed the "stability parameter" as  $\Delta = (2\sigma_d - 1)(I - \theta)$ , the evolutionary change may be described by the three following rules:

- R1) if  $\Delta \geq 0$ , then all  $w_i^\tau = w_i^{(\tau+1)}$ ;
- R2) if  $\Delta < 0$ , then all  $h_i^{\tau+1} = h_i^\tau + 2\zeta_i^\tau(2\sigma^\tau - 1)$ ;
- R3) with probability  $p_s \in [0, 1]$ , if  $w_i^\tau > 0$  then  $h_i^{\tau+1} = h_i^\tau - 2\zeta_i^\tau$ ; else  $h_i^{\tau+1} = h_i^\tau + 2\zeta_i^\tau$ .

In order to find an equivalence between the CA described in equation (4.1) and a CA built using the SBPI, several arrangements have to be made on the parameters of the algorithm. The probability  $p_s$  was set to zero in order to have total control of the generation changes of the states of the cells composing the system. The number of states  $k$  was set equal to 2 in order to have  $h_i \in \{-1, 1\}$  significantly cutting down the computational complexity. Combining R1 and R2 with the definition of stability parameter  $\Delta$  function  $J(\cdot)$  can be obtained, which describes the evolution dynamics of the cells:

$$J_i(\zeta, \sigma_d) = h_i^{\tau+1} = h_i^\tau + 2\zeta_i^\tau \frac{(\text{sign}(\Delta) - 1)}{2\text{sign}(I - \theta)} \quad (4.2)$$

$\tau$  in R1, R2, R3 and  $J(\cdot)$  denotes the time point of a given generational change. As it is possible to see from equation (4.2),  $J(\cdot)$  is the function that states the weights given to the inputs ( $\zeta_i$  and  $\sigma_d$ ).

In our BPI-CA the actual cells that evolve during the process are posed in three memristor-composed matrices with the same size of the analyzed image ( $H_r, H_g$  and  $H_b$ ). This is so since differently from normal CA use (grey tone image processing and filtering), the BPI-CA can be used to elaborate full colour map images (RGB). As an initial condition, the memristive elements were all set to the  $R_{off}$  state ( $h_{H_r, H_g, H_b|i, j} = -1$ ). The iterations of the system do not occur in the single matrix but crosswise in the three memristive blocks, taking into account the spacial correspondence of the cells as shown in figure 4.3. The neighborhood in which the region of influence is

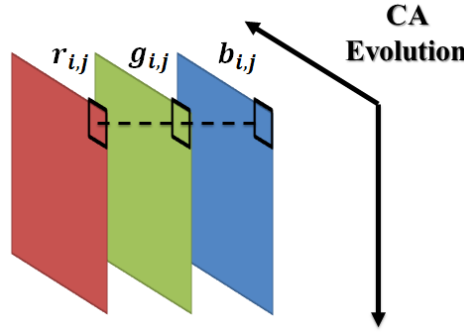


Fig. 4.3 Brief depiction of the crosswise CA. All three matrices ( $R$ ,  $G$ , and  $B$ ) are divided in cells which are compared through the equations in  $G(r_{i,j}, g_{i,j}, b_{i,j})$ . The results of the system give the inputs to the CA, which evolves horizontally and vertically from the original neighborhood array until it covers the whole image.

described is composed by the triplets of cells that correspond to the same position in the three memristive matrices ( $N_n = 3$ ). Considering equation (4.1), it is possible to rewrite equation (4.2) in the same form.

$$\begin{aligned}
 h_{x|i,j}^{\tau+1} &= M \left( \sum_{x=1}^{N_n} a_{x|i,j} h_{x|i,j}^{\tau} + \sum_{x=1}^{N_n} \zeta_{x|i,j} \left( 2 \frac{(\text{sign}(\Delta) - 1)}{2 \text{sign}(I - \theta)} \right) \right) \\
 &= M \left( \sum_{x=1}^{N_n} a_{x|i,j} h_{x|i,j}^{\tau} + \sum_{x=1}^{N_n} J_{x|i,j}(\zeta, \sigma_d) + \Delta t \right)
 \end{aligned} \tag{4.3}$$

In equation (4.3)<sup>1</sup>, the threshold parameter was set to  $\theta = 2.5$ . All the generation changes in the system must be input-based, so in the case of our CA performing the BPI, the matrix that gives the weights to the surrounding states is  $A = [0 \ 1 \ 0]$ . By inserting  $A$  in equation (4.3) it is possible to obtain directly equation (4.2). It is possible to notice that the evolutionary algorithms described by equations (4.1) and (4.3) present the same properties of a CA as described by Wolfram, thus are considered to be equivalent.

<sup>1</sup>In equation (4.3) the cell states are noted as  $h_{i,j}$  instead of  $y_{i,j}$  since for the SBPI algorithm the possible states are discrete and properly fixed. On the other hand, in the algorithm by Itoh and Chua the state of the single cell coincides with the actual internal state of the memristive element.

## 4.2.2 Element Detection in an RGB Image Trough Memristive SBPI-CA

The SBPI-CA can be used as afore mentioned in the processing of generic RGB images. The scope for which ha been performed in this work is the detection of particular elements from digital images. In order to obtain a good identification of a specific element depicted in a generic coloured image, it is necessary to understand the properties of the image segment that shows the element itself. It is necessary to understand that the BPI-CA was performed on pictures taken with generic digital optic devices such as the one shown in Figure 4.5A. Every element of a picture has a specific colour combinations that diverges from the rest of the background. Considering a generic *RGB* image, it is possible to decompose its three colour maps. Considering the single elements of *R*, *G*, and *B* it is possible to find mathematical relations between the three, here described as  $G(r_{i,j}, g_{i,j}, b_{i,j})$ , in order to distinguish the patterns that are only proper of the areas of the depicted detail that is intended to be isolated.  $G(\cdot)$  is a system of equations that take inspiration from the "green screen" detection techniques and its equations vary according to different factors relating the image, i.e. the exposure of the picture, but can be adjusted through digital image filters that act directly on the brightness histogram. In other words  $G(\cdot)$  for the chosen element is defined in a particular subspace  $\Omega$  so that we have  $\{G(r_{i,j}, g_{i,j}, b_{i,j}) : (r_{i,j}, g_{i,j}, b_{i,j}) \in \Omega, \Omega \in RGB\}$  as shown in the figurative example shown in Figure 4.4.

All the elements of the *RGB* matrices of the picture (i.e. Figure 4.5A) were analyzed according to these functions and the solutions of the equations gave the corresponding value range in which all three must reside in order to identify the particular element obtaining  $G(r_{i,j}, g_{i,j}, b_{i,j}) = \{\zeta_{r|i,j}, \zeta_{g|i,j}, \zeta_{b|i,j}\}$ . In other words, the colours that identify the object are singular and are not repeated in other areas of the picture external to the object itself. As mentioned before the BPI-CA does not perform its iterations singularly in each matrix, but it evolves crosswise between *R*, *G*, and *B* as shown in Figure 4.5.

Each element of the three matrices was considered as an input cell. The environmental neighborhood of the generational evolution of the cells is given by the spatial relation of the elements of the three matrices. The SBPI other than cellular external inputs needs the according desired output in order to arrange the eventual

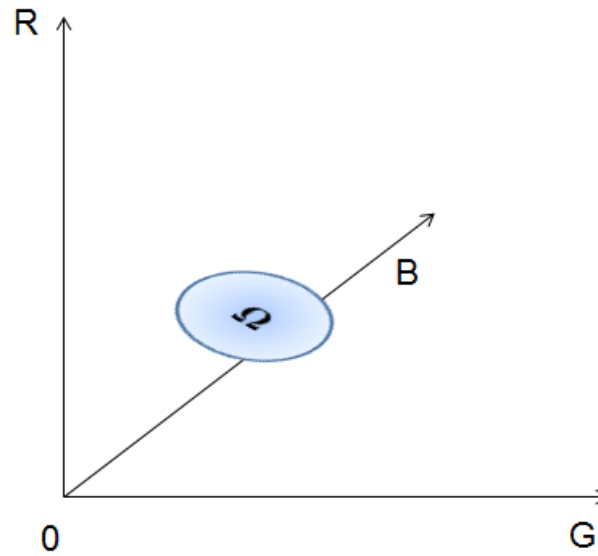


Fig. 4.4 Generic subspace  $\Omega$  in the RGB space. Considering a generic RGB image, only several pixels are depicting a given subject in the figure. Those pixels have particular values that can be related through each other through the relations described by  $G(r_{i,j}, g_{i,j}, b_{i,j})$ .

generation change of the states. By these means the rule imposed to the CA can be easily described by Table 4.1.

Table 4.1 SBPI-CA Particular colour detection rule

$\zeta_{r i,j}$	$\zeta_{g i,j}$	$\zeta_{b i,j}$	$\sigma_{d i,j}$
0	0	0	0
0	0	1	0
0	1	0	0
0	1	1	0
1	0	0	0
1	0	1	0
1	1	0	0
1	1	1	1

Once all the iterations are over and all the cells in the three  $H$  matrices have been set according to the algorithm, matrix  $S$  was created re-presenting all the inputs to the cells. In this second computational phase, the cells do not change their states

but retain memory of the CA interactions.  $S$  has the same size of the image and its elements are the outputs of the SBPI calculated as:

$$s_{i,j} = \Theta(w_{H_r|i,j}\zeta_{r|i,j} + w_{H_g|i,j}\zeta_{g|i,j} + w_{H_b|i,j}\zeta_{b|i,j} - \theta). \quad (4.4)$$

$\Theta(\cdot)$  is the Heaveside function,  $w_{H|i,j}$  are the synaptic weights computed from the cells composing  $H_r, H_g$  and  $H_b$ , and  $\theta$  is the threshold parameter.

The resulting contents of  $S$  matrix corresponds to a bit-wise image representing the mask of the element since the white pixels ( $s_{i,j} = 1$ ) are spatially corresponding to the ones in the native image in which the object is present as shown in Figure 4.5B. It is possible to notice that in the particular case of the figure chosen as an example the subject has two very close objects with the same colour scheme and that the system was able to exclude the rest of the background of the picture, detecting in fact, both elements. The SBPI-CA is able to precisely detect the contours of a single chosen element. The results depend on the conditions present when the picture was taken. All images used to prove the reliability of the method were randomly selected from several databases and all have variable features, i.e. use of the flash when capturing the picture and degree of focus. Although this variability could lead to aleatory results, applying well known image filtering solutions (same filters for each picture examined), the system was able to detect several elements with the same high precision for all pictures.

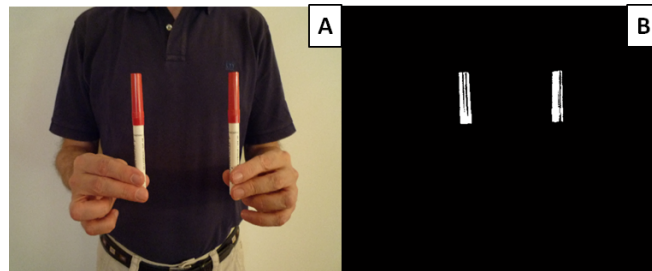


Fig. 4.5 Results of the CA iterations on a generic digital image. (a) Picture representing a subject holding two objects of similar colour which are intended to be identified and isolated from the picture. (b) The mask image given by matrix  $S$ , which is composed of the binary outputs of the three memristive matrices  $H_{r,g,b}$ .

### **4.3 System Based on SBPI-CA for Chronic Wound Detection, Follow-Up and Assessment**

In section 4.1 it has been described the problem related to chronic wounds. As afore reported this syndrome is considered one of the most dangerous since it mostly affects the part of the world population which is more vulnerable: the elderly. The people who suffer from these particular kind of wounds also suffer from more serious and debilitating diseases such as vasculopathy and diabetes. Moreover the wounds need a large amount of time to heal and have to be constantly assessed and medicated by the physician and the caretakers. If the wound is not properly evaluated and medicated through time the patients risk to lose the affected limb, or in the worst cases they can die.

To assess the wounds and to subsequently evaluate the healing status of a patient, the physician must measure the sore in means of area and volume. Both variables are of high importance since in certain cases the decrease of the area of the wound is decreasing but its depth is increasing, violating deeper tissues. This fact increases the probability of an amputation. In addition the wound is also visually analyzed in order to detect the status of the tissues that compose the ulcer.

All these measurements are taken in the majority of the cases by hand with a high level of inaccuracy and most of all with methods that are highly invasive. For example the depth of the ulcer in some cases is measured through a cotton tip which is inserted in the open skin, provoking a severe pain to the patients. Though the great problems and suffering given to the patients these measures are of primary importance since these values have the scope to identify and classify the ulcer by means of the *Wound Bed Preparation Score* (WBP) [135].

The WBP score is an alpha-numeric codification system which is recognized and used by the majority of physicians which states the actual status of the wound. Tables 4.2 and 4.3 describe the actual parameters by which this score is given depending on the various cases.

As it is possible to read from the tables also the amount of exudate is a clear indication of how the cure is proceeding. Obviously there are many other factors that have to be taken into account when treating a chronic wound and all have their importance when a physician has to formulate the correct diagnosis and posology.

Table 4.2 WBP letter code taken from [135]

Wound bed appearance score	Granulation tissue	Fibrinous tissue	Eschar
A	100%	Absence	Absence
B	50 – 100%	Presence	Absence
C	< 50%	Presence	Absence
D	Any amount	Presence	Presence

Table 4.3 WBP number code taken from [135]

Wound exu- date score	Extent of control	Exudate amount	Dressing Require- ment
1	Full	None/ mini- mal	No absorptive dressings required. If clinically feasible, dressings can remain for up to 1 week
2	Partial	Moderate amount	Dressing changes required every 2 to 3 days
3	Uncontrolled	Very exuda- tive wound	Absorptive dressings changes required at least daily

The problem related to ulcers is also the difficulty of collecting appropriate data regarding a wound or a patient. As afore mentioned the most accurate measurements are taken with very invasive and painful methods, on the other hand non-invasive solutions are fairly inaccurate. One of the most recent systems developed for this particular use us able to measure the entity of the sore from a digital picture taken with a dedicated device, but the actual recognition of the ulcer in the image is done by hand and the operator has to trace the borders on the screen.

the system here presented has the scope to overcome the problems related to ulcer assessment and detection. In the following paragraphs will described in details the system and its efficacy will be proven through the results obtained from pre-clinical trials done on more than 200 patients.

### 4.3.1 System Design

The system we propose is made of two distinct components: a device with the appropriate elements for the data collection and storage (here denoted as *hardware*), and a *software* that implements the SBPI-CA algorithm afore described for the analysis

following data from the patient:

1. the wound's surface;
2. the wound's depth;
3. the wound's granulation, or in other words the tissue composition of the sore.

Regarding the hardware, the device was built with the following components:

1. one FPGA board which includes:
  - (a) 12 white LEDs with a colour temperature of 2700K, singularly controlled with dimming through PWM signals;
  - (b) one PING distance sensor with a proximity range from 1 to 30mm and a resolution of 50 $\mu$ m;
  - (c) one temperature and humidity sensor for the correct reading of the PING;
  - (d) the driver for the LEDs;

- (e) one  $\mu$ -processor for the control of the drivers, obtained with an *Arduino NANO* board;
2. one supporting mobile device (smartphone) of which were exploited the  $\mu$ -processor for synchronization of the elements on the FPGA, the camera (8Mpx), the screen for the device's pointing and the memory capability for the data;
3. one external battery for the supply voltage given to the LEDs and its drivers, other than the sensors and the Arduino board (16Wh charge).

The FPGA board and the supporting device are connected through USB cable. The smartphone, as mentioned in the element list, is used for the control of the whole system providing a simple interface for pointing the camera and sends the commands to the Arduino NANO board for the synchronization of the elements. Figure 4.6 shows the device with its components.

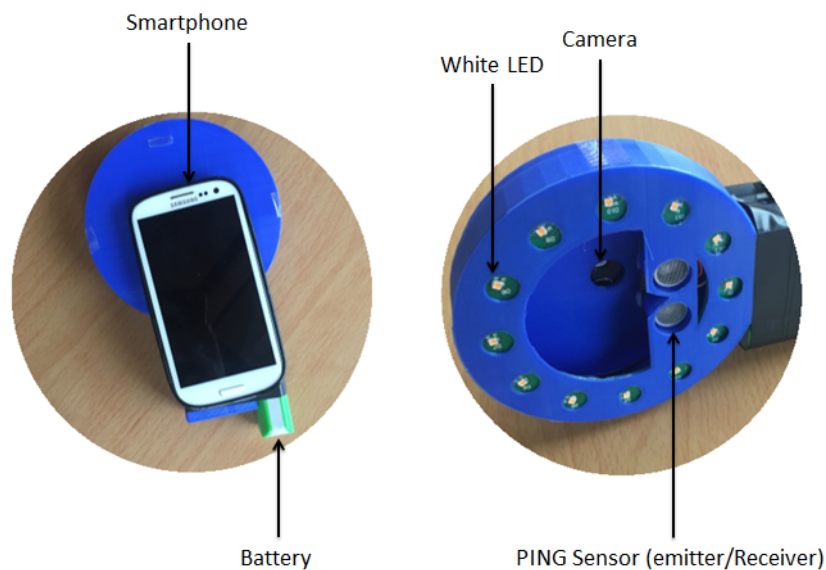


Fig. 4.6 The picture shows the *hardware* components of the device for the data collection regarding the ulcers. In the picture are indicated all the principal components. The case of the device was realized through a 3D printer. The temperature and humidity sensor is not shown since is inside the case. Next to the battery, in the handle, is located the Arduino NANO board. The FPGA is inside the case, which is attached to the smartphone through a custom cover.

The purpose of the device, as mentioned, is to gather the raw data from the wound. The FPGA on the other hand is designed have the LEDs disposed, equally spaced, on the borders of a circular "crown" with a diameter of 10cm. The crown is posed on the smartphone in order to have the camera exactly in the center of the LED circle. The distance sensor is positioned next to the camera in order to measure with the greatest possible precision the distance between the camera itself and the wound. The system is designed to take a set of pictures with different light sources generating shades on the patient's skin. More precisely one picture of the wound is taken for every light source turned on in sequence plus one with all the LED emitting light.

All the pictures are then stored in the mobile device which through a software, implementing the SBPI-CA described in section 4.2, is able to identify the wound, calculate its area, its depth and its granulation. All the data regarding the distance is transmitted through micro-USB cable to the smartphone. Regarding the tissue classification, a set of wound images have been taken from patients of different races in order to establish the colour differences between various kinds of skin and the tissues composing the wounds. Through these pictures it was possible to create a digital catalogue of the different colours of the tissues for the granulation analysis. from these pictures it was possible to identify a pattern that is proper of each wound and the same pattern was used to identify the wound from the data collected from the device.

At first it was necessary to size the pixels of the image. their sizes depends on the distance of the camera from the skin surface, which is the reference for the measurements. With a blue dot (i.e. a blue point on a white background with known size) it was possible to calculate the *focal curve* of the camera and its optics. the focal curve is calculated taking at least five pictures of the blue dot at different known distances (measured with the PING distance sensor). Analyzing the pictures identifying the blue dot (through the SBPI-CA choosing accordingly the  $\zeta_{r,g,b} - \sigma_d$  values) it is possible to create a pixel mask for each distance. The relationship between the number of pixels composing the mask, divided by the surface in  $mm^2$  of the blue dot, and the distance of the camera of each picture can be represented in the curve  $D(\cdot)$ .  $D(\cdot)$  is different for each camera and is also dependant from its optics. If the camera of the device is changed it is necessary to build a new curve.

Once the pictures of the wound have been taken, the algorithm starts analyzing the one with all the LEDs switched on. This picture (hereafter will be named as *principal*) is considered the most important for the almost complete absence of shades. This picture has the scope to function as reference for the next measurements performed on the other taken images. As afore mentioned it has been established a pattern of identification of the lesion on any kind of skin. This pattern derives from the study of a random set of pre-taken digital pictures of wounds on subjects that have different skin pigmentation. Through the use of this recognition pattern, the system is able to recognize the *seeds* or in other words the values  $\zeta_{r,g,b}$ , proper of the wound for each image and to associate them with the desired output  $\sigma_d$ .

It is proven from the pre-taken set of images that a generic ulcer is characterized by high derivative (both vertical and horizontal) values when decomposing the principal image in its three colour matrices  $R$ ,  $G$  and  $B$ . The skin of a generic patient on the other hand is always uniform in all three cases. Moreover, the greatest differential values are found in the  $B$  and  $G$  matrices. Once the derivatives are performed three binary masks are obtained. The binarization of the masks is obtained applying a threshold to the resulting pixel values, this threshold was set (considering a black and white image that ranges from 0 to 1) to 0.75 so that only the highest differential values are taken into account. The three masks are then added and subtracted as  $B + G - R$  and the resulting image is binarized again. The resulting pixels over threshold (with a value of 1) are then used as markers to identify the colour seeds ( $\zeta_{r,g,b}$ ) and related with a desired output  $\sigma_d = 1$ .

The SBPI-CA algorithm is then performed on the image with the crosswise iteration shown in Figure 4.3, obtaining the resulting  $s_{i,j}$  matrix introduced in equation (4.4). Other two operations are then performed on the same image in order to exclude with greater precision the *false positives* or in other words the elements of the image that have been classified as wound, but are parts of the background or of the skin. This operations have also the scope to identify the peri-wound, which is the skin borders of the ulcer that have the characteristics of sane epidermis but are to be considered s part of the sore. The first operation is a second classification operation done using the  $\zeta_{r,g,b}$ , values used for the ulcer detection. All the supra-threshold elements of  $s$  are analyzed with a structure  $C$  which has size  $5 \times 5 \times 3$ . The central element of  $C$  corresponds to the analyzed pixel.  $C$  contains the weights given to the surrounding elements as:

$$C = \begin{bmatrix} 1 & 1 & 1 & 1 & 1 \\ 1 & 0.5 & 0.5 & 0.5 & 1 \\ 1 & 0.5 & 0 & 0.5 & 1 \\ 1 & 0.5 & 0.5 & 0.5 & 1 \\ 1 & 1 & 1 & 1 & 1 \end{bmatrix}. \quad (4.5)$$

The elements of  $C_{i,j,z}$  ( $c_{z|i,j}$ ), where  $z$  stands for the the elements of the considered matrix ( $R$ ,  $G$  or  $B$ ) corresponding to the principal image, are then inserted in equation (4.3) substituting the elements of matrix  $A$ , and excluding the SBPI contribution ( $J(\cdot)$ ) as

$$h_{z|i,j}^{\tau+1} = M \left( \sum_{z=1}^{N_n} c_{z|i,j} h_{x|i,j}^{\tau} - \theta_2 \right), \quad (4.6)$$

where  $\theta_2$  is a second threshold applied which is set to  $3(\sum_{i,j} c_{i,j})/2 = 30$ . Equation (4.6) is a second CA that exploits the information obtained from the first. Through this operation a second mask  $s_{i,j}$  is obtained as shown in equation (4.4). The last operation is an averaging, done directly on the mask  $s$ . This averaging procedure is done to exclude the eventual false positives that remain in the mask though the two CAs applied. The calculation of the area of the sore is given by the count of the "positive" pixels in mask  $s$  and dimensioned through the curve  $D(\cdot)$ .

To measure the depth of the wound, as mentioned above, it is necessary to analyze the other images taken enlightening the sore from different positions with the LEDs, implemented in the device. First it is necessary to state that in order to decrease the effect of the relative movement between the device and the patient during the capture, the system has been designed to perform the data collection in a very small time frame ( $\leq 10s$ ). With the same principle of the wound recognition, still performing the SBPI-CA, it is possible to detect the shades generated by the skin borders with the sore with a very high precision. This is possible exploiting the data from the mask  $s_{i,j}$ . Identifying the borders through the mask it is possible to evaluate the pixels in the *secondary* images (i.e. the rest of the picture taken switching on and off consequently the LEDs) which are more enlightened with respect to the ones closer to the border, taking into account the correspondent illuminating LED. Figure 4.7 shows a schematic example of this principle.

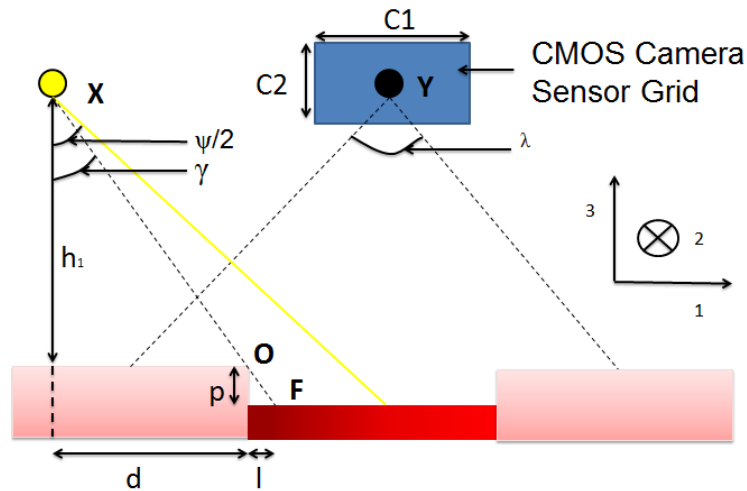


Fig. 4.7 Schematic example of the shade detection taken from an ulcer.  $Y$  is the center of the CMOS camera,  $X$  is the position of the given LED,  $O$  is the point of incidence of the light with the skin border and  $F$  is the end point of the shadow generated by the border with the given LED light. Still in the figure:  $h_1$  is the distance of the device from the skin,  $\lambda$  is the focal opening angle of the CMOS camera,  $\psi$  is the opening angle of the LED light (given by the data-sheet of the element),  $\gamma$  is the angle of incidence of the light with the skin border,  $p$  is the height of the skin border related to the wound,  $d$  is the length of the skin portion normal to the projection of the light, and finally  $l$  is the length of the shadow.  $C_1$  and  $C_2$  indicate the dimensions of the CMOS camera sensor. All the values are known thanks to the measurements of the device's sensors and from the design of the device itself, except for  $p$ ,  $\gamma$  and  $l$  that must be calculated through the here following procedure. In the figure is also reported the reference system with the directions 1, 2 and 3.

As mentioned in the caption of Figure 4.7, all the indicated values are known *a priori* from the device's and element's specifications, other than from the measurements performed and the data collected as described previously in this paragraph. From the data collected by the PING distance sensor it is possible to calculate the position in space of the camera (referring to its center)  $Y(y_1, y_2, y_3)$  and of the given LED light  $X(x_1, x_2, x_3)$ . All the coordinates of the points here described are referred to the directions 1, 2 and 3 reported in Figure 4.7. Also the distance  $h_1$  is known from the PING and the illumination demi-angle of the light  $\psi/2$  is given by the data-sheet of the element. The focal range angle  $\lambda$  of the CMOS camera is known from its data-sheet. The points of the image  $O(o_1, o_2, o_3)$  and  $F(f_1, f_2, f_3)$  are calculated through the SBPI-CA, the first is taken from the analysis of the principal image, while the second from the processing of the single secondary image. From this data it is possible to calculate the parameters  $d$ ,  $\gamma$  and  $l$  as:

$$d = \sqrt{(o_1 - x_1)^2 + (o_2 - x_2)^2}, \quad (4.7)$$

$$\gamma = \arctan\left(\frac{D}{h_1}\right), \quad (4.8)$$

$$l = \sqrt{(f_1 - x_1)^2 + (f_2 - x_2)^2}. \quad (4.9)$$

Finally, it is possible to compute the depth  $p$  as:

$$p = l \frac{\cos(\gamma)}{\sin(\gamma)}. \quad (4.10)$$

Last, the granulation is evaluated from the principal picture of the sore. In this paragraph is mentioned that before testing the device and designing the recognition algorithm, a set of digital pictures was taken for preliminary evaluation. The tissues composing the ulcer are evaluated by physicians visually and are classified according to the colour. From the test set of pictures all the possible pathological tissues have been analyzed regarding their colour. Four colours have been chosen as the most important since they collect all the possibilities excluding sane skin which are: black (necrosis), red (granulation), yellow (fibrin) and white (infection). All the colours have been evaluated and for all of them a tolerance range has been set. This is of primary importance for the association of the given wound with its WBP score as explained in Tables 4.2 and 4.3, other than in [135]. Once the measurement of the surface and of the depth has been performed, the corresponding pixels of the principal image with the mask  $s_{i,j}$  are read through their RGB values and classified accordingly in one of the four possible classes.

### 4.3.2 Pre-Clinical Trials and Results

This paragraph has the scope to describe the procedure and the results of the pre-clinical trials done on the system to prove the efficacy of this technology. These tests are called *pre-clinical* since they are the first step of the technology certification procedure which is purely scientific. The results taken from these test have the scope, by EU laws (CEI-EN 47-2007), to apply to the Ministry of Public Health of the referring country (i.e. the country where most of the development has taken place,

Table 4.4 Patient test population characteristics

Characteristic	Description
Number of patients	200
Gender	Male: 36% Female: 64%
Ethnical group	European Caucasian: 95.5% African: 3% Asian: 1.5%
Total number of ulcers	213
Average number of ulcers per patient	1.065

in this particular case Italy) for granting the possibility to initiate the certification procedures and start the *certified clinical trials*.

Regarding the EU law on medical devices (CEI-EN 47-2007) the system here proposed can be classified as *class I*. This classification states the non-invasive nature of the device and that it doesn't represent a risk nor for the operator, nor for the patient. This system is not diagnostic, since it returns objective information regarding the wound. This system as so is intended to be an aid to the decision of the physician regarding the specified cases.

The pre-clinical trials here presented were performed with the help of Dr. Elia Ricci, as afore mentioned, and its patients. A population of 200 patients was chosen randomly, with randomized pathologies and syndromes. In other word the typology of the ulcers of each patient as not before predictable. Moreover the patients are part of three distinct racial groups: African, Caucasic European and Asian, with different skin colours. In Table 4.4 are reported all the preliminary information regarding the patient population on which the device was tested.

The trials were performed confronting the measurements made on the ulcers by the here proposed system with the measurements performed by other devices and the diagnosis made by the physician. Regarding the measurement of the ulcer's area, the wound was measured with a device known as *Visitrack*, developed by *Smith & Nephew*. This device consists of a portable digital board and celluloid transparent films. One film os posed on the wound and with a marker the operator traces on it its borders. The traced film is the put on the digital board and the mark is retraced on it with a touch pen. The board, when it senses that the trace has a closed shape, returns the wound's surface. The depth value used to compare the measurements taken with

the system, was calculated with the use of cotton tips placed in the sore and marked when reached the bottom tissue layer. This method though being the most invasive, is the most commonly used by physicians. At last, for confronting the measurements done on the granulation the WBP score was used, comparing the one given by the operator through a visual analysis and the one returned by the system.

The sample wound population evaluated in the trials is described in Table 4.5. In the table is reported the etiology of the wounds, i.e. the pathologic incidence that brought the sore to manifestation. Also in the same table are reported the WBP scores given to the wounds and the anatomical depth that each wound reached, showing that the sample is composed by ulcers of different entities and gravities.

As mentioned before all the measurements taken with the proposed system were compared with measurements taken through the commonly used devices and methods for wound assessment. From this comparison it resulted that in more than 70% of the cases the system was able to measure the area with an accuracy of more than 85%, as shown in Figure 4.8. In the same figure the data distribution was overlapped with a kernel (in figure shown with a red line). analyzing this curve it is possible to see that in very low cases the system was not able to perform a satisfying measurement. Moreover it is necessary to state that the measurements with lowest accuracy were the ones that were performed first, and the parameters of the SBPI-CA were then set and tailored on the features of the hardware device. In Figure 4.9 is shown an example of a picture of a wound taken with the device and analyzed through the SBPI-CA. It is possible to see that the algorithm was able to identify the wound from the rest of the picture. The mask shown in Figure 4.9 (b) was built setting the system in order to recognize not only the open skin, but also the peri-wound which in this particular case is considered part of the ulcer and classified as fibrinous tissue.

Regarding the other features, such as depth measurement and granulation assessment through the WBP score, Table 4.6 reports the results obtained from the trials.

From the results obtained from the pre-clinical trials it is possible to state that the here proposed system has a high measurement efficiency. It is clear, from the explanations given in sections 4.1 and 4.3 that this system has the required characteristics to be used in a clinical environment such as a hospital or by a physician. Moreover this device is completely non-invasive and harmless for the patients. As so it has been proven its capability of returning reliable data on the wound generating an important *aid to the decision of the physician* improving *patient's experience*.

Table 4.5 Wound sample characteristics

Characteristic	Description
Etiology	Venous: 15.89% Diabetes: 2.8% Mixture: 17.76% Decubitus: 6.54% Surgical: 4.67% Sickle Cell Anemia: 2.8% Mixed Diabetes: 0.93% Trauma: 8.41% Inflammatory: 4.67% Raynaud: 1.87% Vasculopathy: 20.56% Sclerodermis: 2.80% Talaxemy: 1.87% Piodermis: 1.87% Neuropatic Diabetes: 1.87% Necrobiosis Lipodica Diabeticorum: 0.93% Vascular Diabetes: 2.8% Osteimielitus: 0.93%
WBP Score	A1: 26.32% A2: 9.56% A3: 7.02% B1: 1.75% B2: 14.04% B3: 1.75% C1: 4.39% C2: 8.77% C3: 7.02% D1: 6.14% D2: 7.02% D3: 6.14%
Anatomical Depth	Epidermis: 30.36% Dermis: 31.25% Subcutaneous: 16.07% Band: 8.04% Muscle: 9.82% Bone: 4.46%

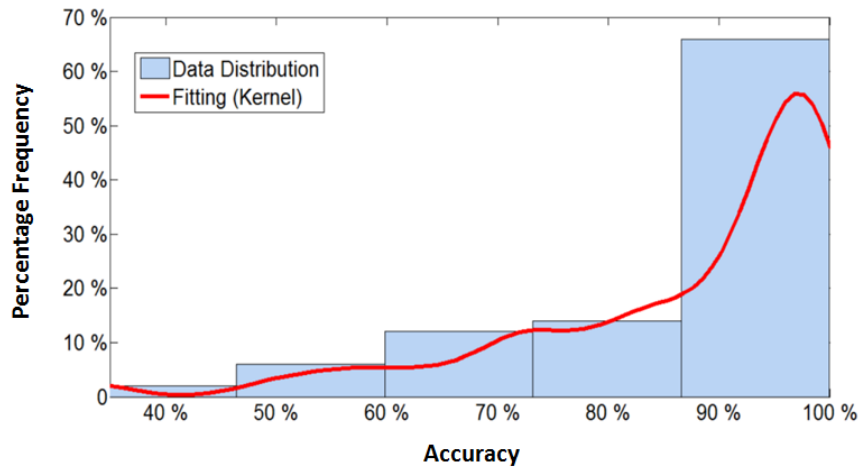


Fig. 4.8 Results of the measurements performed on the area of the wound. The results are shown relating the accuracy of the measurement with its frequency. The results are overlapped with a curve which represents the kernel of the data. From the graph it is possible to state that more than 70% of the cases were measured with an accuracy greater than 85%.

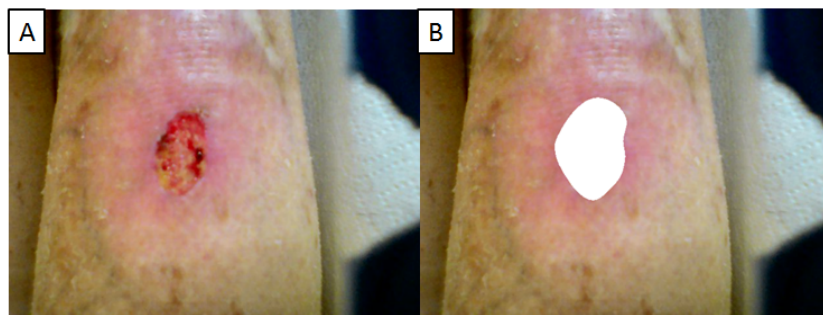


Fig. 4.9 (a) Sample picture of a wound and (b) mask of the wound built through the SBPI-CA. The system was able to recognize automatically the wound from the rest of the picture. Moreover the system was set to identify also portion of the peri-wound which have to be classified in the granulation assessment as pathological tissue.

Table 4.6 Pre-clinical trial system's efficiency results

Measurement (Feature)	Results (Efficiency)
Wound Detection	Automatically detected in 100% of the cases
Area Measurement	Median accuracy: 94.17% Mean Accuracy: 87.01% Standard Deviation: 15.28%
Depth Measurement	Median Accuracy: 91.23% Mean Accuracy: 84.91% Standard Deviation: 12.34%
Granulation (Based on WBP Score)	Median Accuracy: 97.81% Mean Accuracy: 92.01% Standard Deviation: 8.78%

# Chapter 5

## Conclusion

Memristors are considered the new generation of electronic elements. This is due to several reasons: first memristors, thanks to their particular and singular dynamics, drew the interest of the scientific community on new methods of computation such as neural networks, cellular neural networks or in general bio-inspired computing. From the early 2000s the world became more and more connected through the internet and this led to a very large number of data that has to be continuously processed. Moreover there is the sustained scientific will of discovering the still hiding and unknown features and functionalities of the brain. Neuromorphic systems have proved to be the best path in order to put the two things together, proving its efficacy and its efficiency of analyzing a greater and greater number of delocalized data.

On the other hand, the word "memristor" took with the years a larger and larger connotation. New elements, thanks to the unbreakable work of Professor Leon Chua and the whole scientific community, are now considered to have memristive behaviour. The use of such elements is strongly bonded to their capability of implementation in larger and more complex systems. Their behaviour has so to be well understood and has necessary to be predictable for the designers and the engineering community. Now most of them can be considered as *off the shelf* technologies thanks to memristor theory, i.e  $\varphi - -q$  models.

This work has been done, as shown in the previous chapters, for several kinds of elements such as *phase change memories*, *silicon nano-wires* and also for the canonic William's device. These same models were used to implement memristors in more complex systems and make them the key element for neuromorphic computing. For

instance it has been shown and described the computing efficiency of a memristive perceptron. Moreover its efficiency has made possible the design of systems and devices for wider utilities, such as biomedics.

The system for ulcer detection and follow-up here presented represents the final step of a road map that begins from the basic element theory to utility design. This same system is the result of a deep analysis on memristive systems and it represents the proof of concept of future applications of memristors. Obviously the importance of such system resides also in its use. The final goal of each technology should be the proof of their ability of comforting and aiding the progress of mankind and of this world. With this system it was possible to relief from pain more than 200 patients and giving to the medical and scientific community the hope for arrival of new devices, and new technologies that can and must improve patient care and experience.

From a scientific point of view this work has the scope to fill a gap between element development and system design. The modeling of memristive devices, as it has been proved in the previous chapters, leads to better data management and new solutions to more impelling and ambitious problems.

# References

- [1] Leon Chua. Memristor-the missing circuit element. *IEEE Transactions on circuit theory*, 18(5):507–519, 1971.
- [2] Dmitri B Strukov, Gregory S Snider, Duncan R Stewart, and R Stanley Williams. The missing memristor found. *nature*, 453(7191):80–83, 2008.
- [3] Dalibor Biolek, Sandro Carrara, Elisabetta Chicca, Fernando Corinto, Julius Georgiou, Bernabé Linares-Barranco, Themis Prodromakis, Sabina Spiga, and Ronald Tetzlaff. Eu cost action ic1401–pushing the frontiers of memristive devices to systems. In *Proceedings of the Melecon Conference in Cyprus*, 2016.
- [4] J Joshua Yang, Dmitri B Strukov, and Duncan R Stewart. Memristive devices for computing. *Nature nanotechnology*, 8(1):13–24, 2013.
- [5] Leon Chua. Resistance switching memories are memristors. *Applied Physics A*, 102(4):765–783, 2011.
- [6] Shari Lim Wei, Eleni Vasilaki, Ali Khiat, Iulia Salaoru, Radu Berdan, and Themistoklis Prodromakis. Emulating long-term synaptic dynamics with memristive devices. *arXiv preprint arXiv:1509.01998*, 2015.
- [7] Radu Berdan, Eleni Vasilaki, Ali Khiat, Giacomo Indiveri, Alexandru Serb, and Themistoklis Prodromakis. Emulating short-term synaptic dynamics with memristive devices. *Scientific reports*, 6, 2016.
- [8] Sylvain Saïghi, Christian G Mayr, Teresa Serrano-Gotarredona, Heidemarie Schmidt, Gwendal Lecerf, Jean Tomas, Julie Grollier, Sören Boyn, Adrien F Vincent, Damien Querlioz, et al. Plasticity in memristive devices for spiking neural networks. *Frontiers in neuroscience*, 9:51, 2015.
- [9] R Berdan, T Prodromakis, I Salaoru, A Khiat, and C Toumazou. Memristive devices as parameter setting elements in programmable gain amplifiers. *Applied Physics Letters*, 101(24):243502, 2012.
- [10] Sieu D Ha and Shriram Ramanathan. Adaptive oxide electronics: A review. *Journal of Applied Physics*, 110(7):071101, 2011.

- [11] Reut Wizenberg, Ali Khiat, Radu Berdan, Christos Papavassiliou, and Themistoklis Prodromakis. Applications of solid-state memristors in tunable filters. In *2014 IEEE International Symposium on Circuits and Systems (ISCAS)*, pages 2269–2272. IEEE, 2014.
- [12] Nicolas Locatelli, Vincent Cros, and Julie Grollier. Spin-torque building blocks. *Nature materials*, 13(1):11–20, 2014.
- [13] André Chanthbouala, Vincent Garcia, Ryan O Cherifi, Karim Bouzehouane, Stéphane Fusil, Xavier Moya, Stéphane Xavier, Hiroyuki Yamada, Cyrille Deranlot, Neil D Mathur, et al. A ferroelectric memristor. *Nature materials*, 11(10):860–864, 2012.
- [14] Leon Chua. If it’s pinched it’s a memristor. *Semiconductor Science and Technology*, 29(10):104001, 2014.
- [15] Sandro Carrara, Davide Sacchetto, Marie-Agnès Doucey, Camilla Baj-Rossi, Giovanni De Micheli, and Yusuf Leblebici. Memristive-biosensors: A new detection method by using nanofabricated memristors. *Sensors and Actuators B: Chemical*, 171:449–457, 2012.
- [16] D Biolek, V Biolkova, and Z Biolek. Spice model of memristor with nonlinear dopant drift. *Radioengineering*, 2009.
- [17] Zdenek Biolek, Dalibor Biolek, and Viera Biolková. Specification of one classical fingerprint of ideal memristor. *Microelectronics Journal*, 46(4):298–300, 2015.
- [18] Zdeněk Biolek, Dalibor Biolek, Viera Biolková, and Zdeněk Kolka. Variation of a classical fingerprint of ideal memristor. *International Journal of Circuit Theory and Applications*, 2015.
- [19] Hisham Abdalla and Matthew D Pickett. Spice modeling of memristors. In *2011 IEEE International Symposium of Circuits and Systems (ISCAS)*, 2011.
- [20] Zdenek Kolka, Dalibor Biolek, and Viera Biolkova. Improved model of tio2 memristor. *Radioengineering*, 24(2):378–383, 2015.
- [21] Alon Ascoli, Fernando Corinto, and Ronald Tetzlaff. Generalized boundary condition memristor model. *International Journal of Circuit Theory and Applications*, 44(1):60–84, 2016.
- [22] Iliia Valov, Eike Linn, Stefan Tappertzhofen, Sebastian Schmelzer, J Van den Hurk, Florian Lentz, and Rainer Waser. Nanobatteries in redox-based resistive switches require extension of memristor theory. *Nature communications*, 4:1771, 2013.
- [23] J Georgiou, E Kyriakides, and C Hadjistassou. Niti smart alloys for memristors with multi-time-scale volatility. *Electronics letters*, 48(14):1, 2012.

- [24] Evripides Kyriakides, Constantinos Hadjistassou, and Julius Georgiou. A new memristor based on niti smart alloys. In *2012 IEEE International Symposium on Circuits and Systems*, pages 1403–1406. IEEE, 2012.
- [25] Fernando Corinto and Mauro Forti. Memristor circuits: Flux charge analysis method.
- [26] Fernando Corinto, Pier Paolo Civalleri, and Leon O Chua. A theoretical approach to memristor devices. *Emerging and Selected Topics in Circuits and Systems, IEEE Journal on*, 5(2):123–132, 2015.
- [27] Simone Raoux, Geoffrey W Burr, Matthew J Breitwisch, Charles T Rettner, Yi-Chou Chen, Robert M Shelby, Martin Salinga, Daniel Krebs, S-H Chen, Hsiang-Lan Lung, et al. Phase-change random access memory: A scalable technology. *IBM Journal of Research and Development*, 52(4.5):465–479, 2008.
- [28] Abu Sebastian, Manuel Le Gallo, and Daniel Krebs. Crystal growth within a phase change memory cell. *Nature communications*, 5, 2014.
- [29] Leon O Chua and Lin Yang. Cellular neural networks: Applications. *IEEE Transactions on circuits and systems*, 35(10):1273–1290, 1988.
- [30] John J Hopfield. Neural networks and physical systems with emergent collective computational abilities. *Proceedings of the national academy of sciences*, 79(8):2554–2558, 1982.
- [31] Stephen Wolfram. Universality and complexity in cellular automata. *Physica D: Nonlinear Phenomena*, 10(1):1–35, 1984.
- [32] Andrew McAfee, Erik Brynjolfsson, Thomas H Davenport, DJ Patil, and Dominic Barton. Big data. *The management revolution. Harvard Bus Rev*, 90(10):61–67, 2012.
- [33] Frank Rosenblatt. The perceptron: a probabilistic model for information storage and organization in the brain. *Psychological review*, 65(6):386, 1958.
- [34] Carlo Baldassi, Alfredo Braunstein, Nicolas Brunel, and Riccardo Zecchina. Efficient supervised learning in networks with binary synapses. *BMC Neuroscience*, 8(2):1, 2007.
- [35] Saeed Reza Kheradpisheh, Mohammad Ganjtabesh, and Timothée Masquelier. Bio-inspired unsupervised learning of visual features leads to robust invariant object recognition. *Neurocomputing*, 205:382–392, 2016.
- [36] Jürgen Schmidhuber. Deep learning in neural networks: An overview. *Neural Networks*, 61:85–117, 2015.

- [37] Steve B Furber, David R Lester, Luis A Plana, Jim D Garside, Eustace Painkras, Steve Temple, and Andrew D Brown. Overview of the spinnaker system architecture. *IEEE Transactions on Computers*, 62(12):2454–2467, 2013.
- [38] Kuk-Hwan Kim, Siddharth Gaba, Dana Wheeler, Jose M Cruz-Albrecht, Tahir Hussain, Narayan Srinivasa, and Wei Lu. A functional hybrid memristor crossbar-array/cmos system for data storage and neuromorphic applications. *Nano letters*, 12(1):389–395, 2011.
- [39] Mirko Prezioso, Farnood Merrih-Bayat, BD Hoskins, GC Adam, Konstantin K Likharev, and Dmitri B Strukov. Training and operation of an integrated neuromorphic network based on metal-oxide memristors. *Nature*, 521(7550):61–64, 2015.
- [40] Teresa Serrano-Gotarredona, Themistoklis Prodromakis, and Bernabe Linares-Barranco. A proposal for hybrid memristor-cmos spiking neuromorphic learning systems. *IEEE Circuits and Systems Magazine*, 13(2):74–88, 2013.
- [41] Makoto Itoh and Leon O Chua. Memristor cellular automata and memristor discrete-time cellular neural networks. *International Journal of Bifurcation and Chaos*, 19(11):3605–3656, 2009.
- [42] Marius Orłowski, Jacopo Secco, and Fernando Corinto. Chua’s constitutive memristor relations for physical phenomena at metal–oxide interfaces. *Emerging and Selected Topics in Circuits and Systems, IEEE Journal on*, 5(2):143–152, 2015.
- [43] Leon O Chua. *Introduction to nonlinear network theory*. McGraw-Hill, 1969.
- [44] RJ Duffin. Nonlinear networks. i. *Bulletin of the American Mathematical Society*, 52(10):833–838, 1946.
- [45] Charles A Desoer and Jacob Katzenelson. Nonlinear rlc networks. *Bell System Technical Journal*, 44(1):161–198, 1965.
- [46] Sundaram Seshu and Myril Baird Reed. *Linear graphs and electrical networks*. Addison-Wesley Pub. Co., 1961.
- [47] Leon O Chua. Synthesis of new nonlinear network elements. *Proceedings of the IEEE*, 56(8):1325–1340, 1968.
- [48] Sung Hyun Jo, Ting Chang, Idongesit Ebong, Bhavitavya B Bhadviya, Pinaki Mazumder, and Wei Lu. Nanoscale memristor device as synapse in neuromorphic systems. *Nano letters*, 10(4):1297–1301, 2010.
- [49] Yenpo Ho, Garng M Huang, and Peng Li. Nonvolatile memristor memory: device characteristics and design implications. In *Proceedings of the 2009 International Conference on Computer-Aided Design*, pages 485–490. ACM, 2009.

- [50] Navaneethan Duraisamy, Nauman Malik Muhammad, Hyung-Chan Kim, Jeong-Dai Jo, and Kyung-Hyun Choi. Fabrication of tio<sub>2</sub> thin film memristor device using electrohydrodynamic inkjet printing. *Thin Solid Films*, 520(15):5070–5074, 2012.
- [51] Antonio S Oblea, Achyut Timilsina, David Moore, and Kristy A Campbell. Silver chalcogenide based memristor devices. 2010.
- [52] Son Ngoc Truong, Seok Jin Ham, and Kyeong Sik Min. Neuromorphic crossbar circuit with nanoscale filamentary switching binary memristors for speech recognition. *Nanoscale research letters*, 9(1):1–9, 2014.
- [53] Julien Borghetti, Gregory S Snider, Philip J Kuekes, J Joshua Yang, Duncan R Stewart, and R Stanley Williams. Memristive switches enable stateful logic operations via material implication. *Nature*, 464(7290):873–876, 2010.
- [54] Sangho Shin, Kyungmin Kim, and Sung-Mo Kang. Memristor applications for programmable analog ics. *IEEE Transactions on Nanotechnology*, 10(2):266–274, 2011.
- [55] Fernando Corinto, Alon Ascoli, and Marco Gilli. Nonlinear dynamics of memristor oscillators. *IEEE Transactions on Circuits and Systems I: Regular Papers*, 58(6):1323–1336, 2011.
- [56] Bharathwaj Muthuswamy and Leon Chua. Simplest chaotic circuit. *International Journal of Bifurcation and Chaos*, 20(05):1567–1580, 2010.
- [57] J C Sprott. A new class of chaotic circuit. *Physics Letters A*, 266(1):19–23, 2000.
- [58] Leon O Chua and Sung Mo Kang. Memristive devices and systems. *Proceedings of the IEEE*, 64(2):209–223, 1976.
- [59] Fernando Corinto, Alon Ascoli, and Marco Gilli. Analysis of current–voltage characteristics for memristive elements in pattern recognition systems. *International journal of circuit theory and applications*, 40(12):1277–1320, 2012.
- [60] Leon O Chua. The fourth element. *Proceedings of the IEEE*, 100(6):1920–1927, 2012.
- [61] Fernando Corinto and Alon Ascoli. Memristive diode bridge with lcr filter. *Electronics Letters*, 48(14):1, 2012.
- [62] Antonio C Torrezan, John Paul Strachan, Gilberto Medeiros-Ribeiro, and R Stanley Williams. Sub-nanosecond switching of a tantalum oxide memristor. *Nanotechnology*, 22(48):485203, 2011.
- [63] A Talukdar, Ahmed Gomaa Radwan, and Khaled N Salama. Non linear dynamics of memristor based 3rd order oscillatory system. *Microelectronics journal*, 43(3):169–175, 2012.

- [64] Dmitri B Strukov, Duncan R Stewart, Julien Borghetti, Xuema Li, Matthew D Pickett, Gilberto Medeiros-Ribeiro, Warren Robinett, Gregory S Snider, John Paul Strachan, Wei Wu, et al. Hybrid cmos/memristor circuits. In *ISCAS*, pages 1967–1970. Citeseer, 2010.
- [65] Massimiliano Versace and Ben Chandler. Moneta: A mind made from memristors. *IEEE Spectrum*, 47(12):30–37, 2010.
- [66] Yuriy V Pershin, Steven La Fontaine, and Massimiliano Di Ventra. Memristive model of amoeba learning. *Physical Review E*, 80(2):021926, 2009.
- [67] Gorm Krogh Johnsen. An introduction to the memristor—a valuable circuit element in bioelectricity and bioimpedance. *Journal of Electrical Bioimpedance*, 3(1):20–28, 2012.
- [68] Yogesh N Joglekar and Stephen J Wolf. The elusive memristor: properties of basic electrical circuits. *European Journal of Physics*, 30(4):661, 2009.
- [69] Themistoklis Prodromakis, Boon Pin Peh, Christos Papavassiliou, and Christofer Toumazou. A versatile memristor model with nonlinear dopant kinetics. *IEEE transactions on electron devices*, 58(9):3099–3105, 2011.
- [70] Fernando Corinto and Alon Ascoli. A boundary condition-based approach to the modeling of memristor nanostructures. *IEEE Transactions on Circuits and Systems I: Regular Papers*, 59(11):2713–2726, 2012.
- [71] Shahar Kvatinsky, Eby G Friedman, Avinoam Kolodny, and Uri C Weiser. Team: threshold adaptive memristor model. *IEEE Transactions on Circuits and Systems I: Regular Papers*, 60(1):211–221, 2013.
- [72] Alon Ascoli, Fernando Corinto, Vanessa Senger, and Ronald Tetzlaff. Memristor model comparison. *IEEE Circuits and Systems Magazine*, 13(2):89–105, 2013.
- [73] John G Simmons. Electric tunnel effect between dissimilar electrodes separated by a thin insulating film. *Journal of applied physics*, 34(9):2581–2590, 1963.
- [74] Eike Linn, Anne Siemon, Rainer Waser, and Stephan Menzel. Applicability of well-established memristive models for simulations of resistive switching devices. *IEEE Transactions on Circuits and Systems I: Regular Papers*, 61(8):2402–2410, 2014.
- [75] J Joshua Yang, Feng Miao, Matthew D Pickett, Douglas AA Ohlberg, Duncan R Stewart, Chun Ning Lau, and R Stanley Williams. The mechanism of electroforming of metal oxide memristive switches. *Nanotechnology*, 20(21):215201, 2009.
- [76] Shimeng Yu, Ximeng Guan, and H-S Philip Wong. Conduction mechanism of tin/hfox/pt resistive switching memory: a trap-assisted-tunneling model. *Applied Physics Letters*, 99(6):063507, 2011.

- [77] Daniele Ielmini, Federico Nardi, and Simone Balatti. Evidence for voltage-driven set/reset processes in bipolar switching rram. *IEEE Transactions on Electron Devices*, 59(8):2049–2056, 2012.
- [78] John Paul Strachan, Antonio C Torrezan, Feng Miao, Matthew D Pickett, J Joshua Yang, Wei Yi, Gilberto Medeiros-Ribeiro, and R Stanley Williams. State dynamics and modeling of tantalum oxide memristors. *IEEE Transactions on Electron Devices*, 60(7):2194–2202, 2013.
- [79] Lu Zhang, Zhijie Chen, J Joshua Yang, Bryant Wysocki, Nathan McDonald, and Yiran Chen. A compact modeling of tio<sub>2</sub>-tio<sub>2</sub>-x memristor. *Applied Physics Letters*, 102(15):153503, 2013.
- [80] Tong Liu, Yuhong Kang, Sarah El-Helw, Tanmay Potnis, and Marius Orlowski. Physics of the voltage constant in multilevel switching of conductive bridge resistive memory. *Japanese Journal of Applied Physics*, 52(8R):084202, 2013.
- [81] Gargi Ghosh and Marius K Orlowski. Write and erase threshold voltage interdependence in resistive switching memory cells. *IEEE Transactions on Electron Devices*, 62(9):2850–2856, 2015.
- [82] C Schindler, G Staikov, and R Waser. Electrode kinetics of cu-sio<sub>2</sub>-based resistive switching cells: Overcoming the voltage-time dilemma of electrochemical metallization memories. *Applied physics letters*, 94(7):2109, 2009.
- [83] Sungho Kim, Sae-Jin Kim, Kyung Min Kim, Seung Ryul Lee, Man Chang, Eunju Cho, Young-Bae Kim, Chang Jung Kim, U-In Chung, and In-Kyeong Yoo. Physical electro-thermal model of resistive switching in bi-layered resistance-change memory. *Scientific reports*, 3:1680, 2013.
- [84] Ugo Russo, Daniele Ielmini, Carlo Cagli, and Andrea L Lacaita. Self-accelerated thermal dissolution model for reset programming in unipolar resistive-switching memory (rram) devices. *IEEE Transactions on Electron Devices*, 56(2):193–200, 2009.
- [85] T Liu. Dissertation, vtech 2015.
- [86] H-S Philip Wong and Sayeef Salahuddin. Memory leads the way to better computing. *Nature nanotechnology*, 10(3):191–194, 2015.
- [87] Andrea L Lacaita and Andrea Redaelli. The race of phase change memories to nanoscale storage and applications. *Microelectronic Engineering*, 109:351–356, 2013.
- [88] Geoffrey W Burr, Matthew J Brightsky, Abu Sebastian, Huai-Yu Cheng, Jau-Yi Wu, Sangbum Kim, Norma E Sosa, Nikolaos Papandreou, Hsiang-Lan Lung, Haralampos Pozidis, et al. Recent progress in phase-change memory technology. *IEEE Journal on Emerging and Selected Topics in Circuits and Systems*, 2016.

- [89] Duygu Kuzum, Rakesh GD Jeyasingh, Byoungil Lee, and H-S Philip Wong. Nanoelectronic programmable synapses based on phase change materials for brain-inspired computing. *Nanoletters*, 12(5):2179–2186, 2011.
- [90] Tomas Tuma, Angeliki Pantazi, Manuel Le Gallo, Abu Sebastian, and Evangelos Eleftheriou. Stochastic phase-change neurons. *Nature nanotechnology*, 2016.
- [91] Peiman Hosseini, Abu Sebastian, Nikolaos Papandreou, C David Wright, and Harish Bhaskaran. Accumulation-based computing using phase-change memories with fet access devices. *IEEE Electron Device Letters*, 36(9):975–977, 2015.
- [92] A Redaelli, A Pirovano, A Benvenuti, and AL Lacaïta. Threshold switching and phase transition numerical models for phase change memory simulations. *Journal of Applied Physics*, 103(11):111101, 2008.
- [93] Nicola Ciocchini, Mario Laudato, Antonio Leone, Paolo Fantini, Andrea L Lacaïta, and Daniele Ielmini. Impact of thermoelectric effects on phase change memory characteristics. *IEEE Transactions on Electron Devices*, 62(10):3264–3271, 2015.
- [94] Abu Sebastian, Manuel Le Gallo, and Daniel Krebs. Crystal growth within a phase change memory cell. *Nature communications*, 5, 2014.
- [95] Daniele Ielmini and Yuegang Zhang. Analytical model for subthreshold conduction and threshold switching in chalcogenide-based memory devices. *Journal of Applied Physics*, 102(5):054517, 2007.
- [96] Manuel Le Gallo, Matthias Kaes, Abu Sebastian, and Daniel Krebs. Subthreshold electrical transport in amorphous phase-change materials. *New Journal of Physics*, 17(9):093035, 2015.
- [97] Agostino Pirovano, Andrea L Lacaïta, Augusto Benvenuti, Fabio Pellizzer, and Roberto Bez. Electronic switching in phase-change memories. *Electron Devices, IEEE Transactions on*, 51(3):452–459, 2004.
- [98] Manuel Le Gallo, Aravinthan Athmanathan, Daniel Krebs, and Abu Sebastian. Evidence for thermally assisted threshold switching behavior in nanoscale phase-change memory cells. *Journal of Applied Physics*, 119(2):025704, 2016.
- [99] Francesca Puppo, Massimiliano Di Ventra, Giovanni De Micheli, and Sandro Carrara. Memristive sensors for ph measure in dry conditions. *Surface Science*, 624:76–79, 2014.
- [100] Ioulia Tzouvadaki, Francesca Puppo, Marie-Agnès Doucey, Giovanni De Micheli, and Sandro Carrara. Computational study on the electrical behavior of silicon nanowire memristive biosensors. *IEEE Sensors Journal*, 15(11):6208–6217, 2015.

- [101] Francesca Puppo, Massimiliano Di Ventra, Giovanni De Micheli, and Sandro Carrara. Memristive sensors for pH measure in dry conditions. *Surface Science*, 624:76–79, 2014.
- [102] Leon O Chua and Lin Yang. Cellular neural networks: Applications. *IEEE Transactions on circuits and systems*, 35(10):1273–1290, 1988.
- [103] Shyam Prasad Adhikari, Maheshwar Pd Sah, Hyongsuk Kim, and Leon O Chua. Three fingerprints of memristor. *IEEE Transactions on Circuits and Systems I: Regular Papers*, 60(11):3008–3021, 2013.
- [104] Alon Ascoli, Fernando Corinto, and Ronald Tetzlaff. A class of versatile circuits, made up of standard electrical components, are memristors. *International Journal of Circuit Theory and Applications*, 44(1):127–146, 2016.
- [105] Robert W Williams and Karl Herrup. The control of neuron number. *Annual review of neuroscience*, 11(1):423–453, 1988.
- [106] Carver Mead. Neuromorphic electronic systems. *Proceedings of the IEEE*, 78(10):1629–1636, 1990.
- [107] Frederico AC Azevedo, Ludmila RB Carvalho, Lea T Grinberg, José Marcelo Farfel, Renata EL Ferretti, Renata EP Leite, Roberto Lent, Suzana Herculano-Houzel, et al. Equal numbers of neuronal and nonneuronal cells make the human brain an isometrically scaled-up primate brain. *Journal of Comparative Neurology*, 513(5):532–541, 2009.
- [108] Mirko Prezioso, Farnood Merrikh-Bayat, BD Hoskins, GC Adam, Konstantin K Likharev, and Dmitri B Strukov. Training and operation of an integrated neuromorphic network based on metal-oxide memristors. *Nature*, 521(7550):61–64, 2015.
- [109] Yann LeCun, Yoshua Bengio, and Geoffrey Hinton. Deep learning. *Nature*, 521(7553):436–444, 2015.
- [110] Alex Krizhevsky, Ilya Sutskever, and Geoffrey E Hinton. Imagenet classification with deep convolutional neural networks. In *Advances in neural information processing systems*, pages 1097–1105, 2012.
- [111] Geoffrey Hinton, Li Deng, Dong Yu, George E Dahl, Abdel-rahman Mohamed, Navdeep Jaitly, Andrew Senior, Vincent Vanhoucke, Patrick Nguyen, Tara N Sainath, et al. Deep neural networks for acoustic modeling in speech recognition: The shared views of four research groups. *Signal Processing Magazine, IEEE*, 29(6):82–97, 2012.
- [112] Gene A Frantz and Richard H Wiggins. Speech synthesis: Design case history: Speak & spell learns to talk: Designers of an electronic learning aid mastered advanced speech technology and meticulously prepared the consumer. *Spectrum, IEEE*, 19(2):45–49, 1982.

- [113] Frank Rosenblatt. The perceptron: a probabilistic model for information storage and organization in the brain. *Psychological review*, 65(6):386, 1958.
- [114] David E Rumelhart, Geoffrey E Hinton, and Ronald J Williams. Learning representations by back-propagating errors. *Cognitive modeling*, 5(3):1, 1988.
- [115] Fabien Alibart, Elham Zamanidoost, and Dmitri B Strukov. Pattern classification by memristive crossbar circuits using ex situ and in situ training. *Nature communications*, 4, 2013.
- [116] Daniel H O'Connor, Gayle M Wittenberg, and Samuel S-H Wang. Graded bidirectional synaptic plasticity is composed of switch-like unitary events. *Proceedings of the National Academy of Sciences of the United States of America*, 102(27):9679–9684, 2005.
- [117] Thomas M Bartol, Cailey Bromer, Justin P Kinney, Michael A Chirillo, Jennifer N Bourne, Kristen M Harris, and Terrence J Sejnowski. Hippocampal spine head sizes are highly precise. *bioRxiv*, page 016329, 2015.
- [118] Carlo Baldassi, Alessandro Ingrosso, Carlo Lucibello, Luca Saglietti, and Riccardo Zecchina. Subdominant dense clusters allow for simple learning and high computational performance in neural networks with discrete synapses. *Physical review letters*, 115(12):128101, 2015.
- [119] Kamran Eshraghian, Omid Kavehei, Kyoung-Rok Cho, James M Chappell, Azhar Iqbal, Said F Al-Sarawi, and Derek Abbott. Memristive device fundamentals and modeling: applications to circuits and systems simulation. *Proceedings of the IEEE*, 100(6):1991–2007, 2012.
- [120] Jennifer Hasler and Harry Bo Marr. Finding a roadmap to achieve large neuromorphic hardware systems. *Frontiers in neuroscience*, 7:118, 2013.
- [121] Johannes Fieres, Johannes Schemmel, and Karlheinz Meier. Realizing biological spiking network models in a configurable wafer-scale hardware system. In *2008 IEEE International Joint Conference on Neural Networks (IEEE World Congress on Computational Intelligence)*, pages 969–976. IEEE, 2008.
- [122] G Indiveri, T Horiuchi, E Niebur, and R Douglas. A competitive network of spiking vlsi neurons. In *World Congress on Neuroinformatics*, pages 443–455. Vienna, Austria: ARGESIM/ASIM Verlag, 2001.
- [123] Joseph Lin, Paul Merolla, John Arthur, and Kwabena Boahen. Programmable connections in neuromorphic grids. In *2006 49th IEEE International Midwest Symposium on Circuits and Systems*, volume 1, pages 80–84. IEEE, 2006.
- [124] Sylvie Renaud, Jean Tomas, Yannick Bornat, Adel Daouzli, and Sylvain Saïghi. Neuromimetic ics with analog cores: an alternative for simulating spiking neural networks. In *2007 IEEE international symposium on circuits and systems*, pages 3355–3358. IEEE, 2007.

- [125] Rae Silver, Kwabena Boahen, Sten Grillner, Nancy Kopell, and Kathie L Olsen. Neurotech for neuroscience: unifying concepts, organizing principles, and emerging tools. *The Journal of Neuroscience*, 27(44):11807–11819, 2007.
- [126] Sylvain Saïghi, Yannick Bornat, Jean Tomas, Gwendal Le Masson, and Sylvie Renaud. A library of analog operators based on the hodgkin-huxley formalism for the design of tunable, real-time, silicon neurons. *IEEE transactions on biomedical circuits and systems*, 5(1):3–19, 2011.
- [127] Djaafar Chabi, Weisheng Zhao, Damien Querlioz, and Jacques-Olivier Klein. Robust neural logic block (nlb) based on memristor crossbar array. In *2011 IEEE/ACM International Symposium on Nanoscale Architectures*, pages 137–143. IEEE, 2011.
- [128] Giulio Barbato, EM Barini, Gianfranco Genta, and Raffaello Levi. Features and performance of some outlier detection methods. *Journal of Applied Statistics*, 38(10):2133–2149, 2011.
- [129] Frank Werdin, Mayer Tennenhaus, Hans-Eberhardt Schaller, and Hans-Oliver Rennekampff. Evidence-based management strategies for treatment of chronic wounds. *Eplasty*, 9(19):169–179, 2009.
- [130] Finn Gottrup. Optimizing wound treatment through health care structuring and professional education. *Wound repair and regeneration*, 12(2):129–133, 2004.
- [131] Julia V Cornwall, Caroline J Doré, and JD Lewis. Leg ulcers: epidemiology and aetiology. *British Journal of Surgery*, 73(9):693–696, 1986.
- [132] David C Elliott, Joseph A Kufera, and Roy AMMD Myers. Necrotizing soft tissue infections. risk factors for mortality and strategies for management. *Annals of surgery*, 224(5):672, 1996.
- [133] J Stevens, PJ Franks, and M Harrington. A community/hospital leg ulcer service. *Journal of Wound Care*, 6:62–69, 1997.
- [134] Elia Ricci, Roberto Cassino, and Mario Nano. *Piaghe da decubito*. Minerva medica, 2004.
- [135] Gregory S Schultz, R Gary Sibbald, Vincent Falanga, Elizabeth A Ayello, Caroline Dowsett, Keith Harding, Marco Romanelli, Michael C Stacey, Luc Teot, and Wolfgang Vanscheidt. Wound bed preparation: a systematic approach to wound management. *Wound repair and regeneration*, 11(s1):S1–S28, 2003.

# List of Figures

1.1	Comparison of the memristor with the other three fundamental two-terminal circuit elements, respectively related to their descriptive variables. Through this figure it is possible to note the appropriateness of the <i>missing element</i> definition given by Professor Leon Chua in 1971. In the bottom right corner it is shown the circuit symbol of the memristor. This figure has been taken from the work of Strukov <i>et al.</i> [2]. . . . .	2
1.2	Equivalent circuit of the Generalized Boundary Condition Memristor (GBCM) developed by Ascoli <i>et al.</i> The circuit presented is taken directly from [21]. From the manipulation of the on and off state cells it is possible to modulate the effective resistance given by the series of $R_{off}$ and $R(v_x)$ , which is a non-linear resistor that depends on the voltage drop on the capacitor $C$ . $C$ , on the other hand expresses the volatility of the desired modeled device. . . . .	4
1.3	Example of physical deployment of memristors in a PCB architecture. PCB boards contain many functional elements. The implementation of memristor crossbar arrays permits an agile computing and selection of the desired element. In figure is reported a typical example taken from the work of Serrano-Gotarredona <i>et al.</i> [40]. . . . .	8
2.1	Figurative list of the mutators used by Chua to give the first proof of the existence of memristors in 1971. The reported figure is taken directly from [1]. . . . .	19

- 2.2 Example of a typical memristor pinched loop  $v - i$ . It is possible to note from the given example that the loop decreases, as so the memristor acted more and more as a generic resistor rather than a memristor. This phenomenon is given by the physical properties of the materials of which some memristive devices are built with. . . . 20
- 2.3 Example of an  $\mathcal{LM}$  circuit.  $S_1, S_2$  and  $S_3$  are switches that connect (or disconnect) the memristor  $M$  and the capacitor  $C$  with the linear networks  $\mathcal{L}_a$  and  $\mathcal{L}_b$ . By closing  $S_2$  and opening the rest of the switches, the reported circuit becomes an M-C circuit. The figure is taken from [25]. . . . . 23
- 2.4 Figurative example of the memristor developed at the HP labs by Strukov *et al.*  $W$  is the doped region of the device, or in other words the length of the conductive filament,  $D$  is the length of the whole device.  $V$  represents the input signal to the electrodes (full black areas at the devices' extremes), which according to William's configuration are made of platinum  $Pt$ . . . . . 32
- 2.5  $V_{set}$  as a function of frequency for three amplitudes  $V_0=1, 5, 20V$ . . . 37
- 2.6 The last stage of the detachment of the doped (conductive) electrolyte region from the metal electrode. The connection takes place only at a single asperity. The entire current, indicated by dashed arrows, crowds through the single asperity leading to a hot spot (concentric circles) characterized by  $T_{crit}$  in the center. . . . . 40
- 2.7 Doped conductive region is completely detached from the metal electrode by the minimal gap  $\Delta$ . The resulting effective boundary  $W_\Delta$  separating the conductive electrolyte region from the non-conductive region is shown by the dashed line. . . . . 42
- 2.8 Input voltage  $v(t)$  wave form used in numerical simulations of the memristor device modeled by (2.67). A seesaw wave form is chosen in order to have a constantly increasing and decreasing voltage during the essays. . . . . 45

- 2.9 (a) Graph showing  $A(\varphi(t))$ . From Figure 2.8 it is possible to see that the voltage crosses 0 V and becomes negative at  $t = 0.5s$ . From that instant  $A(\varphi)$  increases crossing 0 and becoming positive, since still in presence of a positive flux.  $A(\varphi)$  decreases afterwards reaching 0 again when  $\varphi_{crit}$  is reached. (b) The graph shows the dependency of  $A$  from  $\varphi$ . As afore mentioned there are two fluxes at which  $A(\varphi)$  is null. . . . . 47
- 2.10 (a)  $i-v$  curve for the general memristor without the implementation of the thermal detachment model. (b)  $i-v$  curve for the memristor with the implementation of the thermal detachment model (with the values described above). . . . . 48
- 2.11 Change of the doped region  $W(t)$  over time both for the general (no thermal model implemented) memristor and the device which resents from the thermal detachment effect. . . . . 49
- 2.12 Memristance change comparison for the general model and for the memristor element in which the thermal detachment model was implemented. The region in which there is the memristance change due to the thermal effects (conductive filament not yet ruptured) is put in to evidence by the green dashed square. In that region the memristance of the thermally controlled device follows  $R(A(\varphi))$  described behavior. . . . . 50
- 2.13 (a) Representation of  $A(\varphi(t))$  at different  $T_{crit}$ . (b) Representation of  $A(\varphi)$  for different  $T_{crit}$ . At different  $T_{crit}$  critical fluxes change accordingly. Since higher critical temperature needs a higher flux to be reached, the devices with higher  $T_{crit}$  will reach rupturing rater than the others. . . . . 51
- 2.14  $i-v$  curves of the five devices with different  $T_{crit}$ . Higher  $T_{crit}$  maintain the conductive region of the filament attached to the electrode longer, since more energy is required for the rupture. . . . . 52
- 2.15  $i-v$  curves at increasing  $E_a/k$  ratio. The critical temperature for the device was fixed to  $1000^\circ C$ . . . . . 53

- 2.16 (a) Schematic representation of a mushroom-type PCM device. In the RESET state, the phase change material in the amorphous phase blocks the bottom electrode and the device is in high resistance state. The effective thickness of the amorphous region is denoted by  $u_a$ .  $V_i$  denotes the voltage applied to the device and  $I$  denotes the resulting current flowing through the device. (b) A characteristic  $I$ - $V$  behavior is shown. It can be seen that above the threshold switching voltage ( $V_{th}$ ), the device exhibits a much lower resistance even in the RESET state. The READ and WRITE regions of the  $I$ - $V$  curve are shaded in yellow and blue respectively. . . . . 56
- 2.17 Experimentally obtained estimate of (a) the effective thermal resistance as a function of the amorphous thickness and (b) the temperature dependence of crystal growth velocity.  $T_M$  is the melting temperature of the GST, and from that point on the growth velocity can be considered negligible. Also shown are analytical approximations. . . . . 58
- 2.18 Figurative example of an input voltage waveform, related to the output current and the respective flux  $\varphi(t)$  and charge  $q(t)$ . The case shown is an example of constant writing voltage ( $V_w$ ) inputs given to the PCM cell. From the graphs it is possible to note that  $\varphi(t)$  and  $q(t)$  are calculated as the sum of the areas of the input voltages and output currents respectively. From the last graph it is possible to see that the flux of the reading voltage ( $V_r$ ) can be considered negligible with respect to the flux of  $V_w$ . On the other hand the charge of the current the reading phase increases at every input step. . . . . 59
- 2.19 Surface interpolating the experimental data in the  $(\varphi, q, u_a)$ -domain. The solid black lines highlight the curves that show the actual relationship built through the interpolation of the data obtained from all the simulations. . . . . 61
- 2.20 Interpolating lines derived from the  $(\varphi, q, u_a)$  surface in Figure 2.19. (a) Interpolating lines that show the family of curves describing  $q(u_a(t))$  and (b)  $\varphi(u_a(t))$  obtained from the simulations. . . . . 62
- 2.21 Surface interpolating the experimental data in the  $(\varphi, q, T)$ -domain. 63

- 2.22 SEM image of the SiNW after fabrication. The nano-wire is suspended between two *SiNi* electrodes [15]. . . . . 64
- 2.23  $V - I_n(I)$  curves showed by the SiNW after (a) and afore (b) functionalization, when applied a sinusoidal input signal. In panel-A it is evidenced the voltage gap that gives evidence of the covalent bonding of bio-molecules on the nano-wire. Under each panel are reported the circuit elements that show similar behaviour when excited by the same kind of signal. . . . . 65
- 2.24 SiNW equivalent electronic circuit. The values that were taken into account in order to evaluate the response of the simulation are the voltage drop over the SiNW ( $V$ ) and the total current flowing through the circuit ( $I$ ). . . . . 67
- 2.25 Simulation results of the equivalent circuit model of the SiNW. Next to each  $V - I_n I$  graph are reported the simulation conditions and the circuit element that generate such behaviour. . . . . 68
- 2.26 Versatile circuit presented that shows memristive properties [104]. In the paper the currents flowing through the various elements and the voltages applied to them will be cited with  $i$  with the subscript of the interested element. For instance the current flowing in the diode  $D_A$  will be named  $i_{D_A}$ . The current entering the circuit from the voltage source  $v_1$  (flowing into node A and outflowing from node C) will be named  $i_{in}$ . . . . . 72
- 2.27  $V-I$  curve obtained by applying three different sinusoidal input voltages to the circuit. All three signals have same amplitude ( $0.2V$ ), but differ from the frequency ( $0.1, 1$  and  $10Hz$ ). In the figure is mentioned the output of the  $0.1Hz$  sinusoid but it is not visible since it is completely overlapped by the output of the  $1Hz$  signal. . . . . 77
- 3.1 BSU implementing a memristor. In the figure "CM" stands for Current Mirror.  $V_s$  and  $V_{ref}$  are the input and reference voltage generators of the binary synapse unit. "Mem" identifies the memristor in the device. Refer to the following figures for the specific circuit element implementation. . . . . 88

3.2	(a) pMOS current mirror and (b) nMOS current mirror layout. $I_{ref}$ and $I_{mem}$ represent the reference current and the memristor current that flow through the resistive or memresistive elements, respectively, present in the two branches. Refer to Figure 3.1 for the complete layout implementation. . . . .	89
3.3	MCSU. The elements represented in the figure refer to the other descriptive circuit figures. The <i>SCU</i> is the sigma calculator unit depicted in Figure 3.4, while the <i>BSU</i> are the binary synapse units depicted in Figure 3.1. The resistances $R1$ to $RN$ have all the same value, so that the contribution of each synapse to the system depends only on the memristance value obtained through the algorithm. . . .	90
3.4	SCU. The output of this unit ( $\sigma$ ) is the input of the control unit (CU) and with respect to its value the SBPI perceptron will perform the algorithm according to the computed stability parameter $\Delta$ . $I_{Sum}$ is the current out-flowing from the MCSU (refer to Figure 3.3), acting as an input to this unit in order to perform the SBPI. . . . .	91
3.5	Workflow diagram of the Control Unit designed as a changing state machine. . . . .	92
3.6	Memristance variation vs. single input frequency. . . . .	94
3.7	Memristance change vs. logical state output of the binary synapse. In the first graph it is shown the difference between $R_{off}$ and $R_{mem}$ over $\Delta R$ In the second, the output of the system is described as a logical binary response. . . . .	95
3.8	Graphical description of the test and training procedure performed on the system. Two sets of inputs are given to both the student and the teacher. The student has the goal to return the same outputs of the teacher, learning its "implicit" rule. The colours of the arrows state the relation between the inputs and the given outputs. . . . .	97
3.9	Graph showing $\alpha$ vs. mean efficiency of each training-test trial. Increasing the size of the training input set it is possible to notice that the efficiency of the SBPI perceptron reaches 100%. . . . .	97

- 3.10 Graph showing  $\alpha$  vs. mean number of presentations needed for each training-test trial. For small  $\alpha$  values there is not enough information in the training set to infer the teacher's rule, and thus the number of presentations per patterns is saturated without reaching efficiency 1; beyond a critical value of  $\alpha$ , however, only a few presentations per pattern are sufficient to achieve perfect learning. . . . . 98
- 3.11 Frequency histogram for  $\theta = 0.06N$ ,  $\theta = 0.11N$ ,  $\theta = 0.16N$  and  $\theta = 0.21N$  with overlapped kernel curve (red line). . . . . 100
- 3.12 Frequency histogram for  $\theta = 0.26N$ ,  $\theta = 0.31N$  and  $\theta = 0.36N$  with overlapped kernel curve (red line). . . . . 101
- 4.1 Two examples of CA used for image processing. In both pictures the CA was used for detecting the edges of the subjects. This is one example of image processing operand that can be rendered through CAs. . . . . 107
- 4.2 In figure the theoretical circuit memristor implementation for a memristive CA taken from [41]. From their model it is possible to see that the inputs to the cell are given trough a signal generator. The inputs can be of two kinds: internal (the state of the surrounding cells) and external (the inputs that come from the external environment), in figure represented with pink and blue signal generators respectively. 109
- 4.3 Brief depiction of the crosswise CA. All three matrices ( $R$ ,  $G$ , and  $B$ ) are divided in cells which are compared through the equations in  $G(r_{i,j}, g_{i,j}, b_{i,j})$ . The results of the system give the inputs to the CA, which evolves horizontally and vertically from the original neighborhood array until it covers the whole image. . . . . 111
- 4.4 Generic subspace  $\Omega$  in the RGB space. Considering a generic RGB image, only several pixels are depicting a given subject in the figure. Those pixels have particular values that can be related through each other through the relations described by  $G(r_{i,j}, g_{i,j}, b_{i,j})$ . . . . . 113

- 4.5 Results of the CA iterations on a generic digital image. (a) Picture representing a subject holding two objects of similar colour which are intended to be identified and isolated from the picture. (b) The mask image given by matrix  $S$ , which is composed of the binary outputs of the three memristive matrices  $H_{r,g,b}$ . . . . . 114
- 4.6 The picture shows the *hardware* components of the device for the data collection regarding the ulcers. In the picture are indicated all the principal components. The case of the device was realized through a 3D printer. The temperature and humidity sensor is not shown since is inside the case. Next to the battery, in the handle, is located the Arduino NANO board. The FPGA is inside the case, which is attached to the smartphone through a custom cover. . . . . 118
- 4.7 Schematic example of the shade detection taken from an ulcer.  $\mathbf{Y}$  is the center of the CMOS camera,  $\mathbf{X}$  is the position of the given LED,  $\mathbf{O}$  is the point of incidence of the light with the skin border and  $\mathbf{F}$  is the end point of the shadow generated by the border with the given LED light. Still in the figure:  $h_1$  is the distance of the device from the skin,  $\lambda$  is the focal opening angle of the CMOS camera,  $\psi$  is the opening angle of the LED light (given by the data-sheet of the element),  $\gamma$  is the angle of incidence of the light with the skin border,  $p$  is the height of the skin border related to the wound,  $d$  is the length of the skin portion normal to the projection of the light, and finally  $l$  is the length of the shadow.  $C1$  and  $C2$  indicate the dimensions of the CMOS camera sensor. All the values are known thanks to the measurements of the device's sensors and from the design of the device itself, except for  $p$ ,  $\gamma$  and  $l$  that must be calculated through the here following procedure. In the figure is also reported the reference system with the directions 1, 2 and 3. . . . . 122
- 4.8 Results of the measurements performed on the area of the wound. The results are shown relating the accuracy of the measurement with its frequency. The results are overlapped with a curve which represents the kernel of the data. From the graph it is possible to state that more than 70% of the cases were measured with an accuracy greater than 85%. . . . . 127

- 4.9 (a) Sample picture of a wound and (b) mask of the wound built through the SBPI-CA. The system was able to recognize automatically the wound from the rest of the picture. Moreover the system was set to identify also portion of the peri-wound which have to be classified in the granulation assessment as pathological tissue. . . . 127

# List of Tables

2.1	Extended Memristor . . . . .	28
2.2	Generic Memristor . . . . .	28
2.3	Ideal Memristor . . . . .	29
2.4	SiNW Conditional Behaviour . . . . .	66
3.1	Results of the $\chi^2$ Analysis for Each Kernel . . . . .	102
4.1	SBPI–CA Particular colour detection rule . . . . .	113
4.2	WBP letter code taken from [135] . . . . .	116
4.3	WBP number code taken from [135] . . . . .	116
4.4	Patient test population characteristics . . . . .	124
4.5	Wound sample characteristics . . . . .	126
4.6	Pre-clinical trial system’s efficiency results . . . . .	128